

POLITECNICO DI TORINO

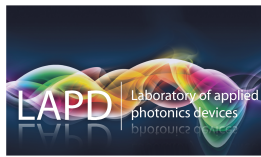
EPFL - LAPD

Degree in Electronic Micro and Nano Systems

Master Degree Thesis

Adaptive Optics Loop for Pupil Tracking

Eye aberration correction for new retinal microscopy



Supervisor

Prof. Renato Orta

Co-Supervisor:

Prof. Paolo Laporta

Candidate

Roberto RUSSO

matricola: 235343

Tutor

EPFL - Laboratory of Applied Photonic Devices

Prof. Christophe Moser
Dr Timothé Laforest Ph.D.

ACCADEMIC YEAR 2017 – 2018

*To my parents, the
strongest desirable
support*

Summary

Nowadays, the field of ophthalmology is permeated by a surging research to the purpose of retinal imaging with cellular resolution. The incredible rise in this research is fundamentally moved by the augmented capability to produce early diagnoses of invalidating diseases affecting the human eye. The realization of a commercial device that allows to perform the imaging of the different cells belonging to the several retina's layers is yet to come. The main reason of this lack is principally related to the complexity of the realization of such a system. One of the main element of complexity is due to the presence of eye aberrations, which introduce a phase distortion and thus implies a reduction of the achievable resolution. The eradication of this issue has old roots in a field far from ophthalmology. Indeed, a similar problem exists with the disturbances introduced by Newton's "Air's Tremors" in astronomy. The first solution proposed, which is still today one of the most applied, was in fact developed for this field. It consists in the reproduction of the *Optical Transfer Function* of the disturbances in order to eliminate their contribute. To perform this method generally included in the domain of *Adaptive Optics*, it is required to use a device that is able to perform the measurements of the disturbances, a wave-front sensor, and a device that is able to produce the correspondent countermeasures, a deformable mirror. The aim of this work will be handling the feedback loop created by the work of those two devices in order to perform the eyes' aberrations corrections, in the objective of replacing the current used proprietary software for a future perspective of integration of the *Adaptive Optics Loop* with all the others subsystems that handle the image acquisition. To fulfil this goal, proprietary functions provided by *Imagine OpticsTM* will be used, also to interface the two main components of the loop: the deformable mirror and the wave-front sensor, which are provided by the same producer. For the realization of this goal, several aspects have to be taken into account, from the specifications and limitations introduced by the particular devices used that have consequences on the actuation phase, to the issues related to the subject to analyse, the human eye. Indeed, the human eye is not a static object and, as a consequence, countermeasures related to its movements have to be taken to improve as much as possible the acquisition procedure. In this perspective, particular attention have to be focused on the blinking phenomena. After the development of the code, several tests and validation procedures were performed with the aim of clarify the results and the limitations of the provided solution also comparing it with the performances of the existent proprietary software to replace. The developed loop resulted to solve the main issues, from the blinking handling to the proprietary software "crash" condition related to the actuation voltages increase and to the exposure setting bottleneck removal. These also providing a comparable optical behaviour.

Acknowledgements

I would like to thank my tutor at EPFL, Professor Christophe Moser, for following me during this challenging experience; Timothé Laforest, Mathieu Kunzi and Dino Carpentras, for the pragmatic support and for the help concerning the in-vivo tests. In addition, the technical cooperation of *Imagine OpticsTM* client service had to be mentioned.

Furthermore, I am grateful to Professor Renato Orta for his continuous assistance and his advices during the development of the whole project, for his trust in me and for his own way to encourage deeper researches on the issues to be solved.

A further mention has to be done for Professor Paolo Laporta who accepted to externally support me although the difficulties he has encountered during the project development period.

Moreover, in the perspective of the conclusion of a challenging path started almost five years ago, a special mention have to be done for Professor Paolo Cortese. His teachings have been the root and the foundations of this path. He thought us to have the courage to be impatient, to withstand the test of fire, to have faith in ourselves.

A last mention to my parents, for their grate support and encouragement during these years, without them those results would not have been possible.

Contents

List of Tables	X
List of Figures	XI
1 Introduction	1
2 Theoretical background	5
2.1 Fourier Analysis in Two Dimensions	6
2.2 Anatomical Structure of the Eye	9
2.3 Optical Structure and Behaviour of the Eye	11
2.4 The Aberrations of the Eye and Their Limitations	13
2.5 The Aberrations Description	16
2.6 The Correction of the Aberrations	18
2.7 Adaptive Optics History and Evolution	19
2.8 The AO Loop Components: Shack-Hartmann Sensor	20
2.9 The AO Loop Components: the Deformable Mirror	22
2.10 Phase Reconstruction Techniques	24
3 Implementation of the AO Loop	27
3.1 The Retina Imaging System	28
3.1.1 Pupil Illumination Setup and Pupil Camera	29
3.1.2 Transscleral Illumination Source and Control	29
3.1.3 Adaptive Optics Loop	29
3.1.4 Imaging system	30
3.2 Description of the Library	30
3.3 Main Steps of the Loop	32
3.4 Initialization Phases	33
3.5 Dealing with the spots' matrix	36
3.5.1 Number of Spots Detected	39
3.5.2 Percentage of Sensor Surface Illuminated	41
3.5.3 Pixels Saturation	43
3.5.4 Shape of the Pupil	44
3.5.5 Consequences of the Methods	47
3.6 Evaluation of the Slopes	47
3.7 Phase Reconstruction	50

3.8	Moving the Actuators	51
3.9	Loop GUI	53
4	Testing and Validation of the AO Loop	55
4.1	The Tilt Problem and the Voltage	56
4.2	In-vivo Imaging Results	67
4.3	Withstanding the Blinking	71
4.4	Testing the Optical Resolution	77
4.5	Analysis of the Speed	78
5	Conclusions and Future Works	83
	Bibliography	85
A	Spots' Matrix During Blinking	I
B	Flow Diagram of the Loop	V
C	In-vivo retina images	VII

List of Tables

4.1 Results of Blinking verification	75
4.2 Speed contributions analysis	81

List of Figures

2.1	Schematic structure of the generalized optical system [2]	8
2.2	Close up of human eye on the left [3] Anatomy of the Human eye on the right [4]	10
2.3	Schematic structure of the main layers of the human Retina [6]	11
2.4	Schematic and simplified abrupt step variation of the refractive index n for the eye's structure [6]	11
2.5	Schematic of the accommodation process [9] to the left decreasing of Accommodation range with age [6] to the right	13
2.6	Comparison between ideal and non-ideal psf and resulting images	14
2.7	Fraunhofer diffraction pattern from circular aperture [14]	15
2.8	Spot diameter on the retina as a function of pupil size [6]	15
2.9	Representation of the aberrations [2]	16
2.10	Bright Star (Arcturus) Observed with Lick Observatory's 1-m Telescope California [18]	20
2.11	Shack Hartmann sensor principle and behaviour [23]	21
2.12	Principle of the Deformable Mirror operation [24]	22
2.13	Example of a deformable mirror with rectangular elements [25] to the left, possible astronomical setup with hexagonal sub-elements deformable mirror [25] to the right	23
2.14	Types of continuous surface deformable mirrors [25] to the left, possible kind of actuators [25] to the right	24
2.15	Structure of the <i>Mirao 52e, Imagine Eyes</i> deformable mirror [27]	24
2.16	Slope measurements sampling geometry and wave-front mesh points [28]	25
3.1	complete scheme of the system [1]	28
3.2	Schematic of the functions	31
3.3	Skeletal hardware schematic of the loop	32
3.4	Main steps of the loop	33
3.5	Schematic of the "auto-exposure" loop	36
3.6	Example of resulting spots' matrix in the case of ex-vivo fake eye on the left (exposure time = 2.35 ms, SLD power continuous mode = $28 \mu\text{W}$) and in the case of in-vivo real eye on the right (exposure time = 10 ms, SLD power continuous mode = $20 \mu\text{W}$)	37

3.7	Comparison between the spots' matrix obtained in the normal case (left), when approaching the blinking (centre) and when the eye is closed (right) (exposure time = 10 ms, SLD power continuous mode = $20 \mu\text{W}$). For the full series of images of the evolution of the spots' matrix during the blinking see Appendix A	38
3.8	Result of the Number of spots threshold on a "good" in-vivo matrix; Number of Spots detected = 1158 (exposure time = 10 ms, SLD power continuous mode = $20 \mu\text{W}$)	40
3.9	Result of the Number of spots threshold on a "bad" in-vivo matrix; Number of Spots detected = 738 (exposure time = 10 ms, SLD power continuous mode = $20 \mu\text{W}$)	40
3.10	Result of the Surface threshold on a "good" in-vivo matrix; Surface percentage detected = 0.1471% (exposure time = 10 ms, SLD power continuous mode = $20 \mu\text{W}$)	42
3.11	Result of the Surface threshold on a "bad" in-vivo matrix; Surface percentage detected = 1.8068% (exposure time = 10 ms, SLD power continuous mode = $20 \mu\text{W}$)	42
3.12	Variation of the pixels intensity during a blinking phase, spots' matrix from Appendix A (exposure time = 10 ms, SLD power continuous mode = $20 \mu\text{W}$)	43
3.13	Shape analysis for a "good" spots' matrix; shape parameter obtained = 0.0452 (exposure time = 10 ms, SLD power continuous mode = $20 \mu\text{W}$) . .	46
3.14	Shape analysis for a "bad" spots' matrix; shape parameter obtained = 0.4 (exposure time = 10 ms, SLD power continuous mode = $20 \mu\text{W}$)	46
3.15	Principle aberrations according to Zernike basis [36]	49
3.16	Principle of the spots shifting	50
3.17	Principle of the "security check" on the maximum voltage applied to the mirror	52
3.18	example of tilt difference: plane $70x + 21z = 0$ on the left and plane $35x + 21z = 0$ on the right	53
3.19	example of tilt difference: plane $35x + 21z + 30 = 0$ on the left and plane $35x + 21z = 0$ on the right	53
3.20	appearance of the interface to the user	54
4.1	Evolution of the Total voltage applying <i>tilt_filtering</i> parameter, ex-vivo case (Exposure Time = 1.04 ms, 32 modes, gain = 0.5, Power SLD = $28 \mu\text{W}$)	56
4.2	Evolution of the Total voltage applying <i>tilt_filtering</i> parameter, in-vivo case (Exposure Time = 5.32 ms, 32 modes, gain = 0.5, Power SLD = $28 \mu\text{W}$)	57
4.3	Evolution of the linear component on the applied commands using <i>tilt_filtering</i> parameter, ex-vivo case; images taken from the top for iteration number 10, 500, 1900 (Exposure Time = 1.04 ms, 32 modes, gain = 0.5, Power SLD = $28 \mu\text{W}$)	58
4.4	Evolution of the linear component on the applied commands using <i>tilt_filtering</i> parameter, ex-vivo case; images taken from the top for iteration number 10, 200, 440 (Exposure Time = 5.32 ms, 32 modes, gain = 0.5, Power SLD = $28 \mu\text{W}$)	59

4.5	Evolution of the Total voltage applying <i>tilt_filtering</i> parameter and <i>tilt_check</i> parameter, ex-vivo case (Exposure Time = 1.09 ms, 32 modes, gain = 0.5, Power SLD = 28 μ W)	60
4.6	Evolution of the Total voltage applying <i>tilt_filtering</i> parameter and <i>tilt_check</i> parameter, in-vivo case (Exposure Time = 5.12 ms, 32 modes, gain = 0.5, Power SLD = 28 μ W)	60
4.7	Evolution of the linear component on the applied commands using <i>tilt_filtering</i> parameter and <i>tilt_check</i> parameter, ex-vivo case; images taken from the top for iteration number 100, 1000, 1900 (Exposure Time = 1.09 ms, 32 modes, gain = 0.5, Power SLD = 28 μ W)	61
4.8	Evolution of the linear component on the applied commands using <i>tilt_filtering</i> parameter and <i>tilt_check</i> parameter, in-vivo case; images taken from the top for iteration number 100, 1000, 1900 (Exposure Time = 5.12 ms, 32 modes, gain = 0.5, Power SLD = 28 μ W)	62
4.9	Evolution of the Total voltage applying <i>tilt_filtering</i> parameter and <i>tilt_check</i> parameter, evolution of the RMS residual phase error and evolution of the shape parameter, in-vivo case (Exposure Time = 6.44 ms, 32 modes, gain = 0.5, Power SLD = 28 μ W)	63
4.10	Evolution of the Total voltage applying forcefully removal of tilt component, ex-vivo case (Exposure Time = 1.39 ms, 32 modes, gain = 0.5, Power SLD = 28 μ W)	64
4.11	Evolution of the Total voltage applying forcefully removal of tilt component, ex-vivo case (Exposure Time = 6.04 ms, 32 modes, gain = 0.5, Power SLD = 28 μ W)	64
4.12	Evolution of the linear component on the applied commands applying forcefully removal of tilt component, ex-vivo case; images taken from the top for iteration number 100, 1000, 1900 (Exposure Time = 1.39 ms, 32 modes, gain = 0.5, Power SLD = 28 μ W)	65
4.13	Evolution of the linear component on the applied commands applying forcefully removal of tilt component, in-vivo case; images taken from the top for iteration number 100, 1000, 1900 (Exposure Time = 6.04 ms, 32 modes, gain = 0.5, Power SLD = 28 μ W)	66
4.14	Acquired image of the retina: on the left column the one relative to the forcefully removal of tilt configuration, on the right one the image produced using the <i>tilt_check</i> configuration. See also Figures C.1 and C.2 of Appendix C	68
4.15	Fourier domain zoom: on the left column the one relative to the forcefully removal of tilt configuration, on the right one the image produced using the <i>tilt_check</i> configuration.	68
4.16	Comparison in terms of axial behaviour of integrated intensity in Fourier domain.	69
4.17	Acquired image of the retina: on the left column using the proprietary software, on the right one the image produced using the using the developed loop. See also Figure C.3 of Appendix C	69
4.18	Fourier domain zoom: on the left column using the proprietary software, on the right one the image produced using the using the developed loop.	70

4.19	Comparison in terms of axial behaviour of integrated intensity in Fourier domain.	70
4.20	In-vivo test of the ability of the loop to withstand the blinking: residual phase RMS error (Exposure Time = 6.04 ms, 32 modes, gain = 0.5, Power SLD = 28 μ W)	72
4.21	In-vivo test of the ability of the loop to withstand the blinking: variation of the different figures of merit during the loop, in red the variations, in blue the thresholds set. From the top to the bottom: Saturation, Shape Parameter, Surface Parameter, Spots Detected (Exposure Time = 6.04 ms, 32 modes, gain = 0.5, Power SLD = 28 μ W)	73
4.22	In-vivo test of the ability of the loop to withstand the blinking, variations of the different figures of merit during the loop, in red the variations, in blue the thresholds set. From the top to the bottom: Saturation, Shape Parameter, Surface Parameter, Spots Detected (Exposure Time = 11.74 ms, 32 modes, gain = 0.5, Power SLD = 28 μ W)	74
4.23	Pupil camera's frames for the first blinking episode of table 4.1	75
4.24	In-vivo test of the ability of the loop to withstand the blinking without any check on the values of the figures of merit, total amount of applied voltage and residual phase RMS error (Exposure Time = 9.62 ms, 32 modes, gain = 0.5, Power SLD = 28 μ W)	76
4.25	In-vivo test of the ability of the loop to withstand the blinking without any check on the values of the figures of merit, spots' matrix appearance at the instant of failure (Exposure Time = 9.62 ms, 32 modes, gain = 0.5, Power SLD = 28 μ W)	76
4.26	Acquired image of the USAF Target, on the left column the ones relative to the proprietary software (zoom below), on the right one the image produced using the implemented software (zoom below)	77
4.27	Evaluated behaviour of the MTF for the images in Figure 4.26, on the left the one relative to the proprietary software, on the right the one produced using the implemented software	78
4.28	Superimposition of the MTF shown separately in Figure 4.27	78
4.29	In-vivo test speed results, evolution of the frequency during the loop running, decrease of frequency are correspondent to blinks of the patient (Exposure Time = 11.74 ms, 32 modes, gain = 0.5, Power SLD = 28 μ W)	79
4.30	In-vivo test pie redistribution of the time required for the different tasks (Exposure Time = 11.74 ms, 32 modes, gain = 0.5, Power SLD = 28 μ W)	80
4.31	In-vivo test pie redistribution of the time required for the different tasks (Exposure Time = 11.74 ms, 32 modes, gain = 0.5, Power SLD = 28 μ W)	80
4.32	In-vivo test evolution during the loop the time required for the different tasks (Exposure Time = 11.74 ms, 32 modes, gain = 0.5, Power SLD = 28 μ W)	81
A.1	from the beginning of the Appendix A it is possible to see the spots' matrix changing during a blink of the patient eye	IV
B.1	More precise schematic of the evolution of the loop	V
C.1	Acquired image of the retina obtained with the forcefully removal of tilt configuration	VII

C.2	Acquired image of the retina obtained with the <i>tilt_check</i> configuration . .	VIII
C.3	Acquired image of the retina using the proprietary software.	IX

Chapter 1

Introduction

One of the most complex challenge to face in ophthalmology is the early detection of the diseases that could affect the eyes, above all in the direction of preventing future issues for the patient. This demanding need results to be even more complex when it comes to follow in real time the deteriorating of retina imaging properties. Indeed, the complexity is directly originated from the high complicatedness of the retina biological structure, organised in several layers of different type of cells, all concurrent to establish the eyesight abilities of the patient. Moreover, dealing with the degeneration of the retina potentialities and performances is a crucial situation due to the highly probable following outcomes: final irretrievable visual losses. To overcome those issues the fundamental step is to have the possibility to detect and appropriately imaging in-vivo retina cells, to have a better insight of the current conditions of the patient. Furthermore, the realization of this objective have to bear in mind the need for the in-vivo apparatus to be able to retrieve all the information required in a way as less invasive as possible. Mainly this last is, at a first glance, the reason why it is not yet possible to perform the correct imaging of each of the retina cells type layers with a commercial device. This lack generates the need for research and is the springing root of the chosen structure realization, which is also sustained by the work of this thesis. The approach used in this case for the accomplishment of the original goal is based on “multiple oblique directions transscleral illumination” whose advantages and consequences are deeply illustrated by Laforest et al. [1]. To fulfil the objective of a “good cellular resolution” , also for in vivo measurements, it is fundamental, before reconstructing the images processing the back-scattered light from retina layers, to have an accurate correction of the aberrations of the eye. To perform this important step several techniques are commonly used, among them it is worth to take into account the more diffused, nonetheless, for the realization of the currently used experimental setup, it has been chosen the *adaptive optics* method. Indeed, the final goal of this work, is to replace the existent software that controls the Adaptive Optics Loop (AOL) with something easier to handle and to access with respect to the original “black box” proprietary one, above all in the optics of a future integration with all the other subsystem constituting the device, but also to investigate crucial “crash” situations as the one related to the saturation of the physical limits of the device used for the actuation, or to overcome some bottleneck during the initialization phase as the one related to the setting of the exposure time. This feedback control system is of basilar importance to obtain a correct retinal imaging,

providing the highest achievable resolution, so as to have the possibility to detect each and everyone of the cells of medical interest. To fulfil this goal, proprietary functions provided by *Imagine OpticsTM* will be used, also to interface the two main components of the loop: the Deformable Mirror (DM) and the wave-front Sensor (WS), which are provided by the same producer.

Before to describe progressively the building of the software, provided the aforementioned base, a theoretical background analysis on different fields have to be performed. As a part of this theoretical fragment the Chapter 2 will propose a generalized inspection of the concept, which constitute the foundation for the development. First of all it will present in Section 2.1 an insight on the principles of *Fourier Optics Analysis* in 2-dimensional problems, zooming on the definition of several relevant quantities as the *Amplitude Transfer Function* (ATF), the *Optical Transfer Function* (OTF) and the *Modulation Transfer Function* (MTF). With those concepts as background it will be smoother to deal with the following tasks. Hereafter, Section 2.2 will describe some of the anatomical features of the eyes that could be useful for further understandings. Moreover, it will be followed by Section 2.3 that outlines the optical characteristics of the eyes. The description of the limitations introduced by eyes's *Aberrations* performed in Section 2.4 will be a starting point to expose a brief description of the *Aberrations* in Section 2.5, whose correction will be later discussed in Section 2.6. Thereafter, a brief history of the concept of Adaptive Optics will be exposed in Section 2.7, focusing then on the behaviour of the two main components of this kind of feedback systems in Section 2.8 and Section 2.9. Moreover, several *Phase Reconstruction* techniques will be mentioned in Section 2.10 of Chapter 2. Afterwards, having provided all the theoretical elements that could be relevant or influencing the development, the realization of the whole software for the handling of the *Adaptive Optics Loop* will be discussed in Chapter 3. This chapter will starts giving in Section 3.1 a first glance on the structure of the whole complex system used for retinal imaging, underlying all the involved and intricate subsystems that play a role in the arrangement of the final resulting device. This step is intrinsically crucial to comprehend the utility of the current work in the behaviour of the overall system. Later, a brief description of the functionality offered by the *Imagine OpticsTM* Library in Section 3.2 will be performed. Hereafter the main steps to be addressed will be described in Section 3.3. The successive Sections will then discuss the implementation of each of the main important stages and process. This deeper analysis will start describing the *Initialization Phase* in Section 3.4. It will then prosecute passing to the more essential handling of the *spots' matrix* in Section 3.5. The relevance of this phase comes from the possible errors of the system that could be avoided correctly considering the "goodness" of the *spots' matrix*. Further, the slopes evaluation process and the phase reconstruction stage will be discussed in Section 3.6 and in Section 3.7 respectively. To conclude the software description the actuation step will be then handled in Section 3.8. Finally, a brief presentation of the *GUI* version of the developed loop will be performed. Chapter 4, will then deal with the discussion of the main aspects tested and with the description of the overall behaviour of the developed software. Particularly, the effects of *Tilt Removal* will be treated in Section 4.1, this effect is related to the physical limitations of the devices used. Afterwards, the validation of what discussed in Section 4.1 will be provided in Section 4.2. Moreover, the testing related to the effectively capability of the software to withstand the blinking will be provided in Section 4.3. A characterization

of the system will be then provided in Section 4.4 thanks to the measurements performed with a standard USAF Target. The Chapter will be then concluded by a description of the system's speed analysis in Section 4.5. Eventually, the main contributions and the future perspectives will be then described in Chapter 5.

Chapter 2

Theoretical background

The aim of this chapter is mainly to present the theoretical background that lays behind the conceptual and practical development of an Adaptive Optics system. Those knowledges are basically significant not only for the general understanding of a set of parameters that could be encountered during the process but also to appreciate the rooting reason for the usage of this procedure in the realization of a complex imaging system.

Indeed, the chapter will begin with a broad description of the methods and tools used to describe a complex optical system. The focus will be initially put on the concepts of *Point Spread Function* (PSF), *Optical Transfer Function* (OTF) and *Modulation Transfer Function* (MTF) in Section 2.1. Those concepts could be generically considered as the optical correspondence of the broad concept, largely used in the *electronic's domain* and in *Control Theory*, of *Pulse response* and *Transfer Function*. The reason why those concepts, together with the optical description of a “*black-box system*”, are important is prevalently related to the correction of *Eyes' aberrations*. The following needed step will be the description of the human eye, before from an anatomical perspective in Section 2.2 and then from the optical point of view, which will be tackled within Section 2.3. Section 2.4 will then aim attention at the limitations introduced by *Eyes' Aberrations*, drawbacks that consequently constitute the ground that forces their correction. Furthermore, a more specific description of the aforementioned *Aberrations* will be afterwards addressed as in Section 2.5. Later, in Section 2.6 the study will be moved on the description of the procedure to correct those aberrations. Moreover, the chosen correction technique will be largely presented in Section 2.7, underlying the origin of the concept, which was originally far from the field of ophthalmology. Afterwards, the main devices that allows the realization of such a system will be presented in Section 2.8 and Section 2.9. Finally an analysis of the Phase reconstruction techniques will be discussed in Section 2.10.

2.1 Fourier Analysis in Two Dimensions

To perform with ease the analysis of optical system a few mathematical tools are required. The usefulness of Fourier analysis for the description of time variant problems in the frequency domain is doubtless, its versatility and efficacy allows it to be used for several problems that spread from control theory to electronic signal processing. The full description of an optical system requires an extension of those frequently used tools. Indeed, very often, there will be the need to use them on functions of two independent variables. As a consequence, it is worth to introduce the Fourier transform couple for a 2-dimensional problems. For a generic function $g(x, y)$ the *Direct Fourier Transform* is defined accordingly to equation 2.1 while the *Inverse Fourier Transform* is defined by equation 2.2 [2].

$$G(f_x, f_y) = \mathcal{F}g(x, y) = \iint_{-\infty}^{\infty} g(x, y) \cdot e^{-j \cdot 2\pi \cdot (f_x \cdot x + f_y \cdot y)} dx dy \quad (2.1)$$

$$g(x, y) = \mathcal{F}^{-1}G(f_x, f_y) = \iint_{-\infty}^{\infty} G(f_x, f_y) \cdot e^{j \cdot 2\pi \cdot (f_x \cdot x + f_y \cdot y)} df_x df_y \quad (2.2)$$

As for the mono-dimensional case several properties are still valid [2].

Linearity

$$\mathcal{F}\{\alpha g + \beta h\} = \alpha \mathcal{F}g + \beta \mathcal{F}h \quad (2.3)$$

Similarity

$$\mathcal{F}\{g(ax, by)\} = 1/|ab| \cdot G(f_x/a, f_y/b) \quad (2.4)$$

Shift

$$\mathcal{F}\{g(x - a, y - b)\} = G(f_x, f_y) \cdot e^{-j \cdot 2\pi \cdot (f_x \cdot a + f_y \cdot b)} \quad (2.5)$$

Convolution

$$\mathcal{F}\left\{\iint_{-\infty}^{\infty} g(\xi, \eta)h(x - \xi, y - \eta)d\xi d\eta\right\} = G(f_x, f_y)H(f_x, f_y) \quad (2.6)$$

Autocorrelation

$$\mathcal{F}\left\{\iint_{-\infty}^{\infty} g(\xi, \eta)g^*(x - \xi, y - \eta)d\xi d\eta\right\} = |G(f_x, f_y)|^2 \quad (2.7)$$

$$\mathcal{F}\{|g(x, y)|^2\} = \iint_{-\infty}^{\infty} G(\xi, \eta)G^*(x - \xi, y - \eta)d\xi d\eta \quad (2.8)$$

Having defined the tools, it is possible to describe a representation of an optical system. If an *Operator Approach* is used, several figure of merit could be obtained. Supposing an input function $g_1(x, y)$ and an output function $g_2(x, y)$, this representation leads to equation 2.9 [2].

$$g_2(x, y) = \mathcal{S}\{g_1(x, y)\} \quad (2.9)$$

where \mathcal{S} represent the action of the system on the input function.

Supposing then that the system that had to be described has *Linearity* properties, such that it is true equation 2.10, it is possible to proceed into a “decomposition step”. Starting from the shift property (Equation 2.5) applied to a delta, referred by equation 2.11, and replacing it into equation 2.9, it is possible to finally achieve, passing from equation 2.12 the definition of an important figure of merit for the system: the *Pulse Response* or in optics *Point Spread Function* (PSF) 2.13 [2].

$$\mathcal{S}\{a \cdot p(x, y) + b \cdot q(x, y)\} = a \cdot \mathcal{S}\{p(x, y)\} + b \cdot \mathcal{S}\{q(x, y)\} \quad (2.10)$$

$$g_1(x_1, y_1) = \iint_{-\infty}^{\infty} g_1(\xi, \eta) \delta(x_1 - \xi, y_1 - \eta) d\xi d\eta \quad (2.11)$$

$$\begin{aligned} g_2(x_2, y_2) &= \mathcal{S}\{g_1(x_1, y_1)\} = \mathcal{S}\left\{\iint_{-\infty}^{\infty} g_1(\xi, \eta) \delta(x_1 - \xi, y_1 - \eta) d\xi d\eta\right\} \\ &= \iint_{-\infty}^{\infty} g_1(\xi, \eta) \mathcal{S}\{\delta(x_1 - \xi, y_1 - \eta)\} d\xi d\eta \end{aligned} \quad (2.12)$$

$$PSF = h(x_2 - \xi, y_2 - \eta) = h(x_2, y_2; \xi, \eta) = \mathcal{S}\{\delta(x_1 - \xi, y_1 - \eta)\} \quad (2.13)$$

Then, is easy to notice that the definition of the output function is equal to the input one convoluted with the *Pulse Response*. Hence, as a consequence of convolution property (Equation 2.6), it is obtain the relationship into the “frequency domain” as in equation 2.14.

$$G_2(f_x, f_y) = H(f_x, f_y) \cdot G_1(f_x, f_y) \quad (2.14)$$

where $G_1(f_x, f_y)$ and $G_2(f_x, f_y)$ are the Fourier transform of $g_1(x, y)$ and $g_2(x, y)$ respectively, while $H(f_x, f_y)$ is the Fourier transform of the PSF as in equation 2.15.

$$H(f_x, f_y) = \iint_{-\infty}^{\infty} h(x, y) e^{-j \cdot 2\pi(f_x x + f_y y)} dx dy \quad (2.15)$$

Given the the extension of Fourier transform and of its properties for the 2-dimensional case, and provided the generalized description of the pulse response function, the PSF and of the correspondent Fourier transform, the transfer function, it is worth to apply those tools to have a clearer insight into the prerogatives of an optical system. To do so it is important to familiarize with an optical setup’s properties starting from a possible model of it. A generic optical imaging system can be represented as a *Black Box* structure with an input and an output, the *Entrance Pupil* and the *Exit Pupil* respectively (Figure 2.1). According to Goodman, such a system is defined *Diffraction Limited* if “a diverging spherical wave incident on the Entrance Pupil, is converted by the system into a converging

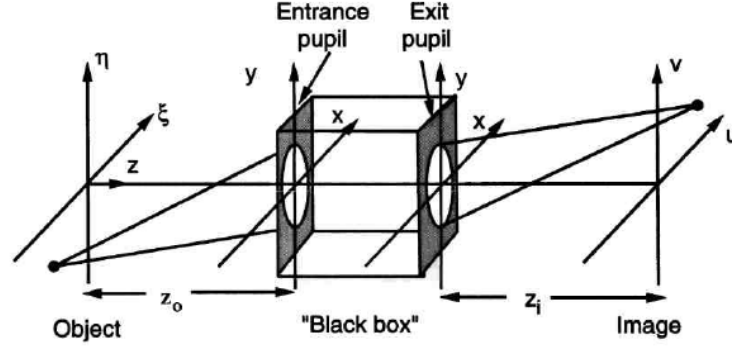


Figure 2.1. Schematic structure of the generalized optical system [2]

spherical wave at the Exit Pupil ... If in the presence of a point source object, the wavefront leaving the Exit Pupil departs significantly from ideal spherical on shape, then the imaging system is said to have *Aberrations* ” [2].

The optical systems could be classified according to different kind of properties, one of the possible classification is performed starting from the kind of light used as illumination. In this case it is possible to distinguish *Coherent Illumination Systems* and *Incoherent Illumination Systems*. The formers are *Linear* in *Complex Amplitude* of the field, the latter are *Linear* in *Intensity*.

In the case of *Coherent Illumination Systems* the frequency analysis allows to determine the *Amplitude Transfer Function* (ATF) as the Fourier transform of the amplitude PSF. As a consequence equations 2.16, 2.17, 2.18 and 2.19 are valid for the system[2].

$$G_i(f_x, f_y) = \iint_{-\infty}^{\infty} U_i(u, v) e^{-j \cdot 2\pi(f_x u + f_y v)} du dv \quad (2.16)$$

$$G_o(f_x, f_y) = \iint_{-\infty}^{\infty} U_o(u, v) e^{-j \cdot 2\pi(f_x u + f_y v)} du dv \quad (2.17)$$

$$H(f_x, f_y) = \iint_{-\infty}^{\infty} h(u, v) e^{-j \cdot 2\pi(f_x u + f_y v)} du dv \quad (2.18)$$

$$G_o(f_x, f_y) = H(f_x, f_y) \cdot G_i(f_x, f_y) \quad (2.19)$$

On the other hand, in the case of *Incoherent Illumination Systems* the frequency analysis allows to determine the *Optical Transfer Function* (OTF) as the Fourier transform of the intensity PSF. Moreover it is worth to mention the *Modulation Transfer Function* (MTF) defined as the magnitude of the OTF. As a consequence of the *intensity convolution integral* (Equation 2.20) equations 2.21, 2.22, 2.23, 2.24 and 2.25 are valid for the system [2].

$$I_o(u, v) = k \iint_{-\infty}^{\infty} |h(u - \xi, v - \eta)|^2 I_i(\xi, \eta) d\xi d\eta \quad (2.20)$$

$$\mathcal{G}_i(f_x, f_y) = \frac{\iint_{-\infty}^{\infty} I_i(u, v) e^{-j \cdot 2\pi(f_x u + f_y v)} dudv}{\iint_{-\infty}^{\infty} I_i(u, v) dudv} \quad (2.21)$$

$$\mathcal{G}_o(f_x, f_y) = \frac{\iint_{-\infty}^{\infty} I_o(u, v) e^{-j \cdot 2\pi(f_x u + f_y v)} dudv}{\iint_{-\infty}^{\infty} I_o(u, v) dudv} \quad (2.22)$$

$$OTF = \mathcal{H}(f_x, f_y) = \frac{\iint_{-\infty}^{\infty} |h_i(u, v)|^2 e^{-j \cdot 2\pi(f_x u + f_y v)} dudv}{\iint_{-\infty}^{\infty} |h_i(u, v)|^2 dudv} \quad (2.23)$$

$$\mathcal{G}_o(f_x, f_y) = \mathcal{H}(f_x, f_y) \cdot \mathcal{G}_i(f_x, f_y) \quad (2.24)$$

$$MTF = |OTF| = |\mathcal{H}(f_x, f_y)| \quad (2.25)$$

2.2 Anatomical Structure of the Eye

The human eye can surely be considered as a complex optical system. This system, which is anatomically composed by several tissues, each of them specialized in one of the fundamental steps that allows human sight, has been optically modelled by numerous Scientist and Researchers. Each of those models has few differences with respect to the others since they tackle with different levels of accuracy, or focusing on different aspects, the hugely complex structure of the eye. Before presenting the optical properties of such a complex sensor, it is worth to perform a depthless description of its anatomical structure, in order to be able to further collocate its optical properties.

The human eye has approximately the shape of a sphere, with a central sub spherical protuberance on the sight side. Starting from this last structure and following the light entering the eye, it is possible to encounter several important and different structures. The first element that the light faces is the *Cornea*, which physically separate the eye from the external environment; prosecuting in its propagation the light will pass through the *Anterior Chamber* and arrives to the *Crystalline lens*. This last element, which could be really correlated to the behaviour and properties of an optical lens, is exposed to a variable amount of light. That amount depends on the aperture of the *Pupil*, which is the central hole created by the *Iris* movements. The *Iris* is a membrane that behaves as a diaphragm enabling the possibility to regulate the amount of light entering the eye. After having crossed the *Crystalline Lens*, with all the layers that constitute it, the light will pass through a more extended region, known as *Vitreous Humor*, and will finally arrive on the *Retina* (Figure 2.2).

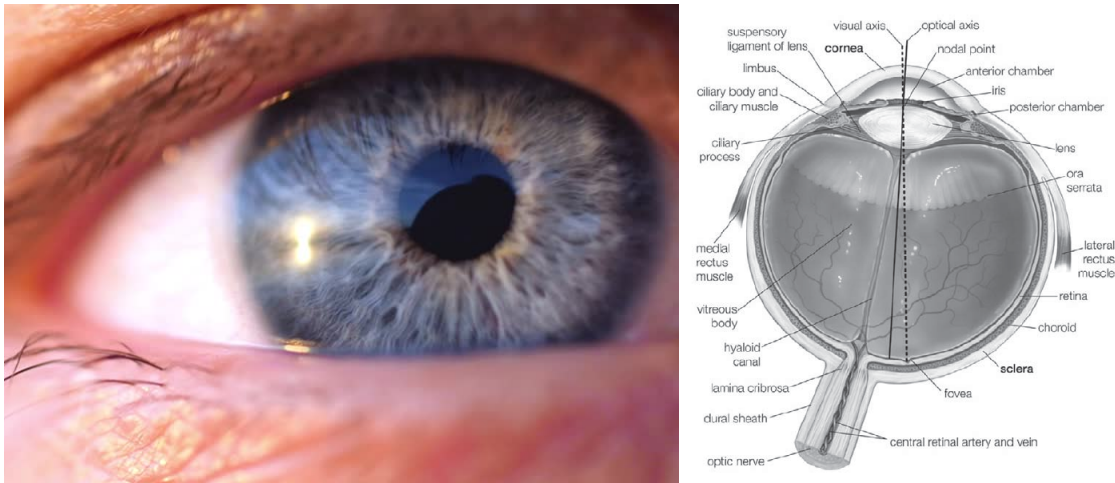


Figure 2.2. Close up of human eye on the left [3] Anatomy of the Human eye on the right [4]

The *Retina* itself has a quite complex structure that is composed by the aggregation of several layers of cells (Figure 2.3). The aim of those layers is mainly to recollect the information generated on the most inner region, the one of the receptors, and to convey it into the *optical nerve* that brings that information to the human brain. The farthest layer from the *Vitreous Humor* is characterised by the presence of *Cones* and *Rods*. The formers are the receptors related to the *Photopic Vision* (Daylight environment), the latter of the *Scotopic Vision* (Night environment). The light reaches the receptors' layer thanks to the transparency of the previous encountered cells. The two kind of receptors are characterized by different *Spectral Sensitivity*; indeed, the two curves that represents the ability of those receptors to be chromatically stimulated peak at different wavelengths: around 550 nm for the photopic cones and around 500 nm for the scotopic rods. In average, a normal human eye posses 125 million of receptors in this layer. The intermediate layer of the retina is characterised mainly by the *Interneuronal Bipolar Cells* that are connected to the *Rods* and *Cones* thanks to the *Horizontal Cells* while to the more external layer through the *Amacrine Cells*. The last layer, the closest to the *Vitreous Humor*, is constituted by *Ganglion Cells*. The information generated at the layer of the 125 millions of receptors is then conveyed to the optical nerve through the 1 million *Ganglion Cells* whose axons are then going to form the optical nerve [5].

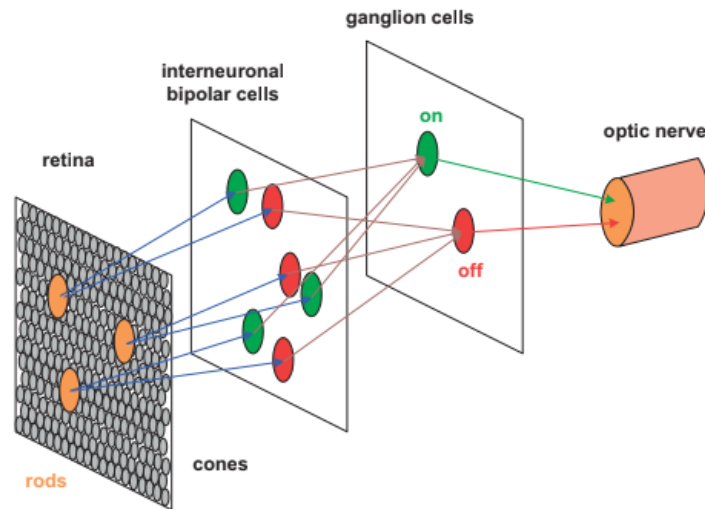


Figure 2.3. Schematic structure of the main layers of the human Retina [6]

2.3 Optical Structure and Behaviour of the Eye

If the eye is analysed from an optical point of view several elements could be pointed out. Primarily it is possible to describe the system as characterized by a variation of the refractive index. Indeed, as shown in figure 2.4, the refractive index slightly change between the several structure previously presented.

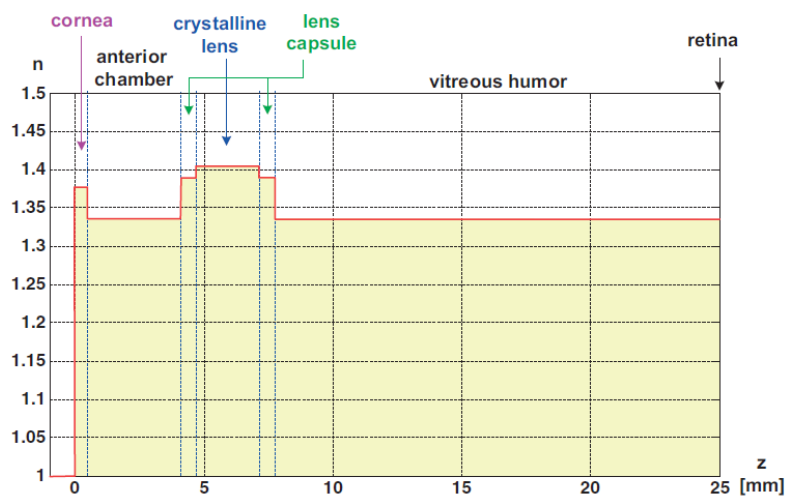


Figure 2.4. Schematic and simplified abrupt step variation of the refractive index n for the eye's structure [6]

Those variations allows the eyes to make light converges on the *retina*, and more specifically principally on its most sensible region the *fovea*. To understand this phenomena first of all it is important to notice that, as demonstrated by *Snell law* (Equation 2.26) when the light encounters a refractive index mismatch it is bent of an angle θ_{out} accordingly to the incidence angle θ_{in} and to the values of the refractive indexes at the interface .

$$\theta_{in} \cdot n_{in} = \theta_{out} \cdot n_{out} \quad (2.26)$$

As a consequence of this simple property of the light it is clearly important to underline the two significant refractive index mismatches that light faces passing through the eye. To go further, two more concepts are required, the definition of *Focal Length* and the definition of *Refractive Power*. The former is defined, supposing a lens in air environment and neglecting the constant phase factor introduced by the thickness of the lens, accordingly to equation [2], and corresponds to the distance from the lens at which the *Focus Point* will occur. This last is defined as the point at which the light will be forced to converge for a converging lens and from which the light seems to be originated in case of a diverging lens.

$$f = (n_{lens} - 1) \cdot \left(\frac{1}{R_1} - \frac{1}{R_2} \right) \quad (2.27)$$

where n_{lens} represents the refractive index of the considered lens, R_1 and R_2 the *Radius of Curvature* of the input and output face of the lens respectively. The second important concept is then the *Refractive Power*, which is simply defined as the inverse of the *Focal Length*. In the case of the eye this interesting quantity is measured in diopters ($dpt = [1/m]$). Having defined those two quantities is now possible to say that the *Refractive Power* of the eye, so its ability to makes light converge from a certain *Focal Length* onto the *retina* is, as shown by Gross, located for $2/3$ at the *Cornea* with a difference of refractive index of 0.377 and for the remaining $1/3$ at the *Crystalline Lens* with a difference of 0.08 [6].

Moreover, it is worth to mention that the eye is able to adapt for change of distances of the objects, this is due to the fact that the *Crystalline Lens* is a variable refractive element whose configuration could change in time thanks to the anatomical and biological structure of the eye itself, this mechanism is referred as *Accommodation*. The description of this complex mechanism was firstly proposed by Hermann Von Helmholtz; he suggested that this process, which corresponds to a variation of the *Refractive Power* previously mentioned, is enabled by a change of stress generated on the elastic *Crystalline Lens* by muscular structures referred as *ciliary muscles* connected to the lens by the *Zonules filaments* 2.5. The relaxation of that muscular structure, corresponding to its expansion, provoke the flattening of the eye lens and the reduction of its *Refractive Power*; this condition corresponds to the *Unaccommodated state*, or in other words to the focusing at infinite (around 6 m for humans). On the other hand the contraction of that structure implies a relaxation of the lens, which, becoming more curved, increases its *Refractive Power*, enabling, in the end, the focus for closer objects [7]. From an engineering perspective the process is handled with a feedback relationship which involves the *Cones* and the mechanical components, the *ciliary muscles*. This biological process allows to obtain a variation of *Refractive Power* from almost 22 dpt to slightly more than 35 dpt [8]. This range varies with the age.

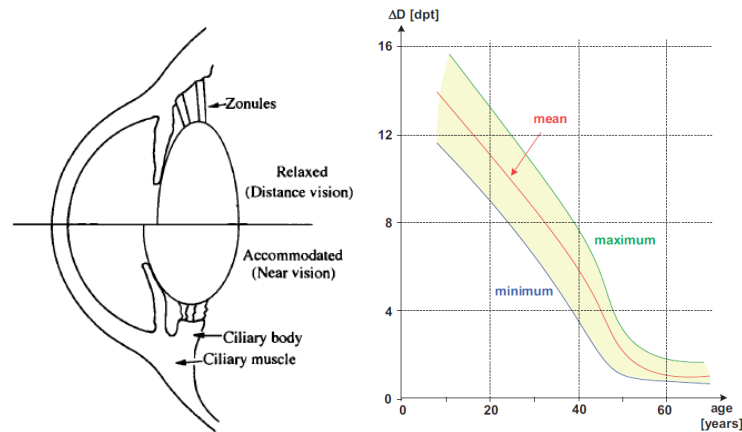


Figure 2.5. Schematic of the accommodation process [9] to the left decreasing of Accommodation range with age [6] to the right

Furthermore, it is important to bear in mind that the values taken to describe the variation of refractive index of the several layers and structures of the eye come from the *Full Gullstrand* eye schematic model [10] [11] [6], which is not the only one although is historically the most used. Other models were indeed proposed, from the Le Grand one [11], quite similar to Gullstrand's description to Liou-Brennan's [12] that is not taking into account the accommodation of the eye but is accounting for Aspherical aberrations, Astigmatism and Chromatic aberrations in the visible range, or to the more complete Navarro's [13].

2.4 The Aberrations of the Eye and Their Limitations

An important aspect that only the more complex models include in their analysis is the presence of *Aberrations*. Indeed, the eye is not a perfect optical system and the *Aberrations* could be defined as effects that comes from its non idealities. This consequently means that the PSF of the eye's optical system is not corresponding to the ideal one, a point, and that the resulting convolution of the input with this PSF, comparable to a thicker pencil stroke, is a blur image as shown in Figure 2.6.

A simple experiment could demonstrate that the eye is characterized, as each non-ideal optical system, by imperfection that modifies the distribution of the light on the retina and as a consequence that change the images quality. Being the eye considered as a lens that focuses on the retina the incoming light, those effects clearly affect also the reverse optical system, which is then used to recollect images of the retina. Shining a collimated green light source on the eye (wavelength $\lambda = 550$ nm), source that is completely covering the size of the pupil, it is possible to obtain a variation of the dimensions of the spot that is generated on the retina as a function of the pupil diameter, that is to say a variation in the PSF. According to the *Diffraction Theory* [2] the pattern generated corresponds to the Fourier transform of the aperture, in this case circular, generating the so called *Airy*

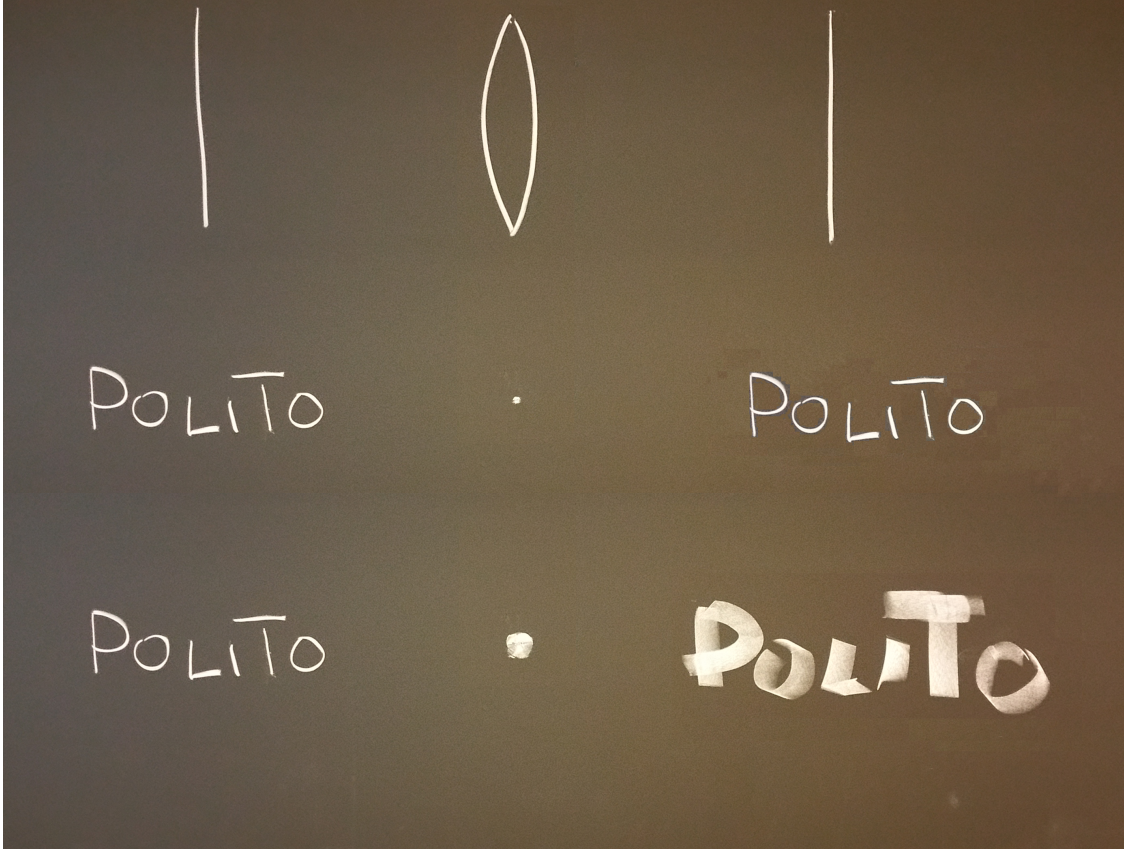


Figure 2.6. Comparison between ideal and non-ideal psf and resulting images

pattern, visible in Figure 2.7, the size of the produced principle spot (Airy disk) is inversely proportional to the size of the aperture, indeed the larger is the aperture the higher is the concentration of the energy of the Airy function into the first lobe, the Airy disk itself, and the smaller is this concentration region.

Although from this assumption it should be supposed that the larger is the pupil aperture the higher is the resolution that the human eye should be able to reach, Gross had shown something different. He demonstrated, taking into account the parameters coming from the Navarro model of the eye [13], that the minimum concerning the spot dimensions is reached for a pupil diameter around 3.5 mm [6] (Figure 2.8). This effect is due to contribution of the aberrations, which then becomes dominant with respect to the outcome of diffraction. The reason why this effects are of crucial importance is the consequent reduction of *Resolution* that is originated. Hence, to lead back the image resolution to the diffraction limit quality, the aberration introduced by the eye have to be corrected.

Moreover, to understand which is the way aberrations affect imaging quality bringing to a reduction of resolution, it is possible to see the problem from optical rays perspective. Indeed, to have a perfect image on the image plane, all the light rays that pass through the

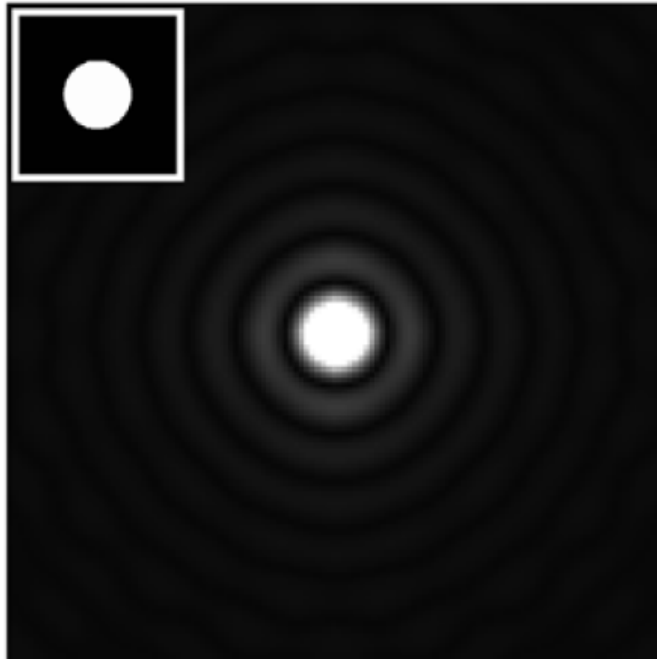


Figure 2.7. Fraunhofer diffraction pattern from circular aperture [14]

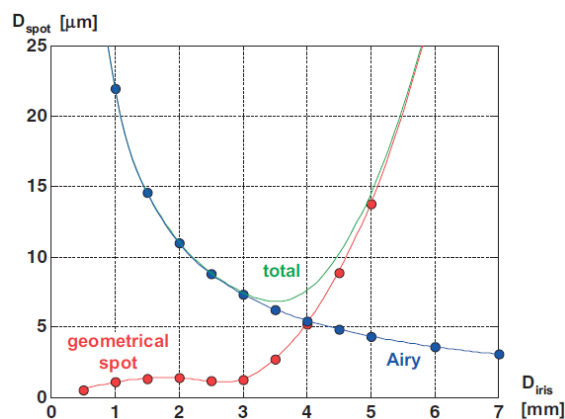


Figure 2.8. Spot diameter on the retina as a function of pupil size [6]

optical system in consideration, in this case the eye, should exactly converge in one point. As a consequence of this assumption, the constant phase regions always perpendicular to those rays should have a spherical shape. The discrepancy of the incoming phase wave-front with respect to the theoretical condition corresponds to the definition of the aberrations as it is clear from Figure 2.9. Hence, as Goodman underlined, the main effect of the presence of the aberrations is the generation of a *Phase Distortion*, which leads to a deterioration of the image quality of the imaging system, that is to say the fall of resolution.

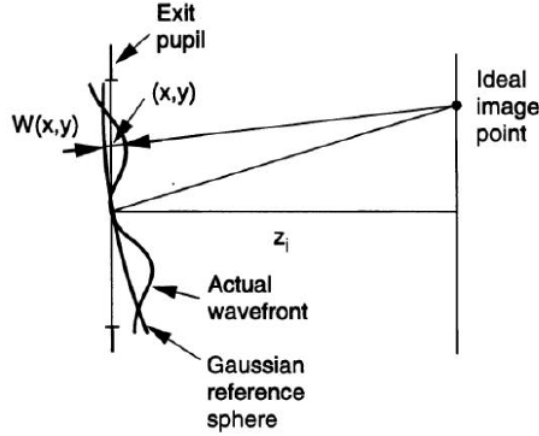


Figure 2.9. Representation of the aberrations [2]

Before presenting more into details the different aberrations that could also affect the eye, it is worth to mention that it is also affected by *Chromatic Aberrations*. This effect is due to the normal *Dispersion* of the media crossed by the light. The consequence are on-axis variations of the focus point position with the wavelength. This phenomena, according to Gross, has a negligible role in the worsening of eyes' resolution [6].

2.5 The Aberrations Description

The properties and characteristics of wave-front aberrations is deeply investigated by Aberration Theory. If a generic orthogonal reference system is defined for the complex optical system in analysis, defined with propagation direction along z axis and x axis pointing to the observer, it is possible to describe the wave-front exiting from the system in terms of *amplitude* and *phase* as in equation 2.28, where $A(x, y)$ represent the amplitude term and $\phi(x, y)$ the phase term.

$$f(x, y) = A(x, y) \cdot e^{j \cdot \phi(x, y)} \quad (2.28)$$

Starting from the equation 2.28 is then possible to evaluate the behaviour in a specified point p as follows in equation 2.29

$$f(x_p, y_p) = A(x_p, y_p) \cdot e^{j \cdot \phi(x_p, y_p)} \quad (2.29)$$

As was previously mentioned the aberrations theory refers only to the phase term $\phi(x, y)$. Usually the waves' aberrations are then defined from the phase term $\phi(x, y)$ as the relative discrepancy with respect to the correspondent paraxial spherical wave. Moreover, that difference is normally referred in unit of length as *Optical Path Difference* (OPD) obtaining the term $W_a(x, y)$. An important figure of merit for the aberrations evaluation

is then the $W_{RMS}(x, y)$ defined from equation 2.30 as the standard deviation of the wave-front.

$$W_{RMS}(x, y) = \sqrt{\langle W_a^2 \rangle - \langle W_a \rangle^2} \quad (2.30)$$

The perturbations of the original and ideal wave-front could be of different types, the ones of major interest are addressed in the following.

Tilt

The *Tilt* effect is generated by the system in a specified point if an angle θ is present between the paraxial reference spherical wave's ray and the one of the current wave-front; in this situation a linear component is produced on the wave aberration W_a .

Defocus

The *Defocus* effect is generated when the system affects the radius of curvature of the wave-front with respect to the one of the paraxial reference spherical wave. This effect is commonly addressed as Defocus since the image which is then produced will no longer be perfectly in focus because the convergence point has moved forward or backward depending on the sign of the aberration. In this situation a quadratic component is produced on the wave aberration W_a .

Astigmatism

Starting again with a generic reference system, with the z axis that is representing the direction of propagation and the x axis pointing at the observer, a reference ray going out from the system have to be chosen. If two angular apertures are defined from this reference ray, one occupying the sagittal plane the other the meridian plane, so on perpendicular to the other, and they are characterized by two different rays of curvature, the *Astigmatic* effect is produced. The effect of this phenomena is that the complete image will not be on focus in the same point but there will be one focus point for the sagittal components, one focus point for the meridian component and a region of minimum blur in the middle, between the two focus points.

Higher Order Aberrations and Zernike Polynomials

Many other aberrations of higher order exist, of different complexity and with different effects. A more systematic description of those kind of aberrations, which includes also the simple ones already presented, could be provided thank to the use of *Zernike Polynomials*. This theoretical constructions, which builds an *Orthonormal Basis* for the representation of the wave-front, is intertwined with a circular aperture description, hence, the polar coordinates are used. The wave-front can, as a consequence, be defined by a sum of terms accordingly to equations 2.31 and 2.32 [6]

$$W(r, \phi) = \sum_n \sum_{m=-n}^n C_{nm} \cdot Z_n^m(r, \phi) \quad (2.31)$$

with

$$Z_n^m(r, \phi) = \begin{cases} \sin(m\phi) & \text{if } m > 0 \\ \cos(m\phi) & \text{if } m < 0 \\ 1 & \text{if } m = 0 \end{cases} \quad (2.32)$$

2.6 The Correction of the Aberrations

The need for Aberrations correction has forced the birth of several techniques to perform the elimination of those wave-front errors that perturb the imaging process by lessening the resolution. The possible methods could be differentiated fundamentally into two main categories the Software based and the Hardware based. The former has on its side the reduced cost of the procedure but generally this cost is paid back, with respect to the latter, in terms of computational cost of the procedure. Hereafter, a possible example of computational correction will be briefly described before of the deep analysis of the Adaptive optics method used in this project.

Sharpness Based Criteria Algorithm

As a first step it has to be remembered that, accordingly to equation 2.33 the complex field at the image plane is equal to the complex field at the object plane convoluted with the correspondent of the electronics' concept of pulse response, the *Point Spread Function* $h(x)$ (PSF). Consequently, in the frequency domain, this relationship implies the Fourier transform of the complex field at the image plane to be equal to the product of the coherent *Amplitude Transfer Function* $H(k)$ (ATF) and of the the Fourier transform of the complex field at the object plane, as shown by equation 2.34. The variable k represent the Fourier conjugate variable of x .

$$f_{img}(x) = h(x) * f_{obj}(x) \quad (2.33)$$

$$F_{img}(k) = H(k) \cdot F_{obj}(k) \quad (2.34)$$

The aberrations are completely contained in the phase term $\phi(k)$ of $H(k)$, hence, according to Hillmann et al. it is only needed to multiply $f_{img}(x)$, which is obtain at the output of the system, for $H^*(k) = e^{-j\phi(k)}$. The objective of the algorithm is so to find the value of $\phi(k)$ which provides the best correction of the aberrations. Remembering the possibility to decompose the wave-front accordingly to Zernike polynomials base function as shown in equations 2.31 and 2.32 only the Zernike coefficients have to be found. To determine the required coefficients, has Hillmann suggested [15], an Entropy based approach could be used. Indeed, as Flores has shown, Entropy should be minimized for a good image quality [16], to do so, the derivative of the computed Entropy with respect to the Zernike phase coefficients was taken.

2.7 Adaptive Optics History and Evolution

“If the Theory of making Telescopes could at length be fully brought into Practice, yet there would be certain Bounds beyond which Telescopes could not perform. For the Air through which we look upon the Stars, is in perpetual Tremor ... The only Remedy is a most serene and quiet Air, such as may perhaps be found on the tops of the highest Mountains above the grosser Clouds” [17]

As those sentences show, the field of Adaptive Optics has its root in a discipline completely different from retinal imaging: Astronomical Observations. What Newton understood during his scientific observations was that the atmosphere introduces aberrations. Indeed, what he described as “Air Tremor ” corresponds to the turbulences produced by the different layers of the atmosphere. It provides a deflection of the incoming light rays which consequently bring to the reduction of the ability of telescopes to resolve the feature of interest, to a reduction of the imaging resolution. In the first phase of Astronomy, no solutions were available for this crucial issue, thereafter scientist had followed Newton’s suggestion: make the observation on the top of the highest available mountains to increase the probability of clearer skies and reduce the effects of atmospheric turbulences. Indeed, this is one of the reasons why the most important and scientifically active astronomical observatories, from La Silla and Paranal observatories in the Atacama desert (Chile), to the Mauna Kea observatory (Hawaii), passing from the Galileo Telescope of La Palma (Canarian Islands) or the Serra La Nava observatory on the Etna (Italy), have all being built on the top of great mountains. Although this, build those observatory on the top of the mountains is not the final solution for the reason that aberrations introduced by the atmosphere are still strong enough so to bring them to have the “same spatial resolution of a modest 8 inch (~ 20 cm) backyard telescope” [18]. Finally the solution was founded during the fifties. Indeed, in 1953 H. W. Babcock proposed an answer to this huge issue. He suggested the possibility of obtaining a compensation for the disturbance introduced by the atmosphere with the use of shape-varying optical elements that could adapt in real-time to the aberrations introduced by Newton’s “*Air Tremors*” . He certainly was the first to propose a possible solution, but it was plenty realized also thank to the parallel military development of the sixties that brought with same technique to the improvement of satellites’ images [19]. The idea proposed in both case was intrinsically simple: Evaluate the *Optical Transfer Function* (OTF) of the atmosphere and then dividing the OTF of the image for the one of the atmosphere [19]. The correction of the aberrations such performed has allowed to obtain astronomical results from grounded telescopes which are comparable with space telescopes’ ones, that obviously work without any interference of the atmosphere (Figure 2.10). The structure of an adaptive optics system is quite simple although definitely complex to be handled, it is constituted by two main devices: a *wave-front Sensor*, which has the duty to detect the aberrations introduced by the atmosphere, and *Deformable Mirror*, which instead has the role to correct them. As Max has pointed out, in the first realization of such systems a *Guide Star* was needed [18]. This technique was required to perform the measurement of the aberrations with the wave-front sensor with a reference source as bright as possible; with the correction performed the telescope would have been then able to observe also faint astronomic objects. The need for a guiding star, that introduced limitations to the region of the space that could be observed, was

brilliantly overcame in the eighties after the invention of the “laser guide stars” which took the place of the previously needed bright star, allowing then astronomers to observe all the regions of the space.

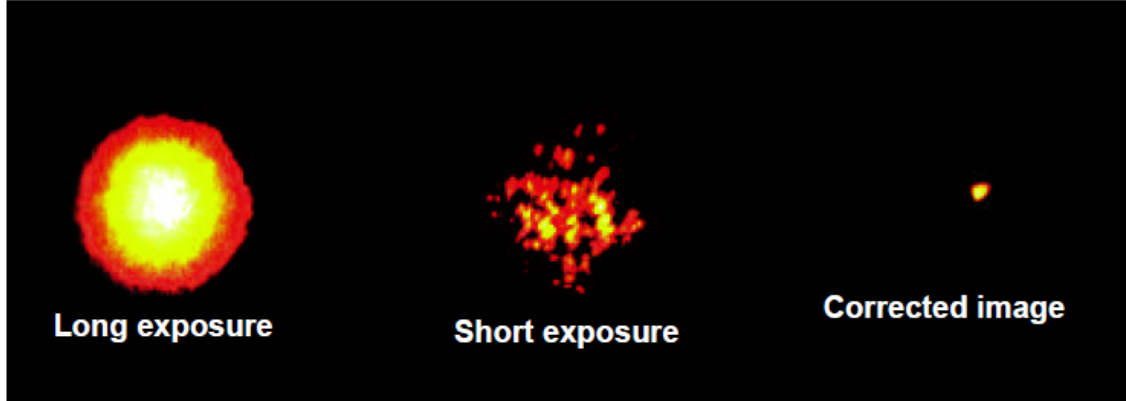


Figure 2.10. Bright Star (Arcturus) Observed with Lick Observatory’s 1-m Telescope California [18]

The Adaptive Optics technique is still today one of the most adopted for the construction of high resolution telescopes, but its application have been spreading into fields far from the original one. Indeed, as Tyson has noticed, since the late nineties the Adaptive Optics procedure has started to be used, as in this project, for ophthalmic applications as the retina imaging [20] or in general in Microscopy [21].

2.8 The AO Loop Components: Shack-Hartmann Sensor

The development of this fundamental component for the the realization of an Adaptive optics system was performed prevalently during the sixties by Mienel, Shack and Platt at the Optical Sciences Center of the University of Arizona under the request of US Air Force. The main military requirements that wanted to be addressed was referred to the problematic handle of satellite’s images which, as the astronomical ones, were strongly affected by the aberrations introduced by the atmosphere. The three scientist starting from the experiment proposed by Hartmann to find out the figure of merit of large telescopes, finally found the solution to the problem. The final sensor is constituted by two different layers. The first layer encountered by the incoming wave-front is the lenslet array, these series of small lenses is going to focus the light of the local wave-front on a point of the second layer, constituted by a two dimensional detector array (later, after its invention, by a camera sensor). the distance between the two layers corresponds to the focal length of the lenslet array, or better of each of its lenses. The lenslet array, which is partitioning the original incoming light, is then generating a series of focus spots on the detector. As Neal et al understood, “The key principle is that the position of these focal spots is directly

related to the average wave-front slope across the lenslet. Thus a measurement of the focal spot position uniquely determines the wave-front slope for that sample if the other system parameters are known” [22].

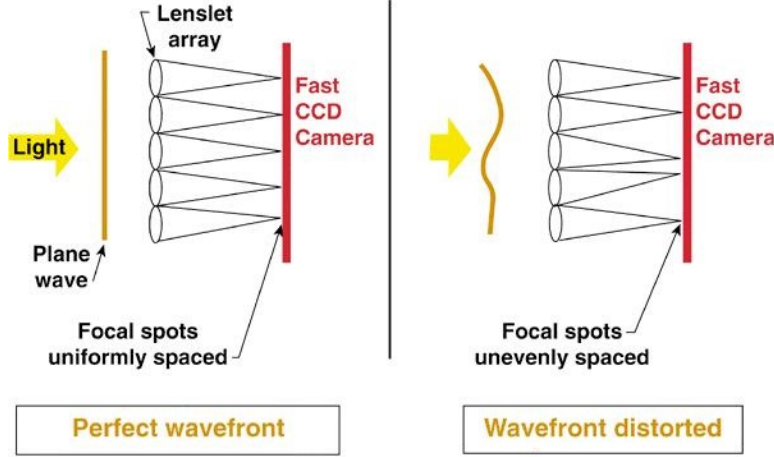


Figure 2.11. Shack Hartmann sensor principle and behaviour [23]

A two dimensional detector is used as a position sensor, commonly to accomplish this task a CCD detector is used. After the determination of the spot position and after, through the comparison with a reference, the evaluation of the local slopes, the wave-front could be reconstructed. More precisely, the output of the CCD detector is a matrix of pixel intensities $I_{i,j}$, from those intensities the spots positions in pixel coordinates $(x_{c,k}; y_{c,k})$ have to be evaluated. To do so the centroid of the spot have to be computed for each micro-lens k of the lenslet array. The evaluation of the centroids is done, for each micro-lens only considering the pixels that belong to the correspondent micro-lens, as a consequence, accordingly to Neal et al, it is possible to obtain equations 2.35 and 2.36 [22].

$$x_{c,k} = \frac{\sum_{i,j \in \text{lens}_k} x_{i,j} \cdot I_{i,j}}{\sum_{i,j \in \text{lens}_k} I_{i,j}} \quad (2.35)$$

$$y_{c,k} = \frac{\sum_{i,j \in \text{lens}_k} y_{i,j} \cdot I_{i,j}}{\sum_{i,j \in \text{lens}_k} I_{i,j}} \quad (2.36)$$

Having then the centroids of the current spots produced by the incoming wave-front it is possible, relating them to the ideal centroid, to evaluate the local slopes. The ideal centroid, which is located in correspondence of the centre of the micro-lens, corresponds to the focus point obtained with a perfectly flat wave-front. The local slopes that represent the average slope of the wave-front across the region defined by a single micro-lens k , are evaluated according to equation 2.37 [22].

$$\begin{cases} \langle \frac{\partial w}{\partial x} \rangle_k \approx \frac{(x_{c,k} - x_{r,k})}{L_H} \\ \langle \frac{\partial w}{\partial y} \rangle_k \approx \frac{(y_{c,k} - y_{r,k})}{L_H} \end{cases} \quad (2.37)$$

From the values of the local slopes is then possible to evaluate the commands that have to be used to feed the actuators in order to correct the measured aberrations and also to reconstruct the wave-front.

2.9 The AO Loop Components: the Deformable Mirror

The second essential component for the realization of the Adaptive Optics loop required for the correction of the aberrations, whatever is their source, atmosphere or human eye, is the *Deformable Mirror*. This component operates as the optical actuator for the physical correction of the disturbances. The actuation principle of the deformable mirror is to generate, thanks to the actuators below the optically flat surface, a curved shape which is complementary with the aberrations that have to be corrected. The consequence of this procedure is the almost total cancellation of the aberrations, depending on the “actuation resolution” of the mirror. The principle is shown in Figure 2.12.

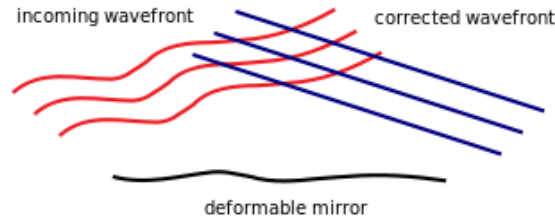


Figure 2.12. Principle of the Deformable Mirror operation [24]

Nowadays, *Deformable Mirrors* are generally classified into two different kinds: the segmented type and the continuous type. Both of them bring the same final result, although they could provide different qualities always accordingly to the application they are used for. The former is based on a basic configuration in which rectangular or hexagonal sub elements are constituting a segmented bigger mirror (Figure 2.13). Each of those sub mirrors has then one or different actuators that, depending on the different shape to produce to correct the aberrations, will independently move the the element with respect to the surrounding ones. The performances of the mirrors depends mainly on the frequency response of the mirror which is primarily determined by the stiffness of the materials and by the mass of the components. The use of this kind of structure is the most common approach for the realization of large aperture telescopes [25].

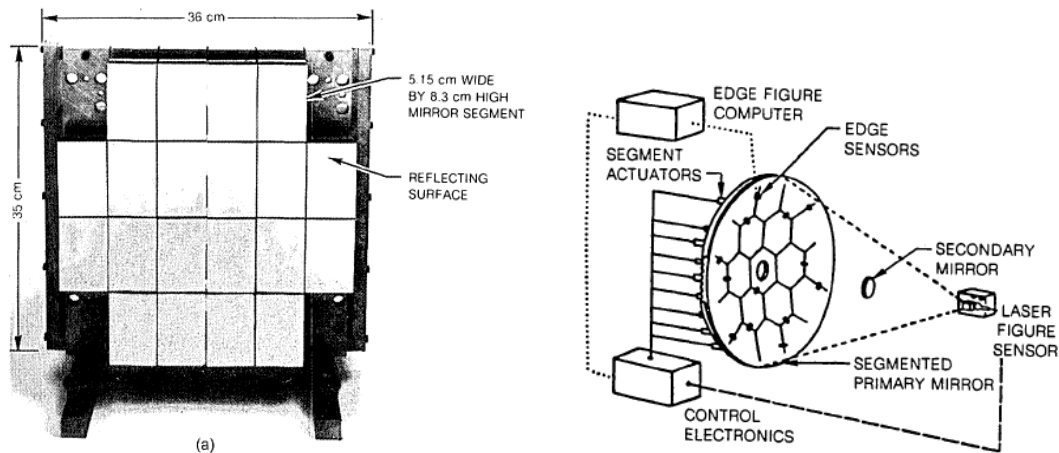


Figure 2.13. Example of a deformable mirror with rectangular elements [25] to the left, possible astronomical setup with hexagonal sub-elements deformable mirror [25] to the right

Instead, the latter is characterized by a continuous deformable surface. The advantage with respect to the previous case is that this kind of deformable mirror could theoretically follow the local slopes deformations providing a more accurate wave-front correction. The continuous surface deformable mirrors are of two different kind: the *monolithic piezoelectric mirrors* and the *thin surface mirrors with discrete actuators*. The first kind is characterized by the presence of a shared back electrode and by several vicinity electrodes in proximity of the surface to actuate; the voltage application will induce a piezoelectric deformation on the surface in correspondence of the activated electrode allowing to modulate the shape of the surface [26]. In the second case it is possible to identify singularly the different actuators. Those actuators could also be of different kind as shown in Figure 2.14: *Piezoelectric*, hence, based on the piezoelectric effect generated on specified materials with the variation of the polarity of applied voltage; *Electromagnetic*, which are based on a coil-spring system working into a magnetic field; *Magnetostrictive*, with a solenoidal actuation of a ferrite linked actuator; *Hydraulic*, based so on the force applied by a pressurized fluid.

A technology which is also in the way of development is a digital deformable mirror which would have no more to withstand the analogical difficulties of the other kind of devices, adding also the possibility to easily interface it to the elaboration unit [25].

The Deformable Mirror that will be used during the realization of this project is the *Mirao 52e, Imagine Eyes*. As it is generally the case in ophthalmic application, this device is a continuous surface deformable mirror. It is based on the operation of *Electromagnetic Actuators*. The realized shape can be tuned thanks to the control of the voltage applied to each of the actuator. Indeed, below the optically flat surface 52 magnets are positioned. Each of their location is in exact correspondence with respect to a electromagnetic coil. The application of a voltage to the coil provides the passage of current, which, in turn, generates a magnetic field that is then going to modify the position of the magnets. The modulation of the voltage in the actuation range allows then to obtain the required shape

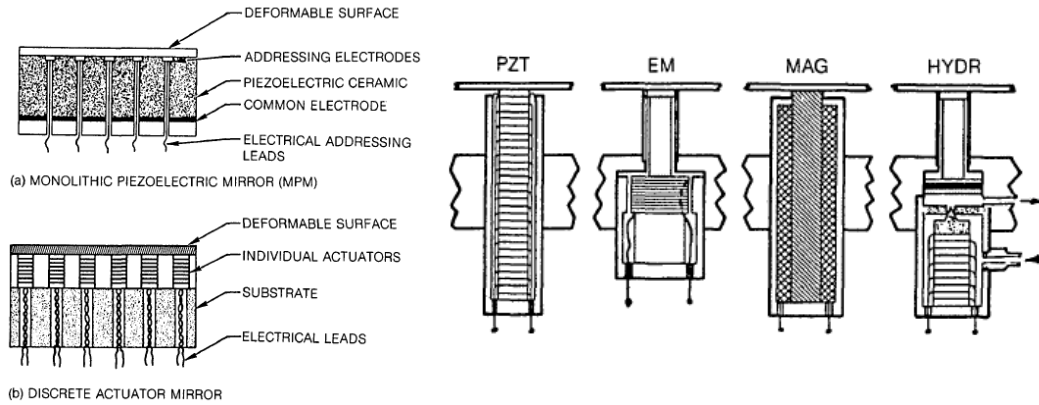


Figure 2.14. Types of continuous surface deformable mirrors [25] to the left, possible kind of actuators [25] to the right

from the deformable mirror. The simplified representation of the structure of this device is shown in Figure 2.15.

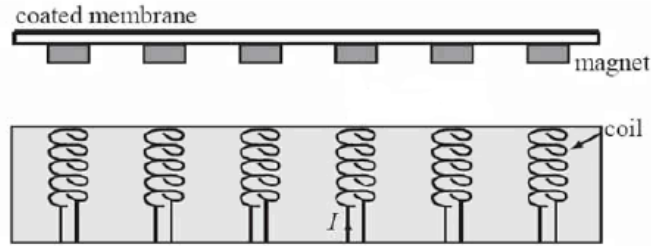


Figure 2.15. Structure of the *Mirao 52e*, *Imagine Eyes* deformable mirror [27]

2.10 Phase Reconstruction Techniques

As said at the end of Section 2.8, after having the values of the slopes it is possible to determine not only the commands to feed the actuator, the deformable mirror, but also to reconstruct the phase of the wave-front. Generally it is possible to distinguish two different kind of algorithms for phase reconstruction: the *Zonal* approach, and the *Modal* one. Both the two kind of algorithms depends strongly on the position at which the slopes are evaluated, that on his own is depending on the kind of sensor that is used, because, as Suthwell has underlined, it influences the “slope measurements sampling geometry” which then gives a different set of known points to start with for the reconstruction [28]. For a Shack-Hartmann wave-front sensor the configuration of the given slopes mesh is the one shown in Figure 2.16.

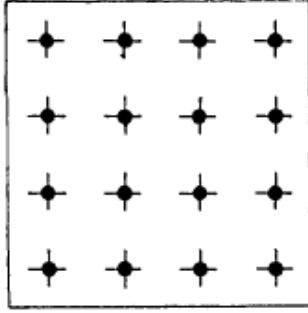


Figure 2.16. Slope measurements sampling geometry and wave-front mesh points [28]

The problem to be solved in the *Zonal* approach is “to least-squares-fit the slope measurement data to some function or model of the phase given at its grid points” [28]. Hence, the phase reconstruction depends on the way the phase itself is represented in between two known points. Supposing a quadratic phase representation in between the mesh grid values, equation 2.38 is obtained.

$$\phi = c_0 + c_1 \cdot x + c_2 \cdot x^2 \quad (2.38)$$

$$S_x = c_1 + 2 \cdot c_2 \cdot x \quad (2.39)$$

Since the slopes, referred by equation 2.39, of this hypothetical phase distribution along x are known, it is possible, with the grid configuration of Figure 2.16, to get the values of c_1 and c_2 . Thus, it is possible to obtain equations 2.40 and 2.41, and to use them to obtain a least-square solution for ϕ_{ij} [28].

$$\frac{(S_{i+1,j}^x + S_{i,j}^x)}{2} = \frac{(\phi_{i+1,j} - \phi_{i,j})}{h} \text{ for } i = 1 : (N - 1) \ j = 1 : N \quad (2.40)$$

$$\frac{(S_{i+1,j}^y + S_{i,j}^y)}{2} = \frac{(\phi_{i+1,j} - \phi_{i,j})}{h} \text{ for } i = 1 : (N - 1) \ j = 1 : N \quad (2.41)$$

Meanwhile, the solution of the problem in the *Modal* case resumes the utilization of a modal basis such as Zernike one. The solution is found by differentiating the phase modal expansion and equating it to the known value of the slopes, from those equations is then possible to find the modal coefficients to be used.

Chapter 3

Implementation of the AO Loop

As mentioned in Chapter 1 the final goal of this work is the implementation, starting from the functions library provided by *Imagine OpticsTM*, of the software to control the Adaptive Optics loop that has to correct the aberrations of the eye before the retinal image acquisition phase. This developed software has to replace the existing used proprietary software. The reasons of this replacement are related mainly to two aspects. The first one concerns the future integration of the Adaptive Optics loop with all the other subsystems that are concurrently working to reach the common goal of a good retinal imaging. The second is conceptually related to the will to understand the way the correction of aberrations is performed and to the desire for the user to influence the choices taken during the correction. Indeed, the “black box” behaviour of the existent software does not allow to understand the reasons beyond certain failure conditions, as the one related to the maximum applicable voltage to the deformable mirror that will be discussed in Section 3.8.

The initial requirements for the realization of the work are related to the ability of the loop to perform the correction at least in ex-vivo condition. This first level of realization allows to avoid considering the temporal variation of the real eye’s aberrations and thus introduces a level of simplification for the realization of the goal. To simulate the theoretical behaviour of the eye, as ex-vivo conditions, a lens (*AC254 – 050 – A – ML*, $f = 50.0$ mm) was used. Moreover, to simulate the reflection conditions of the retina a white paper was positioned at the focal length of the used lens. A second important requirement was related to the need that the loop’s computations were sufficiently fast in order to properly fit with the complex set of operations that leads to the image acquisition. Furthermore, it was also requested to address the choice of the parameters influencing the loop behaviour in order to allow the final user to set them as easy as possible, changing the configuration of the loop. After having addressed those requirements a further level of complexity was added passing to the in-vivo behaviour analysis. It was initially found that the simple behaviour set for the ex-vivo case was not suitable for the in-vivo configuration and that several of the functions used started to provide errors in different conditions. As a consequence of those problems a series of “security checks” were added to the loop in order to avoid it stopping during the analysis. In this Chapter, after an initial presentation of the whole

retinal imaging device in Section 3.1, of the Library used in Section 3.2, of the recognized limitations of the existent proprietary software and of the basilar loop working principle performed, each of those taken measures will be discussed during the description of the implemented loop software. More precisely in Section 3.3 the main steps required and developed for the loop to work will be presented. After that, in Section 3.4, the attention will be moved on the handling of the initialization procedures necessary before the starting of the loop of correction. Afterwards, one of the main issue of the process, the treatment of the *spots' matrix*, will be discussed in Section 3.5. The following phase required for the loop will then be presented in Section 3.6, that will concern the evaluation of the local slopes, in Section 3.7, which will discuss the phase reconstruction of the wave-front and in Section 3.8, that will deal with the actuation steps. Finally, a brief description of the built *Graphical User Interface* (GUI) for live-imaging will be provided in Section 3.9.

3.1 The Retina Imaging System

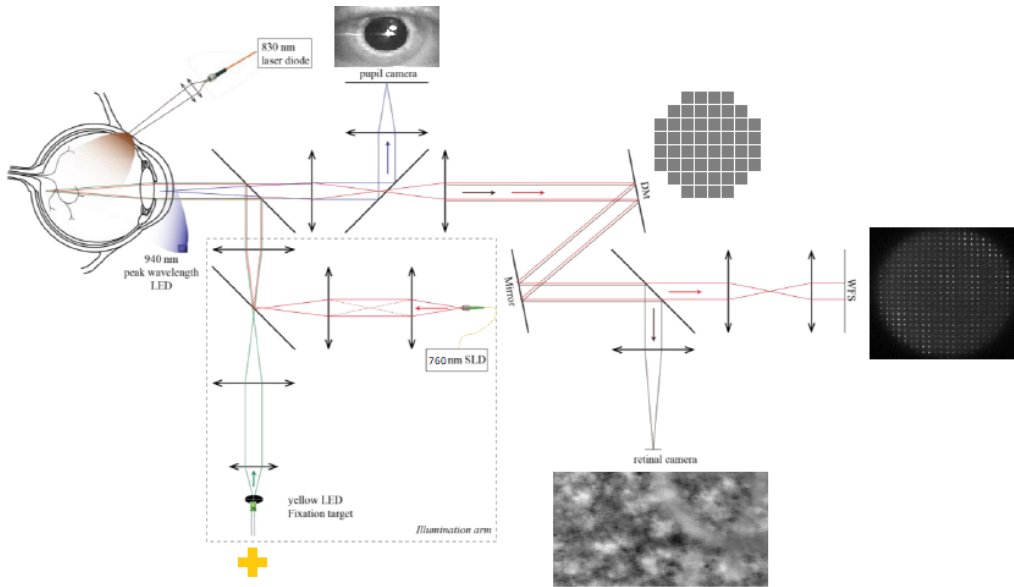


Figure 3.1. complete scheme of the system [1]

The retina imaging system in consideration, as it is possible to see in Figure 3.1, is characterized by several subsystems. Each of those provides a substantial contribute in order to perform the in-vivo measurement. Moreover, it is important to underline that those system are not working in parallel without any interaction, but that the retinal images are obtain as a consequence of the cooperation of those subsystems. Among them the fundamentals are the followings:

- Pupil Illumination Setup and Pupil Camera.
- Transscleral Illumination Source and Control.
- Adaptive Optics Loop.
- Imaging System.

3.1.1 Pupil Illumination Setup and Pupil Camera

The Pupil is externally lighted with an IR led ($\lambda = 940 \text{ nm}$). The goal of this illumination is to have the possibility to align and exactly center the position of the eye at the beginning of the measurement thanks to what is recollected by the pupil camera. Indeed, the live images acquired by the Pupil camera is shown on the control computer and allows the user to mechanically correct potential misalignment of patient's pupil due to macroscopic movements. Referring to the complete schematic of the system the optical rays' path from the Pupil external illumination and the correspondent Pupil camera for the position detection are connected by the blue lines (Figure 3.1).

3.1.2 Transscleral Illumination Source and Control

A software handles the switching of the laser diodes sources that provides the transscleral illumination needed to perform the imaging procedure. Those sources of illumination are again in the IR portion of light spectrum with a wavelength of $\lambda = 830 \text{ nm}$. Given the wavelength of the source it is important to consider all the safety limits concerning the in-vivo exposure of the human eye to the chosen radiation. Those limits are for instance regulated by the *International Standards* [29]. Those kind of standards define what is called the *Maximum Permissible Exposure (MPE)*, that given as an energy density (J/cm^2) or power density (W/cm^2), is defined to be well below the damage threshold. In order to reduce as much as possible the power which is delivered to the eye, so that the measurements is not only safe but also comfortable, the transscleral laser source is not used in continuous mode. In fact, the lighting source is normally handled with the *duty-cycle* technique. This duty-cycling is related also to the developing of the adaptive optics loop because of the necessary synchronization of the two entities. Referring to the complete schematic of the system the Transscleral illumination sources and the following schematic series of optical rays produced by that illumination are shown in brown; it is clearly evident that the path of those rays is then concluded onto the retinal camera (Figure 3.1).

3.1.3 Adaptive Optics Loop

This subsystem is used to perform the correction of eyes aberrations, it is constituted by a *Deformable Mirror* (*Mirao 52e, Imagine Eyes*) and by a *Wave-front Sensor* (*HASO4 FIRST*) that works in a closed loop configuration. The light source for this subsystem is provided by a Super Luminescent LED (SLD) ($\lambda = 760 \text{ nm}$). To perform in a better

way the acquisition of the retinal images, the behaviour of this subsystem is intrinsically correlated to the others in terms of timing. As previously mentioned dealing with those components is the main interest of this development, for this reason its characteristic and properties will be extensively discussed later. Referring again to the complete structure of the system it is possible to understand the path followed by the optical rays produced by the SLD source as red lines. Those clearly originated by the SLD arrive on the *Wave-front Sensor* passing on the *Deformable Mirror* (Figure 3.1).

3.1.4 Imaging system

Finally, the imaging system is characterized by the *retinal camera* (*ORCA Flash, Hamamatsu*) and by the software which controls its focal alignment and the images acquisition. The camera is mounted on a moving platform which is differently aligned according to the depth of the layer that has to be analysed and that as a consequence should be in focus. The possibility to take images at different depths of the retina structure allows to have the possibility to see, with cellular resolution the properties of the corpuscular structures of the retina. Before to obtain the final result, the images taken from each of the illumination points, which retrieval is performed in sequence during the acquisition phase, should be post processed. The first step of the post processing is the averaging of the images acquired after the evaluation of the misalignment caused by the movement of the patients' eye. The following step is the phase reconstruction. To perform this phase a regularization process is required [1] [30]. As previously said the retinal camera receive the back scattered light from the retina provided by the transscleral illumination system (brown in the schematic of Figure 3.1) as well as the yellow light provided by a fixation target source, which is used to create a yellow cross fixation target to be followed by the eye of the patient.

3.2 Description of the Library

To fulfil the goal of the realization of the *Adaptive Optics Loop*, an existing library of functions will be used. This library has been provided by the producer of the two main elements of the loop: the *Shack-Hartmann Wave-front Sensor* and the *Deformable Mirror*, *Imagine OpticsTM*. The *Wave-kit* library from *Imagine OpticsTM* contains several functions that could be used for the development of applications with the previously mentioned devices. Each of those functions has to be considered as a “black-box” since the only information provided are the nature of input and outputs (Figure 3.2); as a consequence, intuition has been a necessary element to understand the nature of the arising errors that those functions were providing during the building of the loop.

Those functions are organized in various classes depending on their properties and on the goal of their use. It is possible to characterize them according to the cluster of operations they belong to. This classification by clusters will be the useful to understand which are the main phases and operations that the loop has to tackle and accomplish in order to work properly. Among them, the fundamental clusters are:

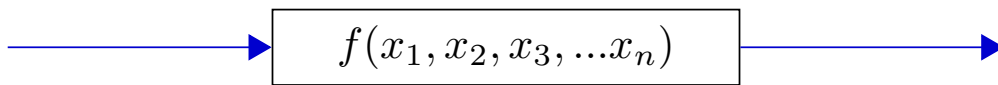


Figure 3.2. Schematic of the functions

- Interfacing the Camera
- Interfacing the Wave-front Corrector
- Computing and Manipulating the Wave-front Slopes
- Computing and Manipulating the Wave-front Phase
- Adaptive Optics Processing

Interfacing the Camera

This cluster of functions, belonging to different classes, is characterized by tasks and routines related to the properties of the *Wave-front Sensor*. The methods here recollected are divided into two classes. Belong to the first class the methods to access: the camera specifications, as the dimensions of the sensor, the bit depth or the maximum frame rate; the camera features and list of actions that could be accomplished; to the camera parameters names and options. Moreover, belong to the second assemblage all the methods that are used to “Get ” and “Set ” the different values of interest for the Wave-front Sensor’s camera.

Interfacing the Wave-front Corrector

The cluster that recollets the methods related to the Wave-front Corrector, that in this case is represented by a *Deformable Mirror*, is organized similarly to the one related to the Wave-front Sensor’s camera. Again it is possible to recognise two main classes, the first one incorporating all the functions that could be used to retrieve the fixed parameters, the features and all the set of available information regarding the used device; the second one gathering together all the routines used to really interface the device.

Computing and Manipulating the Wave-front Slopes

This cluster groups together all the methods which are related to the evaluation and processing of the local slopes as a consequence of the matrix of spots which is the output of the *Wave-front Sensor* camera.

Computing and Manipulating the Wave-front Phase

Instead, this assembling gathers together all the methods that are relative to the computation of the phase of the Wave-front. It offers several opportunities which are related to the different kind of existing methods to fulfil the goal of passing from the grid of local

slopes to the phase. Indeed, several algorithms are provided. Among them, possible choices are the *Zonal* or the *Modal* approaches, previously presented in 2.10.

Adaptive Optics Processing

It is then worth to mention, as a possible cluster, the group of methods that build the core of the *Adaptive Optics Loop*, which are also related to the *Control Theory* aspects of the problem. Belongs to this ideal group of methods all the function related to the calibration procedure and above all to the evaluation of the commands from the previously mentioned Slopes, commands that have to be provided, later, to the actuator (*Deformable Mirror*).

The code has been written using *Matlab*[®] because of the ease of handling experimental data and images during the building from scratches of the system. This has been possible thanks to the fact that the provided library also includes a set API functions that allows the interface between the compiled *.dll* library and *Matlab*[®] software. Moreover, since the provided library was compiled by the producer in a *32bit* format, it is required, to avoid incompatibility errors during the loading of the library and to effectively work with it, to use a *32bit* version of the *MathWorks*[®] release. As a consequence the work will be developed on *Matlab*[®] 2013a version.

3.3 Main Steps of the Loop

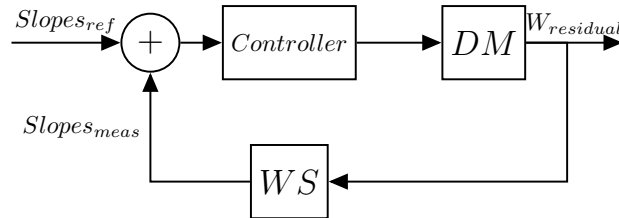


Figure 3.3. Skeletal hardware schematic of the loop

The loop skeletal structure is constituted by the presence of the *Deformable Mirror* and of the *Shack-Hartmann Wave-front Sensor*. The input of the system is considered to be the reference wave-front’s slopes. This reference was taken with a “10x objective” (Olympus, NA = 0.25, 10x) which pupil was perfectly aligned to the pupil plane; moreover a paper was then put at the objective operative distance, which was founded both checking that the paper was in focus on the conjugated retinal camera and that the fixation target (refer to Subsection: 3.1.4) was in focus on the paper; this last procedure is related to the attempt to get a condition close to what will happen with the real eye, which is going itself to focus on the fixation target. The created reference is then saved in the proprietary format “has” typical of the slopes object for the used library. The reference is then compared

with the slopes that are evaluated from the spots’ matrix image resulting from the Shack-Hartman wave-front sensor. The difference between the two slopes corresponds to the slopes of the residual aberration wave-front that remains to be corrected. At this point, an important role is played by the controller that converts those residual slopes into the “*Delta Commands*” that have to be applied to correct the residual error with respect to the reference. Moreover, the application of those evaluated commands provokes the movement of the deformable mirror’s actuators. As a consequence of the actuation a new wave-front is sensed by the Shack-Hartmann device and the loop continues consistent with itself. The output of the system could be considered as the residual wave-front, which is provided by the deformable mirror. The figure of merit that is used to evaluate the theoretical quality of this system is the residual RMS error evaluated on the residual wave-front (refer to Section: 2.5). The structure of the system is shown in Figure 3.3. Each of the blocks presented in Figure 3.3 embeds then a series of operations that have to be done to accomplish the working of the system. A more precise yet not completely exhaustive view of the whole loop’s operations could be seen in Appendix B. To simplify the description, the whole developed loop behaviour could be distinguish in a series of phases that are shown in Figure 3.4. Each of those phase has been implemented using the provided functions. In addition, the steps underlined in green in Figure 3.4 requires a further attention. Indeed, those phases required the additional implementation of security checks and of short cuts in order to overcome some of the issue that were characterising the originally used proprietary software.

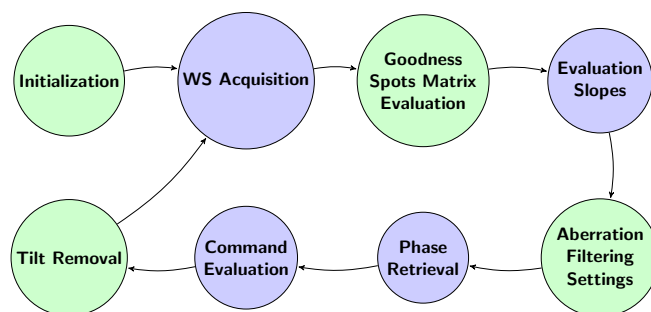


Figure 3.4. Main steps of the loop

3.4 Initialization Phases

The first problem to tackle is the Loading of the *Imagine Optics™* library containing all the functions, methods, classes and definitions that are going to be used during the implementation of the loop structure. After the loading procedure was also introduced a statement to check if this loading phase has gone well. Thus, to prevent the system from crashing, in the worst case scenario the loop would have been stopped before really starting the initialization phase. If the library is correctly loaded the main code has thereafter

access to all the functions it needs to interface the devices. Then, after all the definition for particular types have been performed, all the flags and default parameters are set and the main important variables are preallocated. Hereafter another essential step have to be performed. To create the virtual objects that contain all the method available for the current used devices and that provides all the required information when asked, it is strictly needed to load two critical files, one for the wave-front corrector one for the wave-front sensor. Those two *Configuration Files* are indispensable for the loop to work, therefore, if they are not correctly found, the loop will again be stopped before completing the initialization phase and far before starting the correction procedures. If, instead, they are correctly found, the procedure is enabled to continue. Moreover, to add flexibility to the code, it has been chosen to set the possibility for the user to fix the location of those files or to chose it at each run of the loop software. The following step after the loading of the two *Configuration Files* is the setting of all the parameters that will influence the loop behaviour [31] [32]. The most essentials are the following ones:

- Exposure time of the wave-front sensor’s camera
- Number of images that the wave-front sensor’s camera has to average for each acquisition
- Time-out of the wave-front sensor’s camera
- Number of modes that have to be used during the loop
- Wanted loop gain value
- Sleep time of the mirror after actuation
- Aberrations filtering conditions for the slopes evaluation

Again to guarantee flexibility to the software it was allowed to the final user to decide and insert those parameters when asked or to let the loop use the default parameters. It is important to define that, according to what described by the library introduction [33], the *number of modes* is corresponded to the number of actuators out of the available amount that will be used to perform the correction. For the *Mirao 52* device used in this case the amount of available actuators is 52 [31]. The lower is the number of modes, the worse is the correction performed, the better the mirror response; the higher the number of modes used, the more precise the correction performed, the worse the stability response of the mirror. As a consequence, the choice of the number of modes have to be done as the result of a trade off between quality of the correction and stability of the performances. Moreover, the maximum number of modes, thus the number of actuators used is strongly influenced by the eye’s properties of the patient.

Following the choice of user’s parameters or of default ones, the next phase contemplates the creation of the “camera object” for the wave-front sensor’s camera and the setting of the chosen parameters before of its initialization. An important parameter that is set during this phase is the *trigger* of the this device. Several option are available [32], but to synchronise the behaviour to what required by the whole subsystems collaboration, it is

set by default to “external rising edge”. Although this choice, it is still possible to modify this setting in the initial part of the code. Furthermore the camera acquisition type is set.

After the creation of the camera object and the initialization of the wave-front sensor device, the same procedure has been followed for the deformable mirror actuator. Hence, the “mirror object” is created and then the device initialized. To fully configure the behaviour of the mirror a calibration of the reaction of each of its actuators have to be performed or the file containing these information have to be load. Those information are commonly referred in *Control Theory* as *Interaction Matrix*. This matrix is practically storing the data related to the generalized effect of the actuation of each of the actuators of the mirror. Those effects have to be taken into account during the evaluation of the commands for the deformable mirror’s actuators. Indeed, to evaluate them the *Interaction Matrix* have to be inverted [34]. For the final configuration of the loop software it has been chosen to follow the second chance, to load a previously recorded *Interaction Matrix*, both for a time saving reason and for a practical reason. The most stringent one is the latter, due to the fact that the input configuration required to calibrate would have been completely different with respect to the measurement one (in-vivo case). Moreover, the calibration is stable in time and have to be done again only if major changing are performed on the hardware constituting the loop. Again, to maintain higher flexibility, the final user has the possibility to chose the location of this essential file or to keep the default location; a flag it is used to discriminate between the two choices.

The user has then another option, keeping the set or default value for the exposure duration of the wave-front sensor’s camera, or letting it to be automatically set. This functionality has been added to address a measuring time reduction during the in-vivo measurements, overcoming as a consequence a bottleneck of the proprietary software. Indeed, using this option it is not required to follow the trial and error procedure that was previously used to set the proper exposure time. The auto-exposure setting behaves as in the following. The user has the possibility to chose two boundaries limits that corresponds to a lower an an upper bound in terms of pixels saturation. This two values are so directly related to the dynamics of the camera pixels. Knowing that the amount of photons received by each pixel, and so its percentage of saturation, depends not only on the light conditions but also on the exposure duration of the CCD sensor used, it is possible to determine the first exposure that allows to theoretically stay in between of those two limits. Moving from the the initially set exposure or from the default one the system starts a little loop in which: an image is acquired, an average of the maximum saturation is evaluated on the highest “*nb_extreme_pixels*” saturation values detected (“*nb_extreme_pixels*” which corresponds to the number of pixel taken into account could be set initially). This average saturation in then compared with the two boundaries previously set and consequently the exposure duration is changed. the loop is stopped when the exposure set is sufficient or not to high to stay in the fixed boundaries of saturation (Figure 3.5).

Another important task that anticipate the starting of the correction loop is the loading of the reference. Again to achieve a better flexibility the user, has the possibility to take the reference snapping an image with the camera or to load a previously saved reference. The former case is not suitable for the in-vivo final application because it will reduce the available effective surface on which the correction could be done (intersection between the

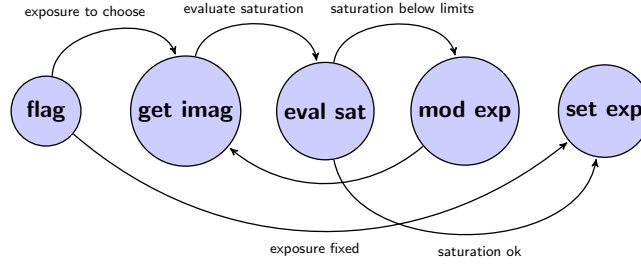


Figure 3.5. Schematic of the “auto-exposure” loop

pupil of the reference and the pupil coming from the loop iteration). Hence, the latter choice is set as default option. After the loading of the reference, the local slopes could be evaluated on it, ready to be later used as a comparison during the phases of the correction loop. This setting concludes the enumeration of the most significant steps that the final code performs as initialization procedure of the loop, exception done for a task that will be discussed later in Section:3.5.

3.5 Dealing with the spots’ matrix

After that the settings described in Section: 3.4 are completed, the effective loop of correction could be started. It is worth to mention that a simple *Matlab*[®] script does not allow to create an infinite loop and then to stop it and continue another series of operations. Thus a finite number of iteration loop was created. Instead, concerning the in-vivo imaging process that has to be performed allowing the possibility to stop the loop when the acquisition is completed, still being able to save the data acquired during the loop, a *Matlab*[®] GUI was created, and it will be discussed in the Section: 3.9. At the beginning of the loop, after the handling of the loop index parameter, the current image is acquired. For this important step two options were implemented: simply take in consideration the last image generated on the Wave-front Sensor, or acquire an image that was previously saved. The latter is a condition that has been used prevalently during the outlining phases in order to test in specified conditions the behaviour of the loop. Consequently the default setting for the normal behaviour of the software is the former one, which is fixed at the beginning of the code. The acquisition of the image is followed by the retrieval of the image pixels intensities as shown in Figure 3.6.

As it is clear from Figure 3.6, the results between the two measurements conditions are different. Indeed, in the ex-vivo case the whole sensor is exposed to the light and as a consequence the spots’ matrix occupies the largest possible pupil, limited by the hardware structure; on the other hand in the case of the in-vivo measurements the size of the spots’ matrix is limited by the dimension of the patient’s pupil.

At this point it is essential to perform a clarification. Indeed, if the system has to work for ex-vivo condition, it is theoretically possible to skip everything that follows and to refer

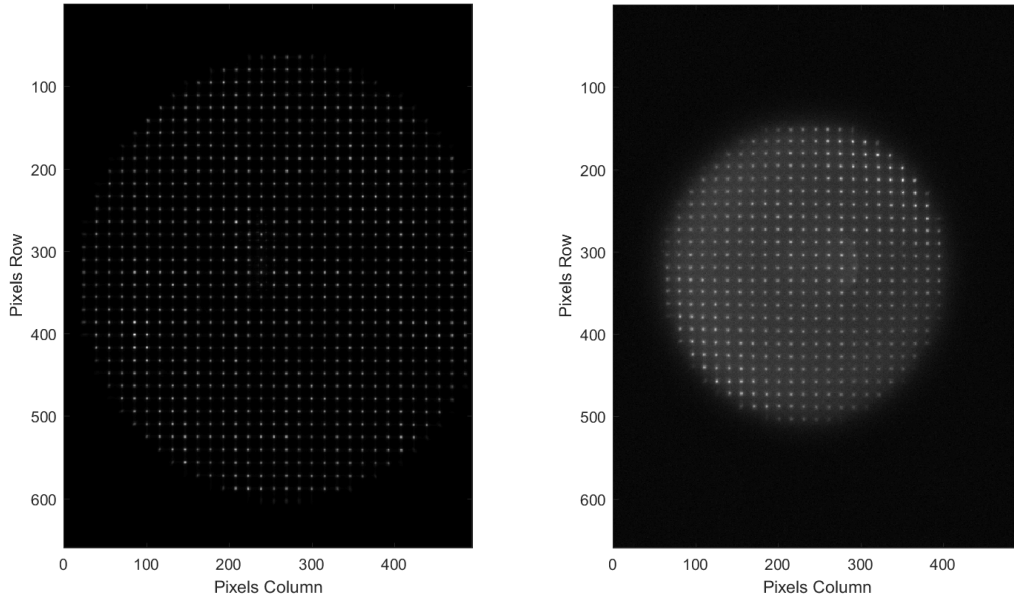


Figure 3.6. Example of resulting spots' matrix in the case of ex-vivo fake eye on the left (exposure time = 2.35 ms, SLD power continuous mode = $28 \mu\text{W}$) and in the case of in-vivo real eye on the right (exposure time = 10 ms, SLD power continuous mode = $20 \mu\text{W}$)

directly to the phase of evaluation of the slopes from the image which is tackled in Section 3.6. However, the real goal of the system building is being able to perform measurements in-vivo, consequently several aspects that differentiate the two measuring conditions have to be handled.

It is a matter of fact that the behaviour of the eye is not static but is dynamic, it means that the conditions in which the system should be able to work are more complex and that it should be able to adapt to those conditions still providing a correction of the aberrations as good as possible. First of all it has to be bore in mind that the dimensions of the pupil will change with time due to the *Accommodation* procedure previously discussed (Section 2.2). Besides, it is also worth to mention that the patient could obviously blink, that is to say that the eye could be closed for a few moments during the measurement. This to conditions produce modifications on the spots' matrix that is recorded by the Wave-front Sensor. Above all the second condition, the *blinking*, implies a loss of signal that could negatively influence the detection and the evaluation of the slopes. Indeed, in those cases, the functions related to the computation of the slopes, that will be presented in Section 3.6, will provide errors and the system will be suddenly stopped. To avoid that, conditions that allow to distinguish the images related to an almost close or completely close pupil from the good ones have to be found. With the goal of finding possible figures of merit inherently the differences between those conditions, several images were acquired and saved with the Wave-front Sensor. The complete series of images that allows to see the progressive changes into the spots' matrix, and so identify the blinking phase, it is shown

in Appendix A, Here are reported the main ones that allows to get the differences between the two cases.

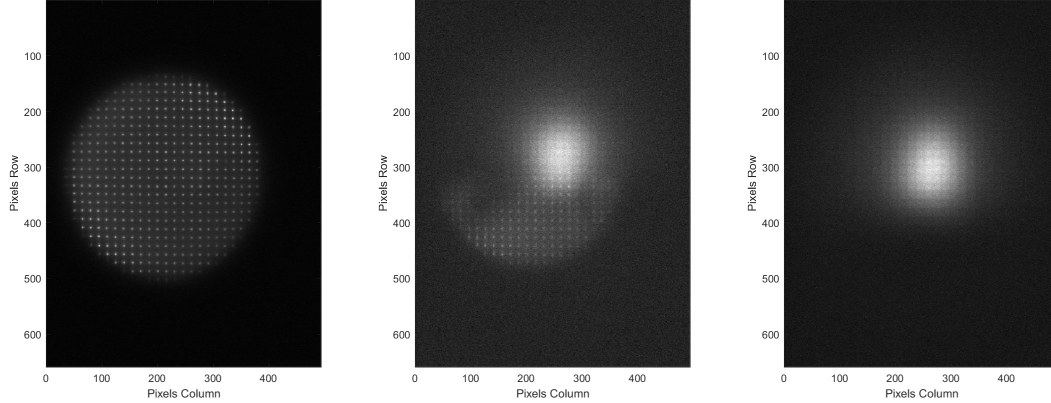


Figure 3.7. Comparison between the spots' matrix obtained in the normal case (left), when approaching the blinking (centre) and when the eye is closed (right) (exposure time = 10 ms, SLD power continuous mode = $20\mu\text{W}$). For the full series of images of the evolution of the spots' matrix during the blinking see Appendix A

As it is clearly possible to see in Figure 3.7, the two conditions are characterized by a completely different spots' matrix. The analysis of the two different situations brought to think about four different possible figures of merit that could be used to check if a blink is occurring:

- Number of Spots Detected
- Percentage of Sensor Surface Illuminated
- Pixels Saturation
- Shape of the Pupil

Before presenting each of those figure of merit into details, in order both to show how their variations are detected and how their values are used to influence the choice of maintaining the current spots' matrix or to discard it, it is worth to mention the reason why they came out to be possible parameters to accomplish the task. From the images compared in figure 3.7, it is clearly possible to notice a difference into the configuration of the information. In the case of what is assumed to be a good image it is clearly possible to see a series of spots highly in contrast with respect to the background, while in the case of a "blinking spots' matrix" the conformation of the image changes and the series of spots giving way to a more concentrated illuminated region at the centre of the image. This modification could be clearly related to a variation of the number of spots and to a variation of the percentage of the surface illuminated. Furthermore, it is undoubtedly that the blinking phase is going to change the shape of the pupil. Since literally the patient

is closing his eye, a prevalence of the horizontal dimension on the vertical one is the a consequent result. Finally, it has also been notice that the light redistribution due to the scattering and the reflection on the eyelid cause a variation of the amount of light reaching the CCD sensor and, as a consequence, of the saturation of the pixels.

3.5.1 Number of Spots Detected

As already mentioned, the estimation of the number of spots characterising the matrix could be considered as a possible figure of merit. To account for them it is necessary to start from the matrix of pixels' intensities that has been retrieved. The evaluation of the number of spots embeds the consideration of the amount of entities on a binary plane. To perform such operation a binary image have to be created starting from the pixels' intensities matrix. To create this binary image a specified threshold have to be set in order to establish if the current pixel intensity I_{ij} is or is not above that threshold. If the pixel intensity I_{ij} is above the binary threshold it will account for a one in the binary image if not it will account for a zero. Before to discuss how the real estimation is performed it is important to stress how the threshold is defined. The first step to set it is to take into account the range of intensities of the current image, this way the threshold will not be set absolutely but relatively to the current spots' matrix, being as a consequence more effective. Hence, the maximum intensity for the current spots' matrix is evaluated and the threshold for intensity set according to equation 3.1.

$$threshold_{intensity} = I_{ij,MAX} \cdot factor_on_intensity \quad (3.1)$$

Where $I_{ij,MAX}$ represents the maximum value of intensity recorded in the current image at coordinates (i,j) and $factor_on_intensity$ a percentage factor to set the threshold. This factor has been experimentally set to 0.27, meaning that the threshold will be set to the 27% of the maximum intensity recorded.

Thereafter, having set the binary threshold, it is possible to compute the binary image following the simple idea shown in Pseudo Code 3.1.

Listing 3.1. evaluation of the intensity binary image

```

for (all the pixels)
    if(current intensity of the pixel > binary threshold)
        binary_image(current position) = 1;
    else
        binary_image(current position) = 0;
    end
end

```

Then on the binary image it is possible to determine the number of spots using *Matlab*[®] function *bwlabel()*, obtaining as result the number of spots for the matrix. In Figure 3.8 and Figure 3.9 are reported examples of the final results of this operation of a “good” in-vivo matrix and on a “bad” in-vivo matrix.

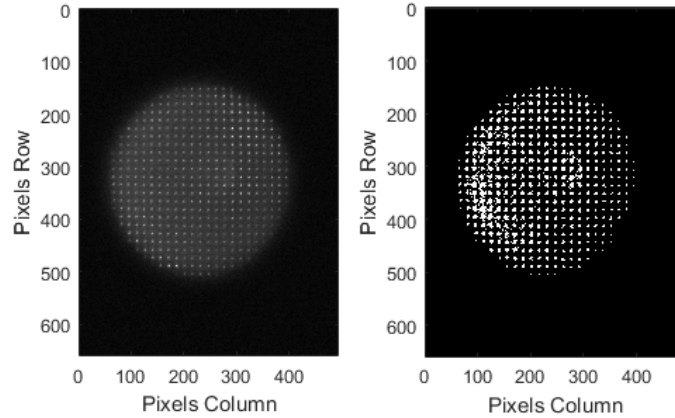


Figure 3.8. Result of the Number of spots threshold on a “good” in-vivo matrix; Number of Spots detected = 1158 (exposure time = 10 ms, SLD power continuous mode = $20 \mu\text{W}$)

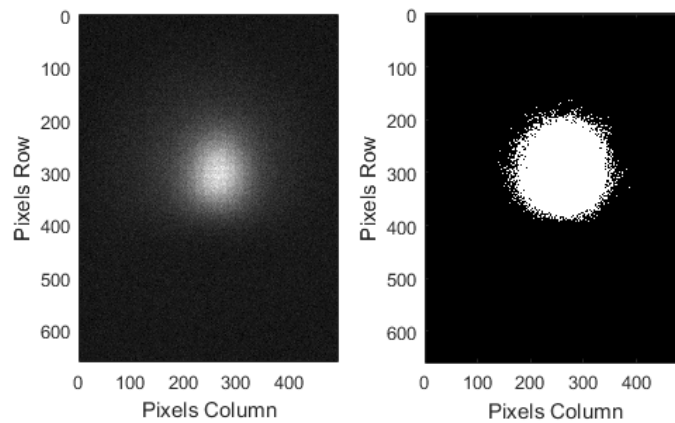


Figure 3.9. Result of the Number of spots threshold on a “bad” in-vivo matrix; Number of Spots detected = 738 (exposure time = 10 ms, SLD power continuous mode = $20 \mu\text{W}$)

Afterwards, having a method for the evaluation of the first figure of merit, it is possible to establish when this figure of merit is good and when it is not. Firstly, it has to be

taken in consideration that the number of spots detected varies also with the experimental conditions and with the patients, for this reason before the beginning of the correction loop, and after the auto-exposure setting it has forced a process that evaluates the number of spots on a certain number of images (it is possible to change this number at the beginning of the code), and then evaluates the average number of spots detected on this amount of images. From this averaged number is then possible to set the threshold “good” / “bad” as shown in equation 3.2. The value *perc_thr_avg_num_spots* is another parameter that could be modified.

$$threshold_{numspots} = num_spots_{average} \cdot perc_thr_avg_num_spots \quad (3.2)$$

3.5.2 Percentage of Sensor Surface Illuminated

A second figure of merit that was identified is related to the percentage of the sensor that receives high intensity light in the two cases of “good” and “bad” spots’ matrix. Indeed, if the matrix obtained is good, it is easily possible to distinguish a series of high intensity points and a reduced intensity background. If, instead, the matrix received is not proper for the evaluation, the region of high intensity is more extended and no more characterized by a spotted pattern. Therefore it is possible to distinguish the two cases. The procedure followed in this case is similar to the one discussed in the case of the number of spots (Subsection 3.5.1). Again there is the need for the creation of a binary image and for this reason the binary image threshold is evaluated following equation 3.3, quite similar to equation 3.1.

$$threshold_{surface} = I_{ij,MAX} \cdot factor_on_surface \quad (3.3)$$

Where $I_{ij,MAX}$ represents the maximum value of intensity recorded in the current image at coordinates (i,j) and *factor_on_surface* is a percentage factor to set the threshold. This factor has been experimentally set to 0.6, meaning that the threshold will be set to the 60% of the maximum intensity recorded. This choice has been made to really distinguish the case in which a matrix of spots is obtained from the one in which the closure of the eye modify the structure. Later, the binary image is generate following the mindset described by Pseudo Code 3.2

Listing 3.2. evaluation of the surface binary image

```

for (all the pixels)
    if(current intensity of the pixel > binary threshold)
        binary_image(current position) = 1;
    else
        binary_image(current position) = 0;
    end
end

```

Then, on the binary image it is possible to determine the percentage of illuminated surface thanks to a trick. The occurrence of “ones” in the binary image are evaluated and compared with the total amount of pixels available ($659 \cdot 494 = 325546$), this leads to a percentage of surface. In Figure 3.10 and Figure 3.11 are reported examples of the final results of this operation on a “good” in-vivo matrix and on a “bad” in-vivo matrix.

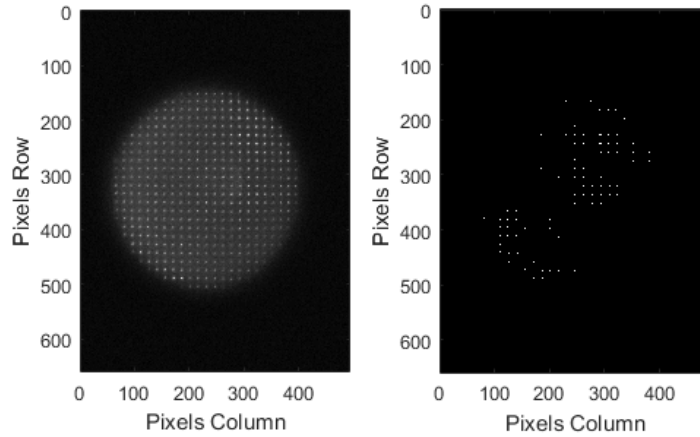


Figure 3.10. Result of the Surface threshold on a “good” in-vivo matrix; Surface percentage detected = 0.1471% (exposure time = 10 ms, SLD power continuous mode = $20 \mu\text{W}$)

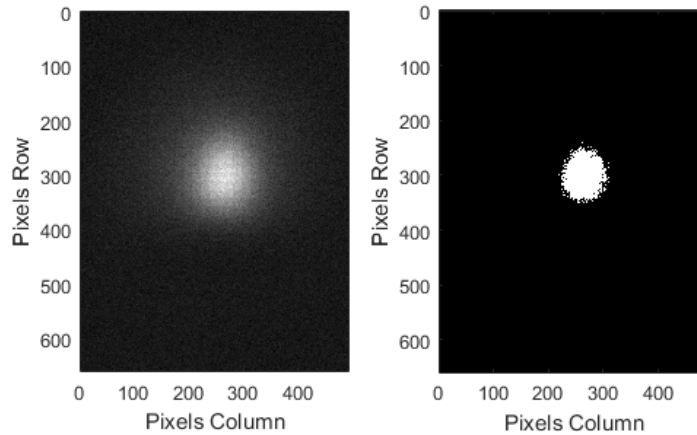


Figure 3.11. Result of the Surface threshold on a “bad” in-vivo matrix; Surface percentage detected = 1.8068% (exposure time = 10 ms, SLD power continuous mode = $20 \mu\text{W}$)

Hereafter, having a method for the evaluation of the percentage figure of merit, it is possible to establish when this figure of merit is good and when it is not. Again it has

to be taken in consideration that illumination conditions of the sensor varies also with the experimental conditions and with the patients, for this reason before the beginning of the correction loop, and after the auto-exposure setting it has forced, as in the case of the number of spots determination, a process that evaluates the surface percentage on a certain number of images (is the same of the one for the number of spots), and then evaluates the average illuminated surface percentage on this set of images. From this averaged number is then possible to set the threshold “good” / “bad” as shown in equation 3.4. The value $perc_thr_avg_percentage$ is another parameter that could be modified.

$$threshold_{surfacepercentage} = surface_percentage_{average} \cdot (1 + perc_thr_avg_percentage) \quad (3.4)$$

3.5.3 Pixels Saturation

Being relative figures of merit, that is to say quantities relative to the maximum intensity detected, the number of spots described in Subsection 3.5.1 and the surface percentage described in Subsection 3.5.2 are not fully recording what is happening during the blinking phase. Indeed, during the blinking phase, the increased reflection and scattering provided by the eyelid implies a reduction of the light received by the sensor. This phenomena could be experimentally shown. Considering the series of spots’ matrix used to describe the blinking phenomena (refer to Appendix A), Figure 3.12

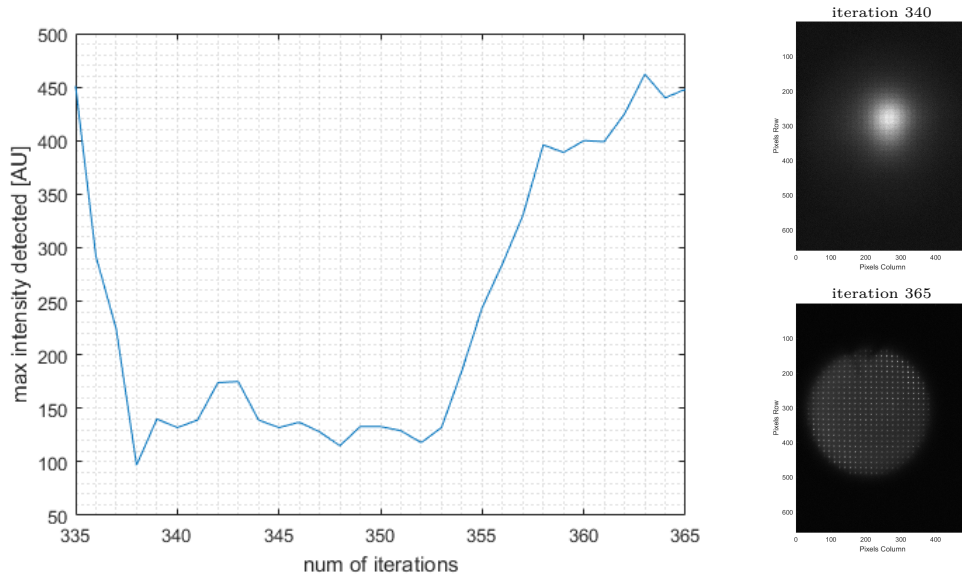


Figure 3.12. Variation of the pixels intensity during a blinking phase, spots’ matrix from Appendix A (exposure time = 10 ms, SLD power continuous mode = $20 \mu\text{W}$)

As a consequence of this behaviour, the saturation percentage of the pixels is evaluated at each iteration in order to monitor it. When it goes below a threshold (The user could change it at the beginning of the code), the image is considered not suitable for the processing since for very low saturation, and so for very low amount of light on the CCD sensor, the functions related to the evaluation of the slopes provides errors of the kind “No Signal” .

3.5.4 Shape of the Pupil

The last figure of merit that has been introduced to track the behaviour of the eye and to recognise a blink is related to the shape of the spots’ matrix obtained on the sensor. Researchers has shown that the roundness of the pupil is approximately perfect [35]. Therefore a strong variation of the shape of the spots’ matrix is generically referable to blinking conditions. To evaluate it the following procedure has been followed. Four reference points are determined on the spots’ matrix, those points corresponds approximately to the north, south, east and west limits of the spots’ matrix. Those points are determined as the first points in the specified direction for which is valid the condition: intensity below threshold before, intensity above threshold currently. the value of the threshold could be set by the user.

Listing 3.3. shape analysis algorithm

```
row = 2;
col = 2;
while(row < limit row & North Not Founded)
  while(col < limit col & North Not Founded)
    if(I_pixel(row, col) > threshold & I_pixel(row-1, col) < threshold)
      North = current pixel
    end
    increment col;
  end
  col = 2;
  increment row;
end

row = 2;
col = 2;
while(col < limit col & West Not Founded)
  while(row < limit row & West Not Founded)
    if(I_pixel(row, col) > threshold & I_pixel(row, col-1) < threshold)
      West = current pixel
    end
    increment row;
  end
  row = 2;
```

```
    increment col;
end

row = 2;
col = max_col-1;
while(col > 2 & East Not Founded)
    while(row < limit row & East Not Founded)
        if(I_pixel(row, col) > threshold & I_pixel(row, col+1) < threshold)
            East = current pixel
        end
        increment row;
    end
    row = 2;
    decrement col;
end

row = max_row-1;
col = 2;
while(row > 2 & South Not Founded)
    while(col < limit row & South Not Founded)
        if(I_pixel(row, col) > threshold & I_pixel(row+1, col) < threshold)
            South = current pixel
        end
        increment col;
    end
    col = 2;
    decrement row;
end

evaluate horizontal diameter;
evaluate vertical diameter;
calculate shape parameter;
if(shape parameter is below threshold)
    evaluate and assign centre spots' matrix;
end
```

Afterwards, the absolute value of one minus the the ratio between the horizontal diameter and the vertical diameter is evaluated. If the resulting value is close to zero the shape of the pupil is acceptable, while, the far this value is from zero the more probable is a blinking occurrence. The exact evaluation of the shape parameter is reported by equation 3.5

$$shape_parameter = \left| 1 - \left(\frac{horizontal_diameter}{vertical_diameter} \right) \right| \quad (3.5)$$

Besides, the centre of the spots' matrix is also evaluated from the coordinates of the 4

extremis points. The results of this phase are presented in Figure 3.13 and Figure 3.14 for a normal spots' matrix and for a "bad" spots' matrix respectively.

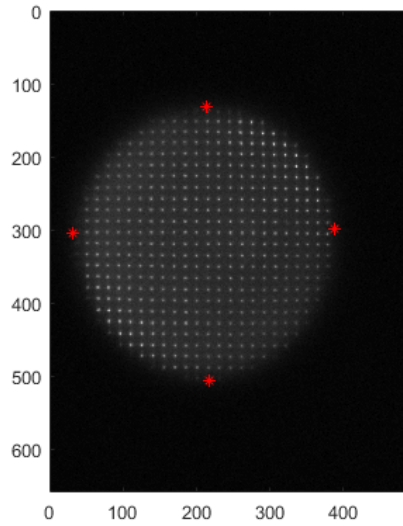


Figure 3.13. Shape analysis for a "good" spots' matrix; shape parameter obtained = 0.0452 (exposure time = 10 ms, SLD power continuous mode = $20 \mu\text{W}$)

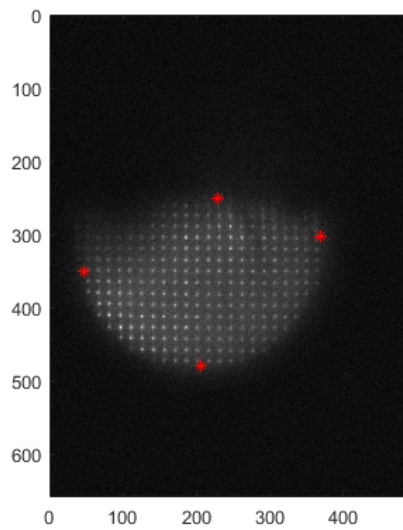


Figure 3.14. Shape analysis for a "bad" spots' matrix; shape parameter obtained = 0.4 (exposure time = 10 ms, SLD power continuous mode = $20 \mu\text{W}$)

3.5.5 Consequences of the Methods

To be considered good, the spots' matrix obtained on the sensor should respect all the conditions previously presented. This limitation guarantees that, although each of the figure of merits is not covering all the possible outcomes in terms of possible spots' matrix, their combination allows to avoid the most critical cases. In the chance one of those figure of merits tells that the current spots' matrix is not suitable, the current image will be discarded and the previous good image will be considered as the current one.

3.6 Evaluation of the Slopes

After having agreed upon the goodness of the spots' matrix using the parameters described in Section 3.5, it is possible to prosecute in the analysis of the code. The successive step that have to be accomplished is the evaluation of the slopes. To perform this essential task the software library provides two different functions. The first one is characterized by the possibility to optimize the memory usage and thus the speed of the operation since it works on variables already allocated. The drawback of this function, according to the library providers, is that it could work properly only if at least the 30% of the surface of the sensor is illuminated [33]. As a consequence, the use of this function could have possible effects on the loop behaviour. The second function available in the library is characterized by a major reliability, but, since it is working differently in terms of memory handling, it is far slower with respect to the first one [33]. This effect is due to the fact that the function itself is providing a new allocation of the necessary object each time it is called, it means at each iteration of the loop. To overcome the limitations of both function and provide a compromise in terms of reliability and speed it has been decided to use the former function, the faster, in case the spots' matrix is considered “good” ; while to use the latter, the more reliable, if at least one of the figure of merits previously presented is warning about the nature of the spots' matrix. This choice has been made also considering that sometimes, when the blinking is approaching, the last image that is taken as a “good” image could represent a partial pupil and thus possible tricky conditions for the faster function could arise. This default choice can be changed by the user, who can still decide to use in any case the faster function.

Another important aspect of the procedure to perform the evaluation of the slopes is that the system requires a starting reference point to initialize the computation. Thus a possible issue could arise if the default starting point, which is maintained theoretically fixed, is not sufficiently illuminated or the correspondent region of the spots' matrix is missing. To overcome this occurrence two procedure are developed. The first one is setting the starting point according to pixel intensity values in a specified region close to the centre of the spots' matrix. The dimension of the region used to chose the initial point is related to a parameter that could be modified by the user, this parameter is then used to build a square region around the point identified as the centre of the current spots' matrix evaluated accordingly to Subsection 3.5.4. The second procedure other is taking into account the pixels intensity on the full matrix of points. The reference point has to be provided to the system in terms of micro-lens coordinates, not as pixels coordinates.

Hence, it is required to proportionally evaluate this quantity starting from the pixel chosen for intensity reason. Considering the dimensions of the CCD sensor to be equal to $659 \cdot 494$ pixels, and taken into account that the lenses are $40 \cdot 32$ it is possible to establish a simple linear proportionality.

Finally, still concerning the slopes evaluation process, the last step performed is the subtraction between the current slopes coming from the current wave-front that has produced the current spots' matrix, and the reference slopes (see Section 3.3). Slightly before performing this operation, the aberrations for whom it is not interesting to correct are removed from the slopes objects. This means that it is possible to perform a filtering of the aberrations not of interest. Both for the reference slopes and for the current slopes it is possible to filter:

- Tilt x
- Tilt y
- Curvature
- Astigmatism 0°
- Astigmatism 45°
- Higher Order Aberrations

Each of those aberration could be filtered or maintained. In the first case its presence will be completely neglected, thus meaning that the mirror actuator will not correct for it; while in the second case the aberration correlated will be taken into account and as a consequence corrected by the deformable mirror's actuators. The possibility to handle a specific filtering gives rise to an increased flexibility, allowing to face different situations. Those choices refers to the classification of aberrations performed accordingly to Zernike basis. The first orders aberrations are shown in Figure 3.15.

As a consequence of the choices available it is worth to analyse the aberration filtering in the perspective of the results and aftermaths on the retinal imaging. The first aberration to take into account is the *Piston*. Its effect could be considered completely negligible on the retinal imaging because it provides only a DC component to the actuators' commands, although this it is important to verify its presence or absence for what concerns the total voltage applied to the mirror, issue that will be tackled in Section 3.8. The second aberration that is encountered is the *Tilt*. Also this aberration does not provide any dangerous effect on the retinal imaging results. Indeed, the main consequence of the presence of a Tilt component is the horizontal shift of the spots of the WS' output and so an horizontal shift of the resulting retinal image, effect that could be easily corrected during the post-processing phase thank to the realignment of the stacks' images. The effect on the spots is shown in Figure 3.16.

The choice of not accounting for the Tilt during the correction theoretically allows also the reduction of the total voltage applied to the mirror, issue that will be tackled in Section

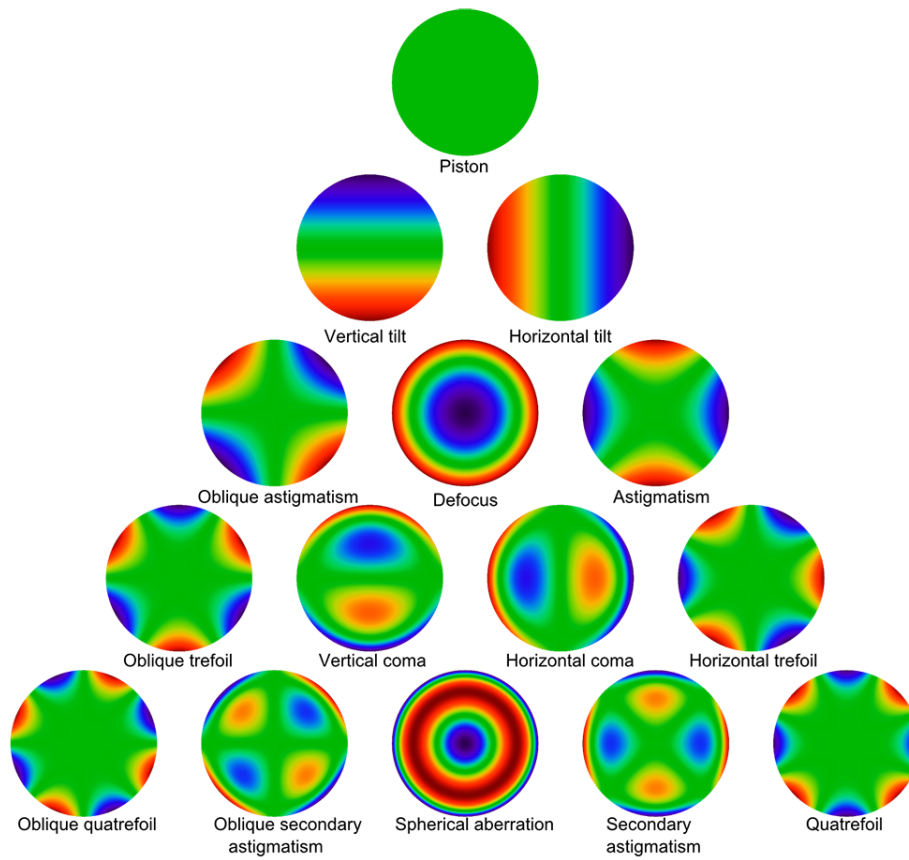


Figure 3.15. Principle aberrations according to Zernike basis [36]

3.8. Instead, the errors introduced by all the others aberration are not easy to be corrected without the use of the deformable mirror, reason why the should be taken into account during the correction phase and so not filtered from the evaluated slopes.

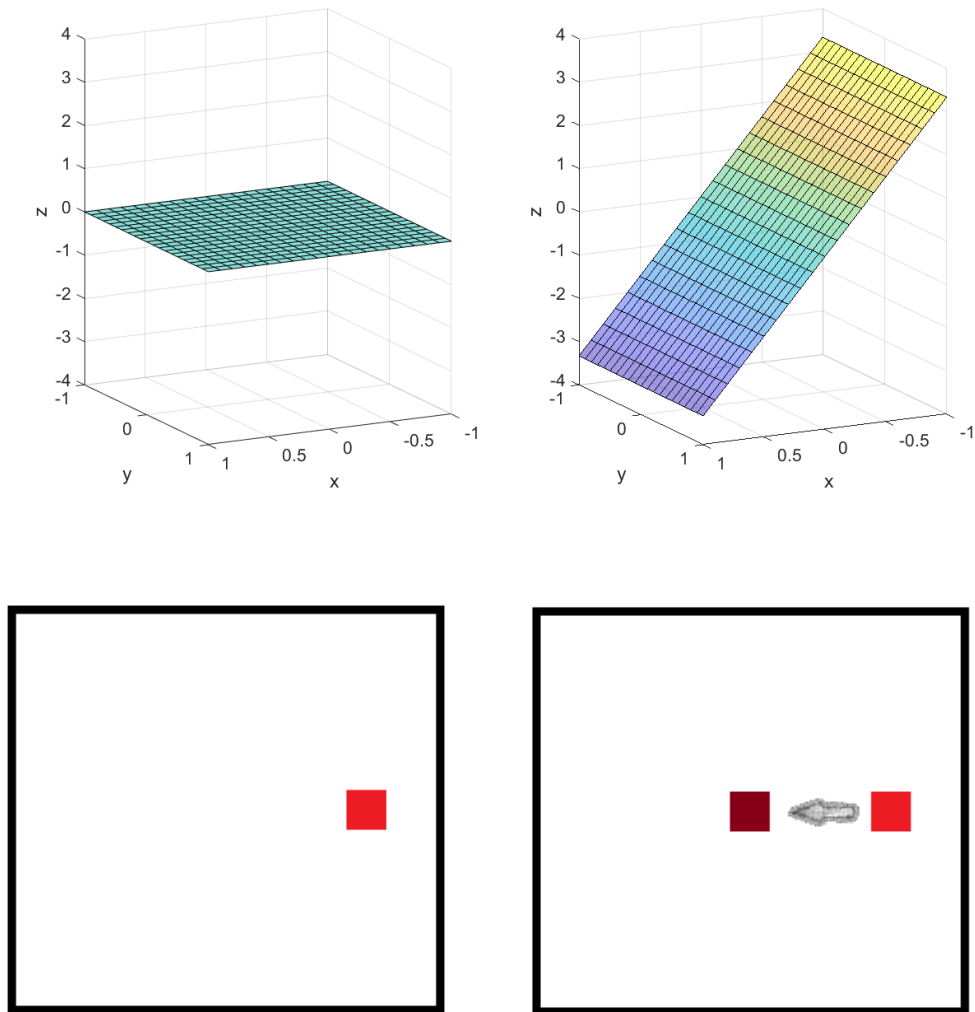


Figure 3.16. Principle of the spots shifting

3.7 Phase Reconstruction

Immediately after the computation of the slopes the generated loop's software has enough information to reconstruct the residual differential phase related to the difference of the slopes just estimated. To perform this task several options are provided to the user, who has the possibility to chose between 3 different approaches: *Zonal*, *Modal Zernike based* and a combination of the previous two. The default choice, which is then the one used for all the measurements in-vivo, is the *Zonal* configuration. This choice has been made because

of the nature of the pupil visualized on the sensor. Sometimes, for instance when the eye is moving or starting a blink what is perceived on the sensor is not perfectly rounded, and this imperfections are kept if they are not overcoming the limits imposed by the shape analysis previously described. It means that, although the *Zernike - Modal* approach provides a more precise evaluation of the phase, it is not completely suitable for the case of study. On the contrary, the *Zonal* approach which is base on the algorithm presented in Section 2.10, is more flexible and thus more suitable for the measuring conditions. The drawback is a reduced precision in the phase reconstruction due to the approximation done during the process. The third option possible is related to a combination of the two approaches, which result in a slightly more precise evaluation but bring a noticeable reduction of the speed of the loop, condition that is not tolerable for the system. As a consequence of these considerations the final choice has fallen on the *Zonal* approach. Moreover, the reconstructed phase is not directly plotted by default, not to weigh the software execution down. Although this the user could decide to modify this choice, in this case it will be plotted each 10 iterations in order to provide a trend of the behaviour. To have a reference about the correction performed a statistical analysis of the phase is handled and the corresponding RMS error provided.

3.8 Moving the Actuators

The following step that has to be performed by the loop software is the computation of the commands (voltage values) that have to be applied to the deformable mirror to perform the correction of the aberrations. Those commands are directly evaluated from the slopes previously determined thanks to one of the provided functions. Relatively to this procedure, it is relevant to stress a few aspects that have to be bore in mind. The actuation process has a few limitations that directly came from the physical limits of the device used. The deformable mirror has 52 actuators, each of them with an available range of $-1\text{ V} \div 1\text{ V}$ [31]. An option have been added to limit the usable dynamics of the actuator to a certain percentage of their maximum limits. Moreover, for power handling problems the maximum total voltage that could be applied to the whole mirror, in absolute value, is of 25 V [31]. If this limit is reached or overcame the system will crash. Among those two specification coming from the construction of the device, the most limiting is the second one. Indeed, the occurring of this condition causes the stop of the correction loop, and, as a consequence, the retinal images are acquired without correcting for the aberrations. Thus, a huge loss of resolution is caused. Moreover, the time required to start again the loop may also invalidate the whole imaging procedure. For this reason, in order to overcome the crashes happening in those situations with the proprietary software, it has been implemented a way to constantly measure and monitor the maximum amount of voltage applied to the mirror. Indeed, retrieving at each iteration the absolute position of the mirror actuators in terms of voltage commands and then evaluating the sum of the absolutes values of those commands, it is possible to have an essential trace of the behaviour of the mirror. Furthermore, to avoid the loop to crash because the limit of 25 V is reached, and so to eliminate any further consequence on the retinal imaging acquisition, it was set a “security threshold” for the maximum amount of voltage applicable. When this threshold is reached, the mirror actuators are reset to their zero positions. Indeed, it is

better to lose the correction for the few iterations required for the convergence than to have the loop crashing during the measurements. The principle of this taken countermeasure is shown in Figure 3.17.

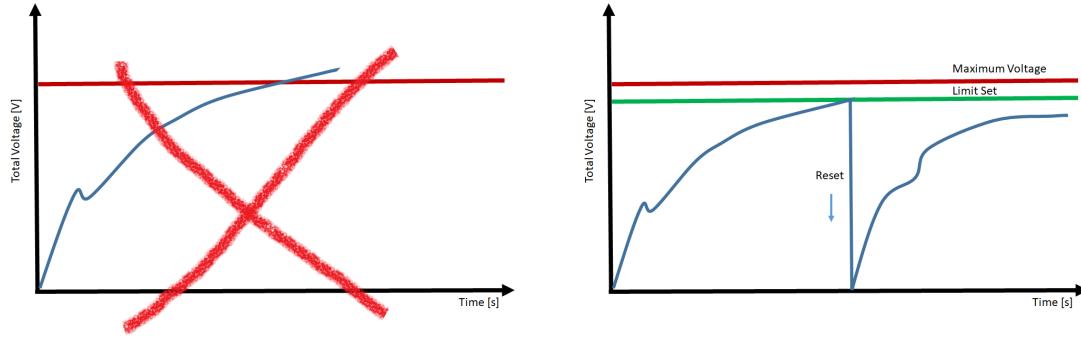


Figure 3.17. Principle of the “security check” on the maximum voltage applied to the mirror

During the development, it was suspected that the two main sources of voltage increase, which provided an almost linear component to the evolution of the total voltage applied to the actuators, were possibly referred to Tilt and Piston (sort of DC component of the commands). Indeed, the application of a huge tilt to the mirror implies the rotation of the plane of the wave-front created by the position of the actuators, consequently an increase in absolute value of the commands applied in the peripheral region of the mirror could be produced as shown in Figure 3.18. Also the increase of the Piston could cause an increase of the total amount of voltage applied on the mirror as it possible to deduce from Figure 3.19.

This two effects are detrimental for the behaviour of the deformable mirror because the increase of the total amount of voltage bring to the saturation of the physical limits of the device. As a consequence, countermeasures have to be taken. First of all, it is remarkable to mention that the library functions could be forced, thanks to two parameters *tilt_filtering* and *tilt_check*, to theoretically filter out and not apply any tilt to the mirror. The effectiveness of those functions will be discussed later in Section 4.1. Moreover, it was provided into the development of the software the possibility to remove the average of the commands and the possibility to further remove any possible tilt component before the actuation. The former procedure is simply accomplished evaluating at each iteration the average of the delta commands to apply and removing this average before the actuation from the whole vector containing the commands to apply. The latter, on the other hand, is more involving to be realized. Indeed, as a first step, it is required to reconstruct the matrix of the commands from the vector of commands, in order to see if a linear trend similar to the one presented in Figure 3.18 is present or not. This phase requires attention since the effective distribution of the actuators is similar to a square with smoothed angles. After having reconstructed this matrix, it is then easy to subtract the linear component and to use the new evaluated commands to feed the actuators.

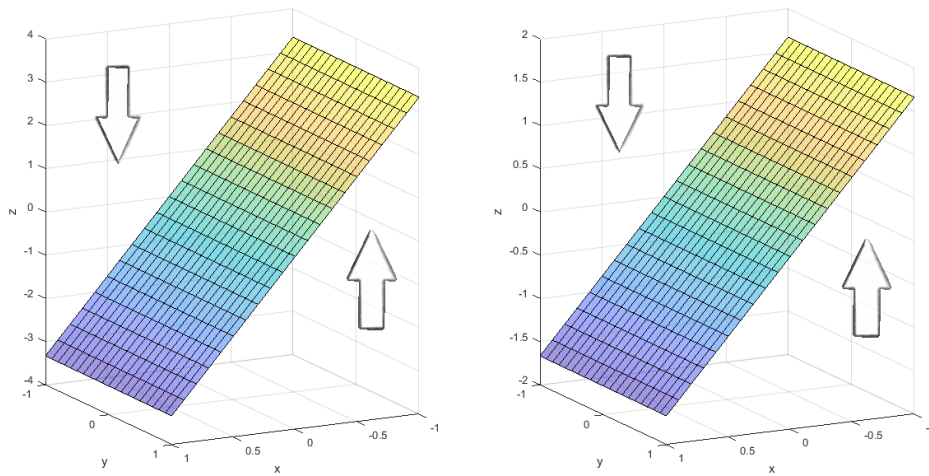


Figure 3.18. example of tilt difference: plane $70x + 21z = 0$ on the left and plane $35x + 21z = 0$ on the right

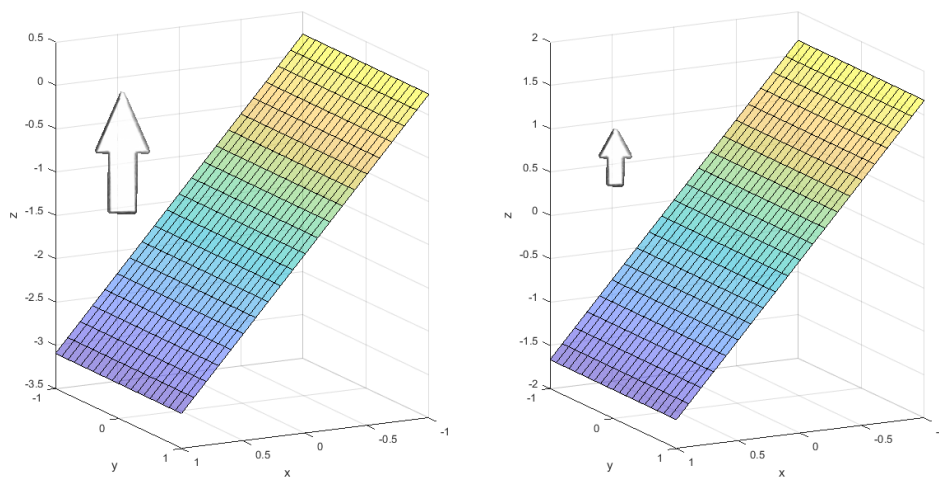


Figure 3.19. example of tilt difference: plane $35x + 21z + 30 = 0$ on the left and plane $35x + 21z = 0$ on the right

3.9 Loop GUI

To perform the in-vivo imaging it is required to have the possibility to stop the loop. This condition it is not available within a simple *Matlab*[®] script. For this reason the code as also been organized into a Graphical User Interface (GUI) version. Since, as previously mentioned, the *Matlab*[®] version used is *Matlab*[®] 2013a, the realization of the GUI was

done using *Matlab*[®] GUIDE. The variable that refers to possible choice for the user are then displayed on the interface and managed with “handles objects” to allow them to be seen from all the callback functions. The Interface is shown in Figure 3.20.

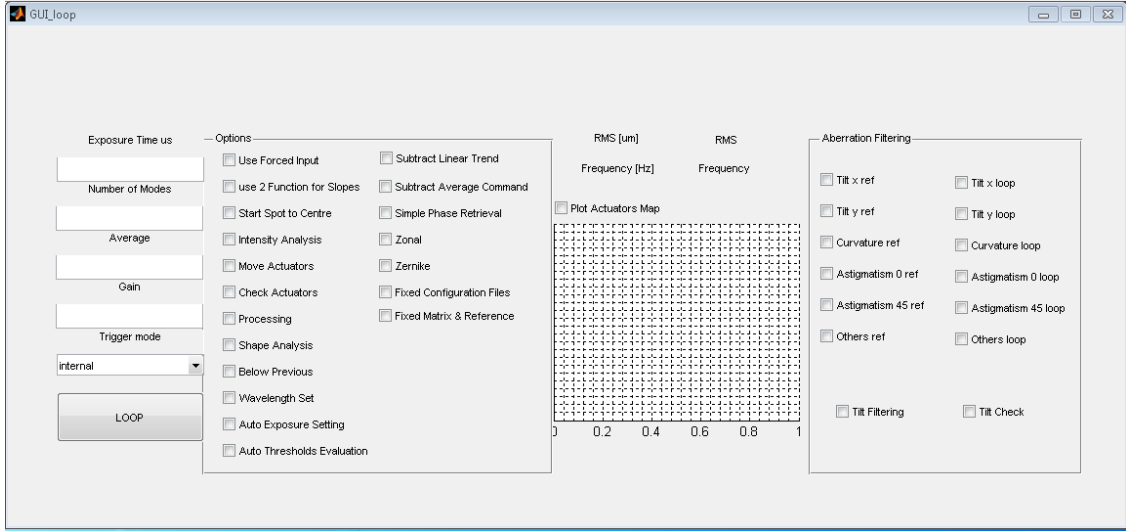


Figure 3.20. appearance of the interface to the user

On the left of the Interface, the first column of choices allows the user to insert the *exposure time*, the *number of modes* to use, the *number of images to average*, the *gain* and to select the *trigger mode* among *internal*, *external rising edge* and *external falling edge*. The bunch of check-boxes on the right of the first column allows to select which options will be used by the implemented software. *Move actuators* makes effective the actuation of the mirror, while *Check actuators* permits to limit the used dynamics of the actuators. *Simple phase retrieval*, *Zernike* and *Zonal* combination allows to defined the phase retrieval technique used. To chose *Zonal* procedure *Simple phase retrieval* and *Zonal* have to be checked; to use *Zernike* procedure *Simple phase retrieval* and *Zernike* have to be checked; to use the more complex procedure presented in Section 3.7 no one of them have to be checked. Then, *Auto exposure setting* and *Auto threshold evaluation* refer to the automatic setting of the exposure from the pixels’ saturation limits and to the procedure to evaluate the processing thresholds before the beginning of the loop respectively. Moreover, *Processing*, *Shape analysis* and *Below previous* have all to be checked if all the technique to recognise the blinking want to be used. Furthermore, *Subtract linear trend* and *Subtract average command* refers to the added option to remove *Tilt* and *Piston* respectively. On the right of the interface instead is then possible to see the map of actuators reconstructed and to set the aberration filtering configuration.

Chapter 4

Testing and Validation of the AO Loop

This Chapter will discuss the overall results obtained with the software described in Chapter 3. The attention will be focus on the main issues for the system, whose existence has been the root of many of the “security checks” implemented in the software. The main features that have to be tested to really validate the software are related to the ability of the loop to handle the pupil tracking task and the aberration correction task. Furthermore another issue will be treated relatively to the physical limits of the *deformable mirror* in terms of maximum total applied voltage. Indeed, the power related limitations that characterize the device imply it is not possible to apply more than 25 V on the mirror considering all the 52 actuators. This leads to the fact that if the required correction needs more voltage than this limit to be performed the system will not be able to apply it. In the previous scenario this condition forced also the stopping of the loop, with the provided code it will be able to maintain the loop working by resetting the actuators. During the testing it was noticed that this problem was mainly related to the tilt component of the commands. As a consequence the characteristics of this issue, the *tilt problem*, will be discussed in Section 4.1. Afterwards, the possibilities discussed in Section 4.1 will be validated in Section 4.2 thanks to the in-vivo imaging process. The second fundamental ability of the loop should then be the one to be able to follow the pupil movements and behaviour. This issue, defined as the *Pupil Tracking* problem is mainly related to the ability of the software to withstand when the patient is blinking. Therefore, the validation of the procedures previously presented in Section 3.5 will be tackled in Section 4.3. A complete analysis of the effectiveness of those procedure will also be provided in terms of *True Positives* and *False Positives*. Furthermore, to understand if the provided software is able to generate a good result in terms of aberration correction a comparison of its Resolution abilities with respect to the one of the previous used software will be provided in Section 4.4 thanks to the use of an USAF Target. Finally a brief analysis of the speed of the system will be developed in Section 4.5, pointing then out the main contribution during the loop iteration.

4.1 The Tilt Problem and the Voltage

For the reasons explained in Section 3.6 the first chosen configuration, taking into account the needs of the correction to provide, was to filter out the tilt components both on the reference wave-front's slopes and on the current loop wave-front's slopes. Moreover, it was also applied the *tilt_filtering* option provided by one of the library functions, thus theoretically eliminating any residual tilt component before the actuation. The function setting is shown below.

Listing 4.1. *tilt_filtering* function

```
Imop_CorrDataManager_SetCommandMatrixPrefs( tilt_filtering=TRUE, ... )
```

This configuration was tested and the results of this experiment are reported in Figure 4.1 and Figure 4.2. For those cases, the maximum allowed voltage threshold was set to 20 V to maintain a security margin with respect to real physical limit of the device. If the attention is focused on the results of the ex-vivo test of Figure 4.1, it is clearly possible to see that the total voltage applied to the actuators is rising during the prosecution of the correction. This effect leads the total amount of voltage close to the threshold that was set. If, instead, the results of the in-vivo testing are analysed, it is clearly possible to see, how the increase of voltage is overcoming the maximum threshold fixed, thus bringing the actuators to the forced reset implemented for those cases in order to maintain the system at work. These resets are visible in Figure 4.1, and corresponds to the points where the total amount of voltage suddenly drops to zero. The occurring of those conditions implied the need of finding a possible reason. As a consequence the nature of the actuators command evolution during the loop was then tested. In order to check the actuators behaviour, the commands' matrix have been reconstructed and then its evolution plotted.

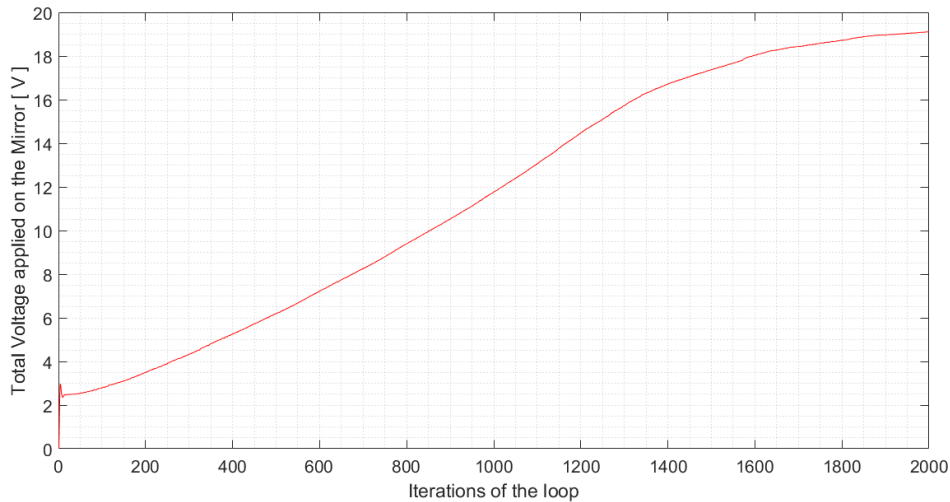


Figure 4.1. Evolution of the Total voltage applying *tilt_filtering* parameter, ex-vivo case (Exposure Time = 1.04 ms, 32 modes, gain = 0.5, Power SLD = 28 μ W)

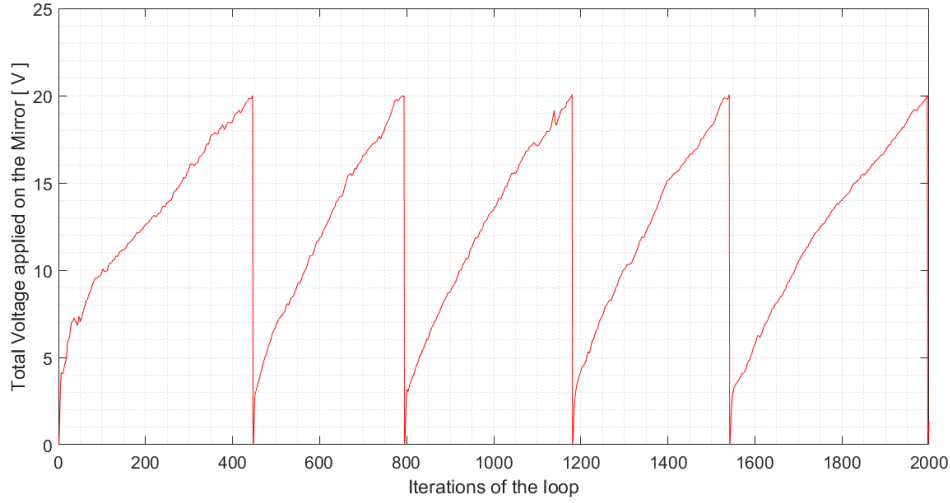


Figure 4.2. Evolution of the Total voltage applying *tilt_filtering* parameter, in-vivo case (Exposure Time = 5.32 ms, 32 modes, gain = 0.5, Power SLD = 28 μ W)

As a consequence of the analysis of the saved backup of the applied commands during the loop, it was possible from the reconstructed evolution of the commands' matrix, referring also to the effects described in Section 3.8, to see an increase of the linear component of the actuation correction. This effect is shown, for the previously mentioned configuration, in Figure 4.3 for the ex-vivo case and in Figure 4.4 for the in-vivo one.

Figure 4.3 and Figure 4.4 undoubtedly point out an increase of the tilt effect during the prosecution of the loop, effect that is remarkable both in the ex-vivo measurements and in the in-vivo experiments. As a consequence of those results obtained using the *tilt_filtering* parameter and filtering out the tilt component both on the reference wave-front's slopes and on the current loop wave-front's slopes, the tests were later repeated choosing a different configuration. Indeed, it was used also another parameter provided, the so called *tilt_check*, which as describe in the library should have prevented the application of huge tilts on the actuators [33]. The setting is shown below.

Listing 4.2. *tilt_check* function

```
[delta_commands, ...] = Imop_CorrDataManager_ComputeClosedLoopIteration ...
... ( slopes , tilt_check= TRUE, ... );
```

This new configuration works properly in the case of the ex-vivo measurement since the voltage is stabilized after a reduced number of iterations, as it is possible to see in Figure 4.5. Also in the case of the in-vivo experiment is present an improvement with respect to the previous configuration. This last behaviour is shown in Figure 4.6, where, although the voltage slightly increases it is still staying far from the maximum value allowed.

For a seek of precision, also in these two cases it was check the behaviour of the tilt component during the evolution of the loop. Again, from an analysis of the saved backup

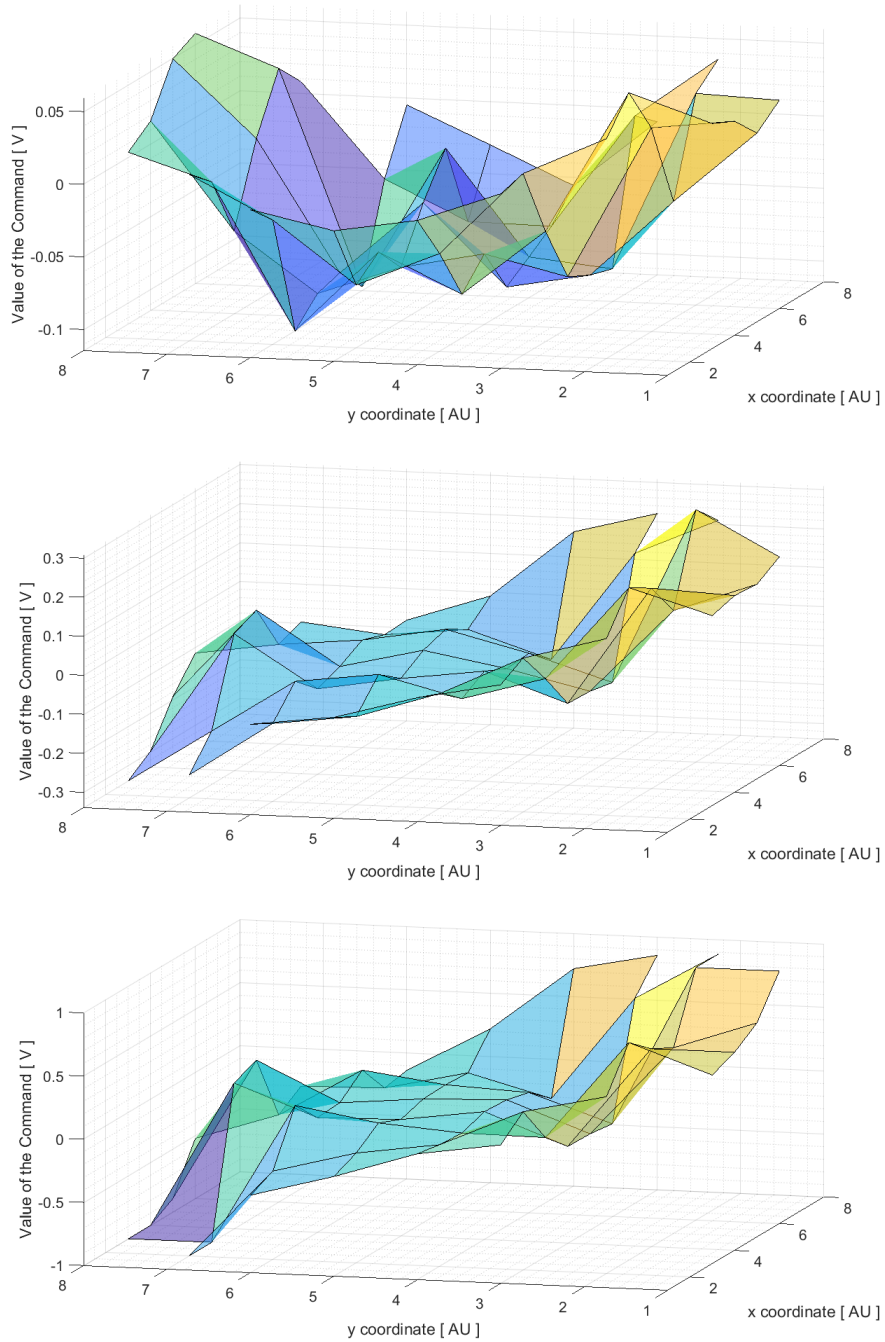


Figure 4.3. Evolution of the linear component on the applied commands using *tilt_filtering* parameter, ex-vivo case; images taken from the top for iteration number 10, 500, 1900 (Exposure Time = 1.04 ms, 32 modes, gain = 0.5, Power SLD = $28 \mu\text{W}$)

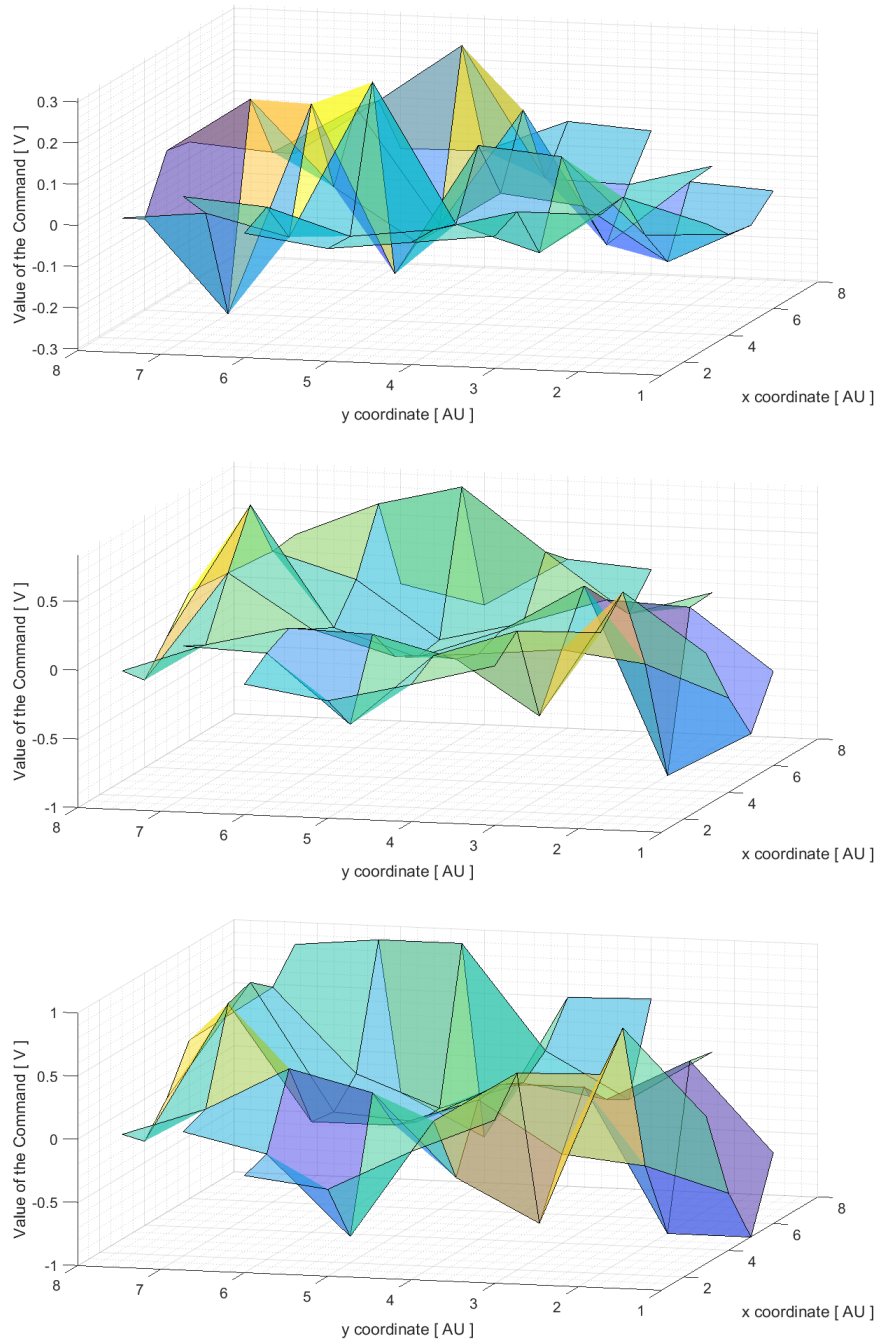


Figure 4.4. Evolution of the linear component on the applied commands using *tilt_filtering* parameter, ex-vivo case; images taken from the top for iteration number 10, 200, 440 (Exposure Time = 5.32 ms, 32 modes, gain = 0.5, Power SLD = 28 μ W)

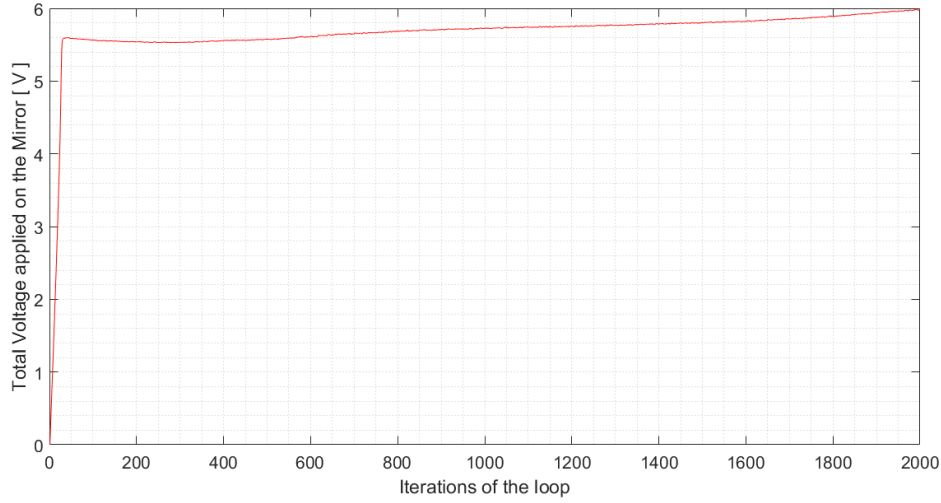


Figure 4.5. Evolution of the Total voltage applying *tilt_filtering* parameter and *tilt_check* parameter, ex-vivo case (Exposure Time = 1.09 ms, 32 modes, gain = 0.5, Power SLD = $28 \mu\text{W}$)

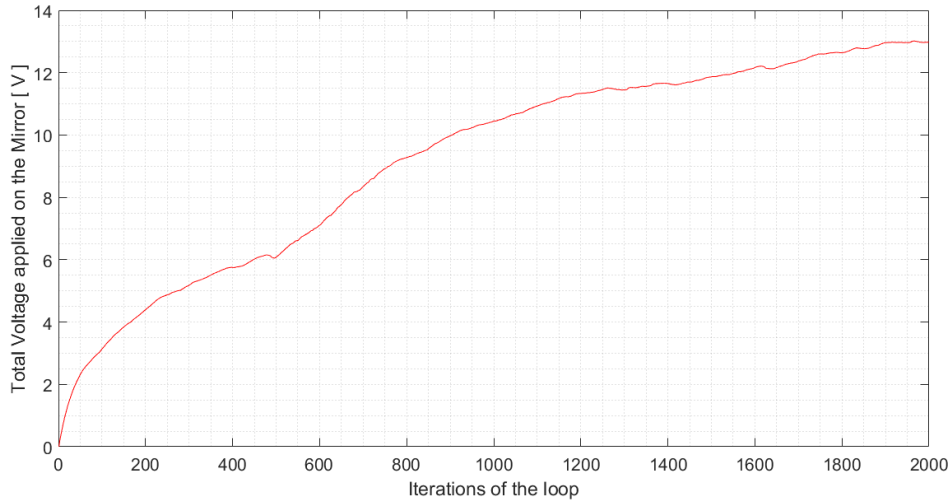


Figure 4.6. Evolution of the Total voltage applying *tilt_filtering* parameter and *tilt_check* parameter, in-vivo case (Exposure Time = 5.12 ms, 32 modes, gain = 0.5, Power SLD = $28 \mu\text{W}$)

of the applied commands, it is possible, referring to the effect described in Section 3.8, to see almost no linear component in the case of the ex-vivo experiment, as shown in Figure 4.7. Moreover, a very small effect, if compared to the previous configuration, it was evident in the in-vivo case, as shown in Figure 4.8.

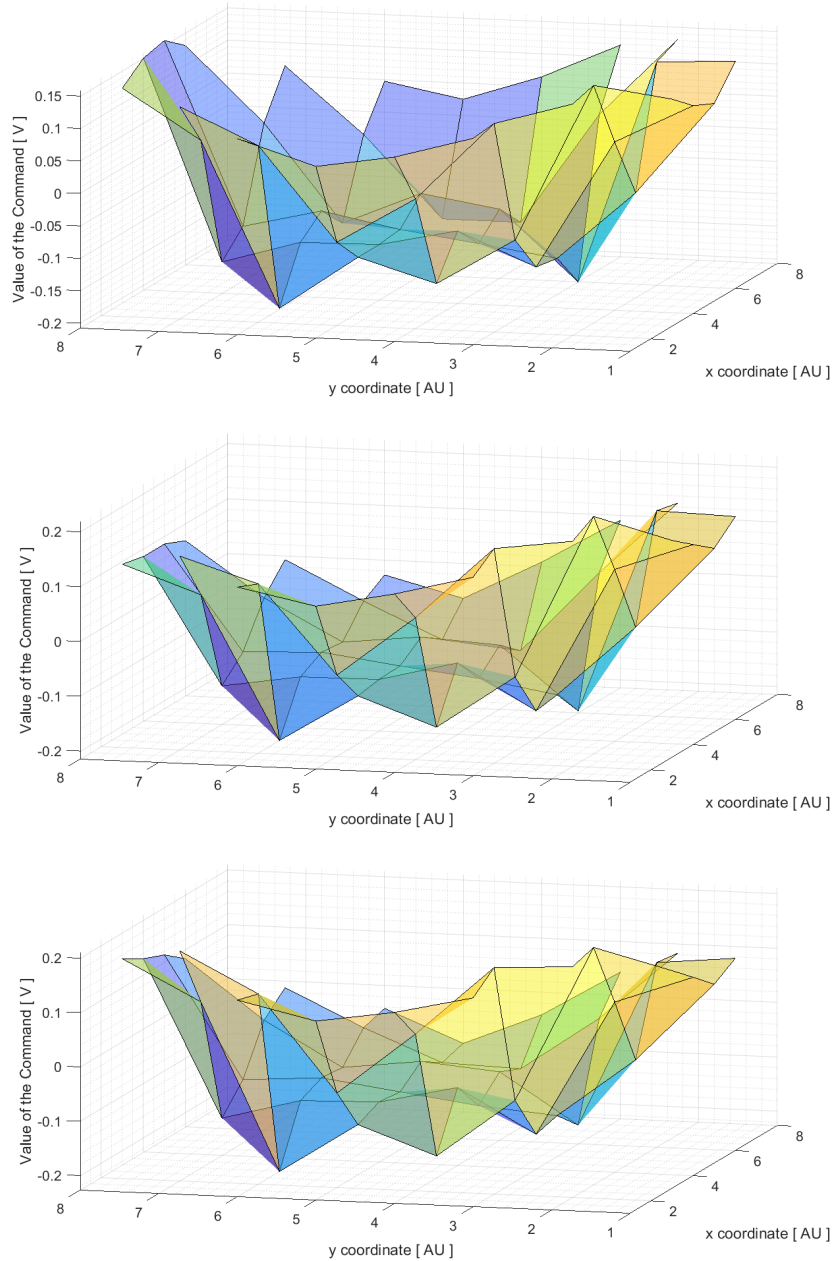


Figure 4.7. Evolution of the linear component on the applied commands using *tilt_filtering* parameter and *tilt_check* parameter, ex-vivo case; images taken from the top for iteration number 100, 1000, 1900 (Exposure Time = 1.09 ms, 32 modes, gain = 0.5, Power SLD = 28 μ W)

The use of *tilt_check* parameter effectively removes almost the whole tilt component of the commands before the actuation. Although this, in one of the in-vivo tests that followed

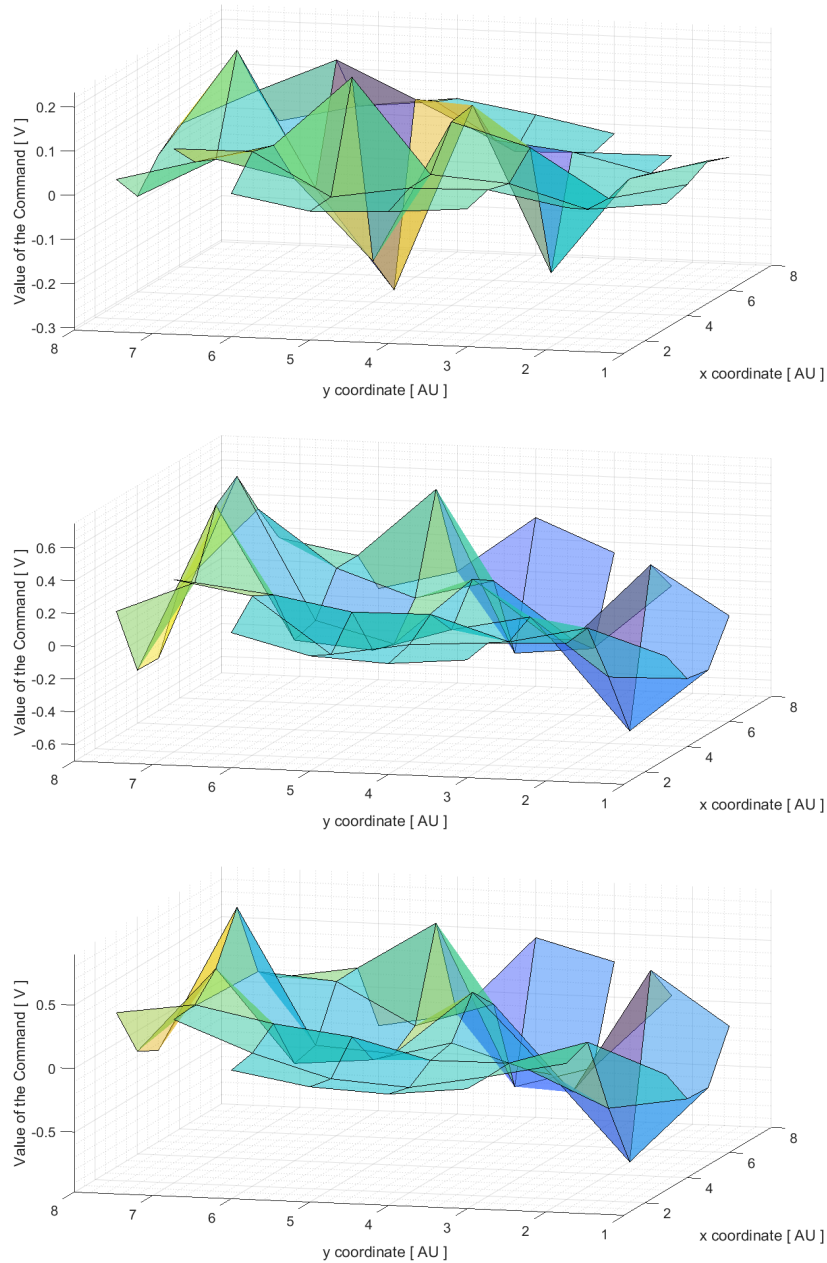


Figure 4.8. Evolution of the linear component on the applied commands using *tilt_filtering* parameter and *tilt_check* parameter, in-vivo case; images taken from the top for iteration number 100, 1000, 1900 (Exposure Time = 5.12 ms, 32 modes, gain = 0.5, Power SLD = 28 μ W)

it was suspected a possible limitation. It resulted that the usage of *tilt_check* parameter, slows slightly down the recovery from the blinking condition, thus possibly influencing the

image acquisition. This effect could be seen in Figure 4.9 close to iteration 120.

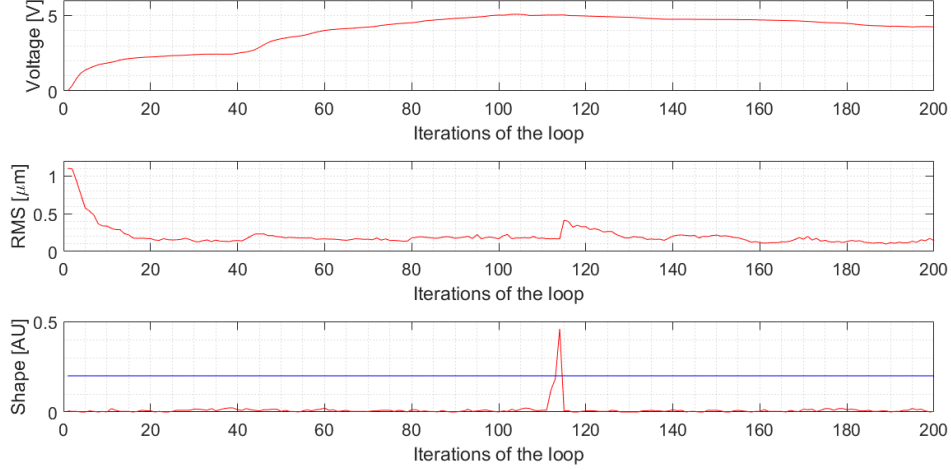


Figure 4.9. Evolution of the Total voltage applying *tilt_filtering* parameter and *tilt_check* parameter, evolution of the RMS residual phase error and evolution of the shape parameter, in-vivo case (Exposure Time = 6.44 ms, 32 modes, gain = 0.5, Power SLD = 28 μ W)

Hence, subsequently to these results, it was investigated the possibility to avoid the *tilt_check* parameter and to forcefully remove the remaining tilt component before the actuation. To perform this operation it was used the method presented in Section 3.8. To test its effect the parameters *tilt_filtering* and *tilt_check* were not used in this case. The results of the usage of this configuration are visible in Figure 4.10 concerning the total voltage applied and the RMS residual phase error. Meanwhile, Figure 4.12 shows the evolution of the linear component, which is almost removed; indeed, it is not possible to see evident differences during the increment of loop iterations. Lastly, the same configuration has been tested in-vivo. In Figure 4.11 it is shown the behaviour of the total applied voltage while in Figure 4.13 the behaviour of the linear component.

Finally, it is possible to conclude that both the *tilt_check* parameter and the method introduced in the last presented configuration allow to obtain as a result, with two different effectiveness, an almost total removal of the tilt before of the mirror actuation. The removal seems to be more efficient in the case of the *tilt_check* parameter, but as said there is the possibility that it slightly slows down the recovery from blinking conditions.

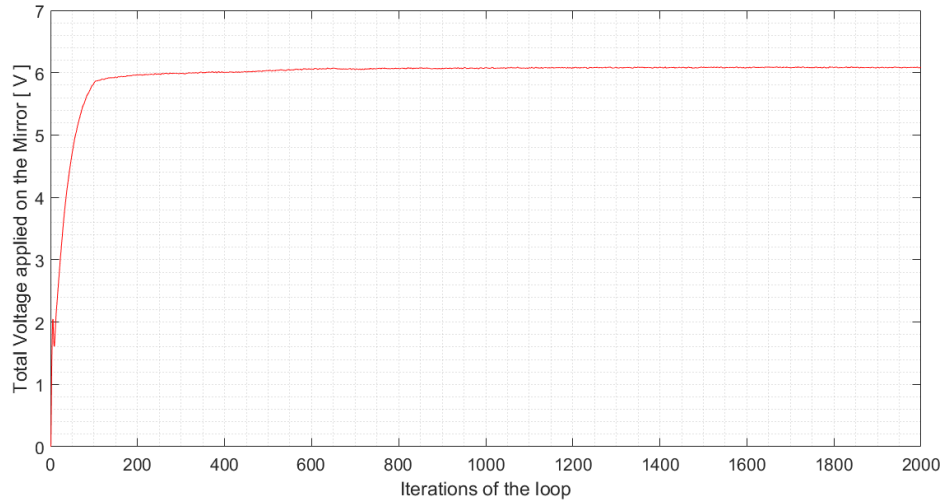


Figure 4.10. Evolution of the Total voltage applying forcefully removal of tilt component, ex-vivo case (Exposure Time = 1.39 ms, 32 modes, gain = 0.5, Power SLD = $28 \mu\text{W}$)

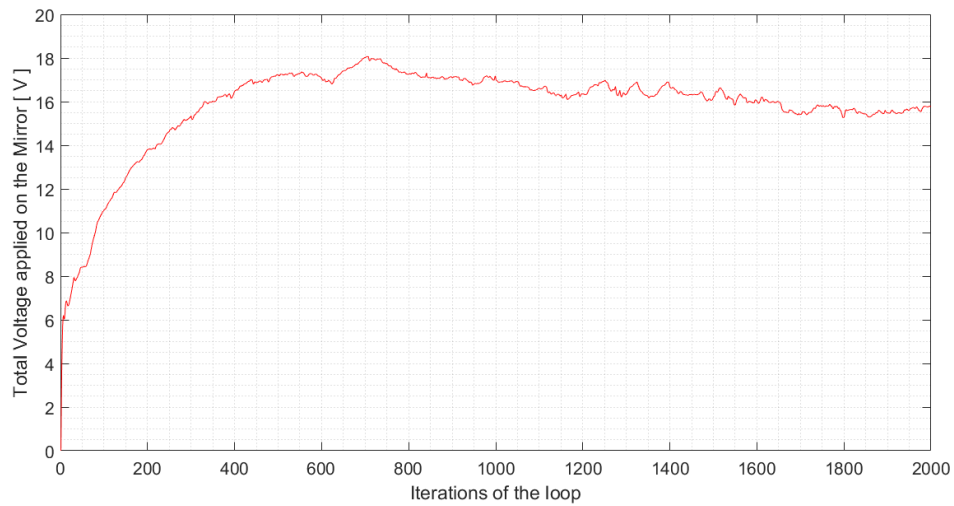


Figure 4.11. Evolution of the Total voltage applying forcefully removal of tilt component, ex-vivo case (Exposure Time = 6.04 ms, 32 modes, gain = 0.5, Power SLD = $28 \mu\text{W}$)

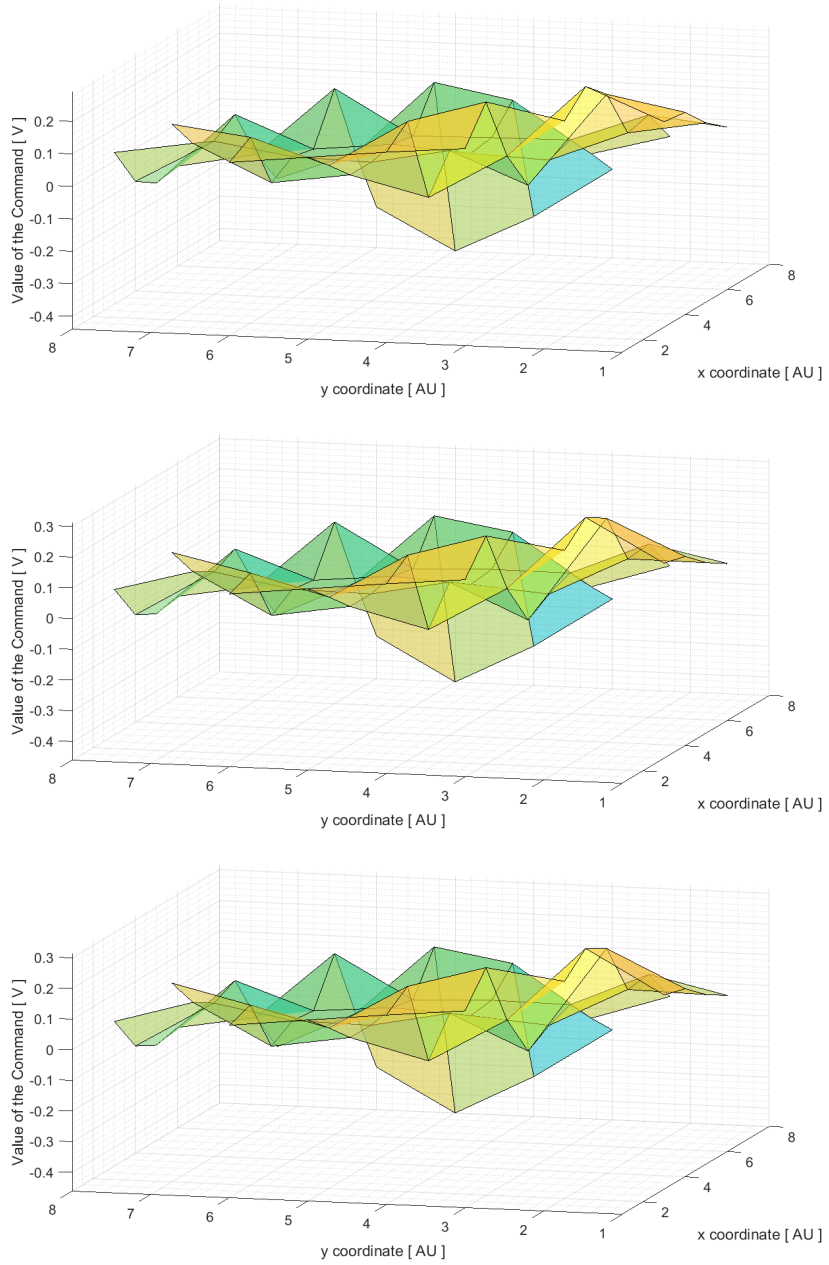


Figure 4.12. Evolution of the linear component on the applied commands applying forcefully removal of tilt component, ex-vivo case; images taken from the top for iteration number 100, 1000, 1900 (Exposure Time = 1.39 ms, 32 modes, gain = 0.5, Power SLD = 28 μ W)

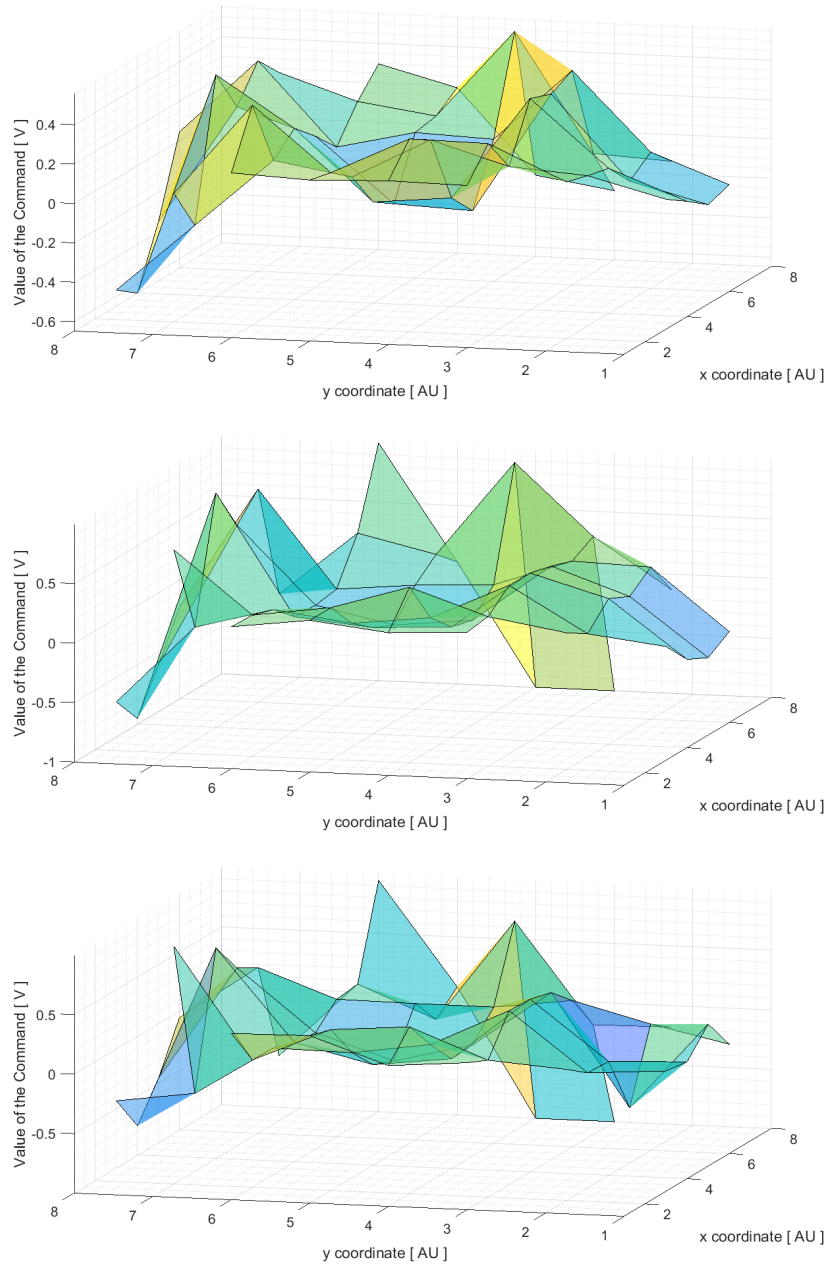


Figure 4.13. Evolution of the linear component on the applied commands applying forcefully removal of tilt component, in-vivo case; images taken from the top for iteration number 100, 1000, 1900 (Exposure Time = 6.04 ms, 32 modes, gain = 0.5, Power SLD = 28 μ W)

4.2 In-vivo Imaging Results

To further check the behaviour of the two configurations presented in Section 4.1, live-imaging experiments were performed. After the acquisition of 300 images for each of the two configurations, the resulting stack of images was post-processed. The first task to be performed is the alignment of the images in order to completely remove the shift introduced by the movement of the eye. Moreover, this task is followed by the normalization of the contrast. Indeed, after the alignment procedure has been performed, the boundaries regions of the images are not providing any more information, and being “black regions” they force unnaturally the contrast. Finally, the resulting images were analysed in the frequency domain. To do so, a Fast Fourier Transform was performed. In the spectral domain is then possible to recognise, in proximity to the centre, a glimpsing annular structure, which corresponds to the spatial frequency relative to the RPE cells imaged in the experiments. The analysis of the images obtained demonstrated in the first place that the loop software is properly performing the correction of the aberrations, since in both cases it was possible to glimpse the features of the imaged retina section. Concerning the analysis of the configuration instead, it was noticed that, between the two presented in Section 4.1, the use of *tilt_check* provided a better result. Indeed, not only the cells are clearly visible, but also the RPE spatial frequency is more evident in the Fourier domain. As a consequence, it could be supposed that the effect seen in Figure 4.9 is not only related to the use of the *tilt_check* parameter but also dependent on the patient and on the external conditions. In conclusion, to perform a 100% certain choice between the two possible configurations, a large scale investigation on different patients should be required. The results of the comparison in terms of live-imaging of the retina, the comparison in the Fourier domain and the comparison of the axial behaviour of the integrated intensity on the Fourier domain are shown respectively in Figure 4.14, in Figure 4.15 and in Figure 4.16.

Moreover, to compare the quality of the imaging accomplished with the developed loop software, the obtained results in the best of the two configuration, the one that uses the *tilt_check* parameter, has been compared with what is obtained using the proprietary software loop. The results of the comparison in terms of live-imaging of the retina, the comparison in the Fourier domain and the comparison of the axial behaviour of the integrated intensity on the Fourier domain are shown respectively in Figure 4.17, in Figure 4.18 and in Figure 4.19.

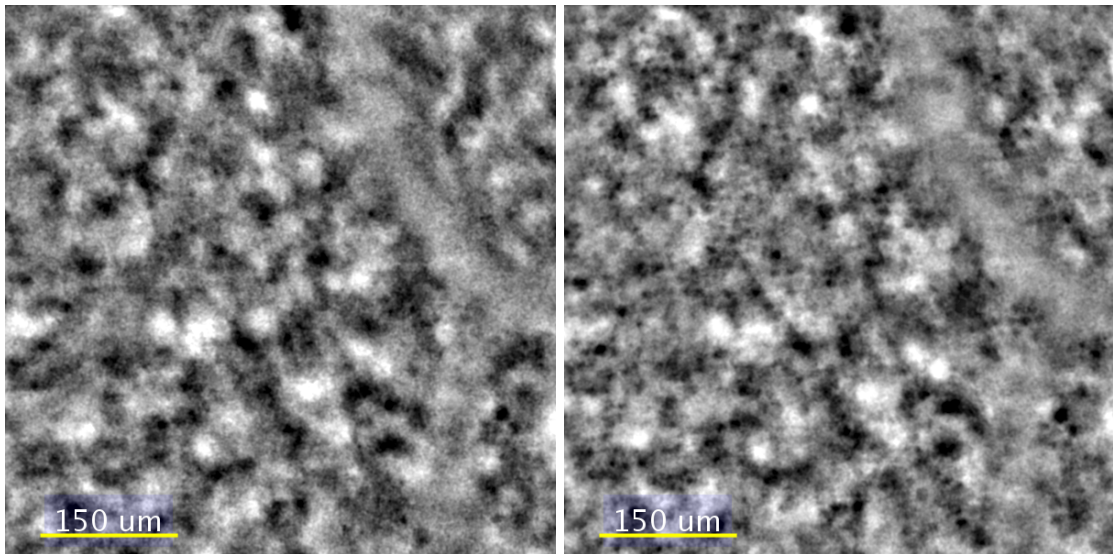


Figure 4.14. Acquired image of the retina: on the left column the one relative to the forcefully removal of tilt configuration, on the right one the image produced using the *tilt_check* configuration. See also Figures C.1 and C.2 of Appendix C

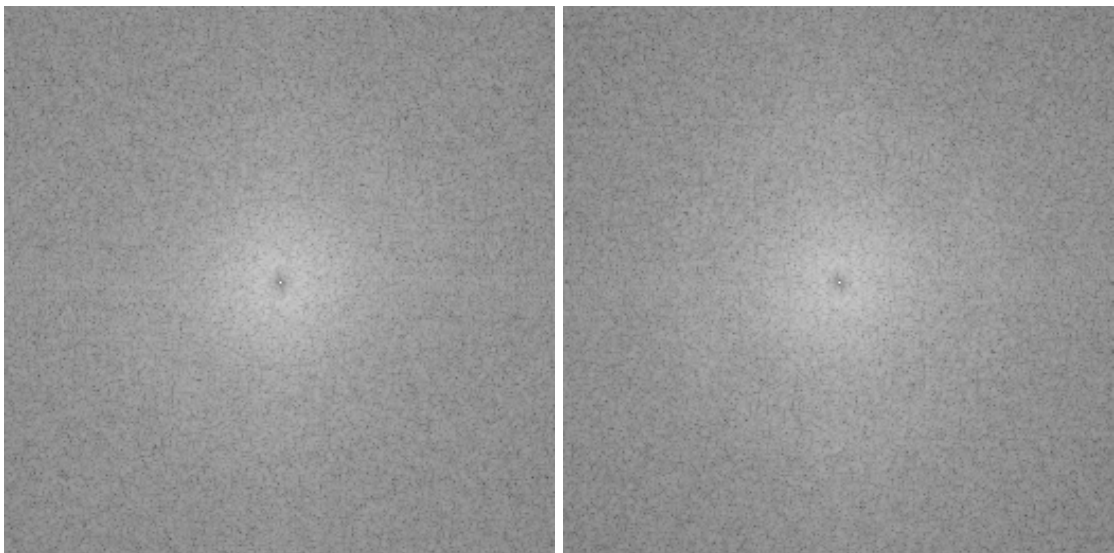


Figure 4.15. Fourier domain zoom: on the left column the one relative to the forcefully removal of tilt configuration, on the right one the image produced using the *tilt_check* configuration.

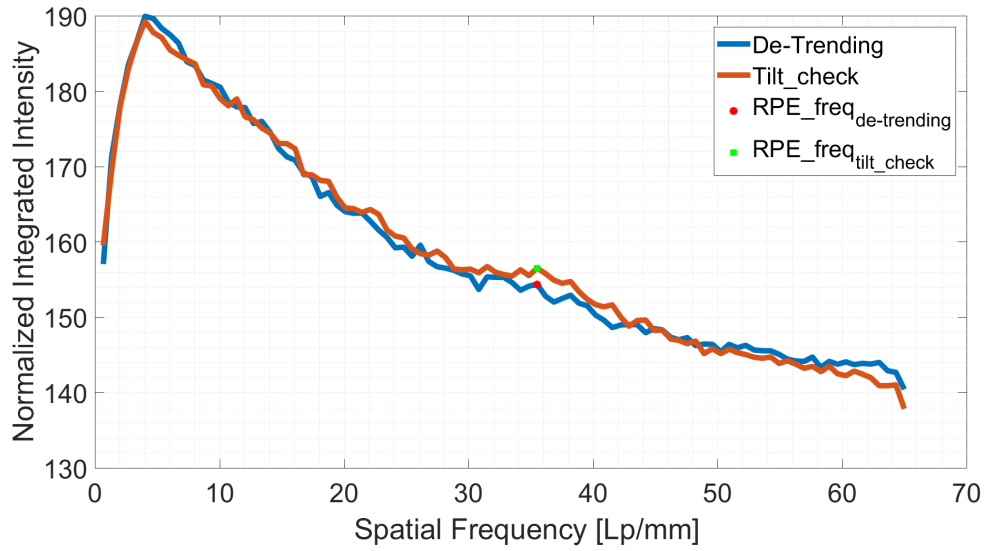


Figure 4.16. Comparison in terms of axial behaviour of integrated intensity in Fourier domain.

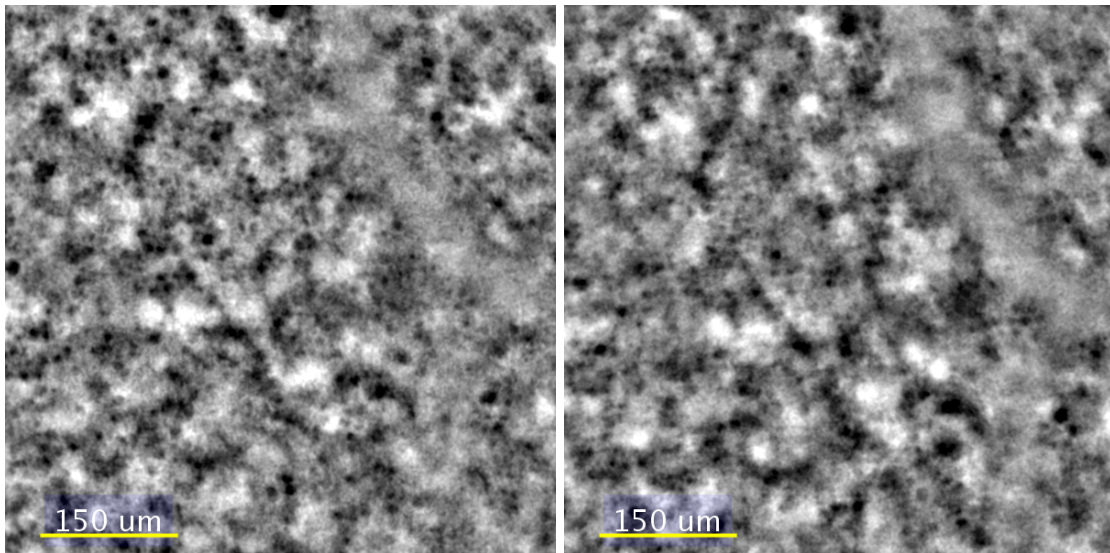


Figure 4.17. Acquired image of the retina: on the left column using the proprietary software, on the right one the image produced using the using the developed loop. See also Figure C.3 of Appendix C

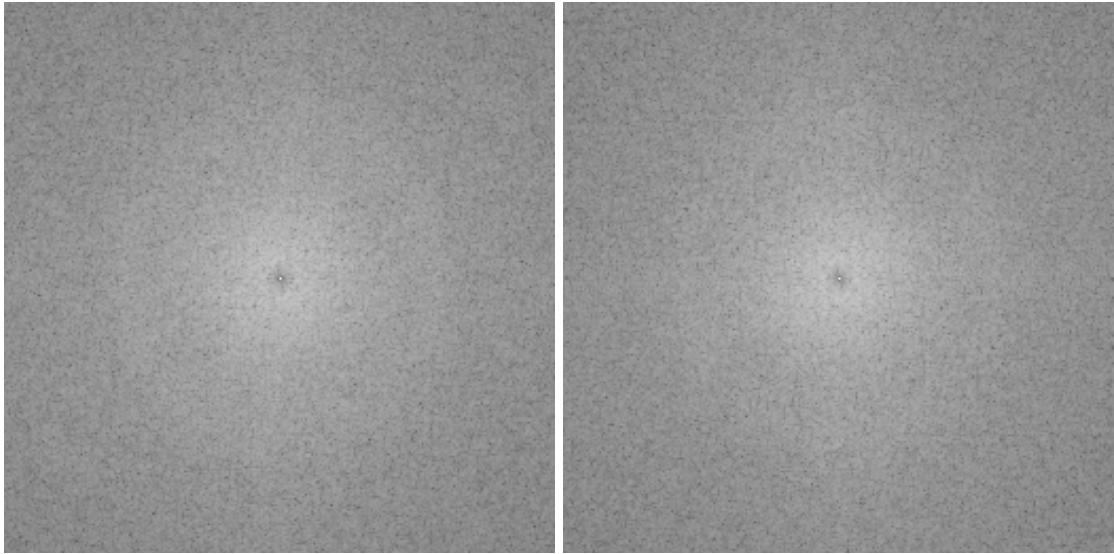


Figure 4.18. Fourier domain zoom: on the left column using the proprietary software, on the right one the image produced using the using the developed loop.

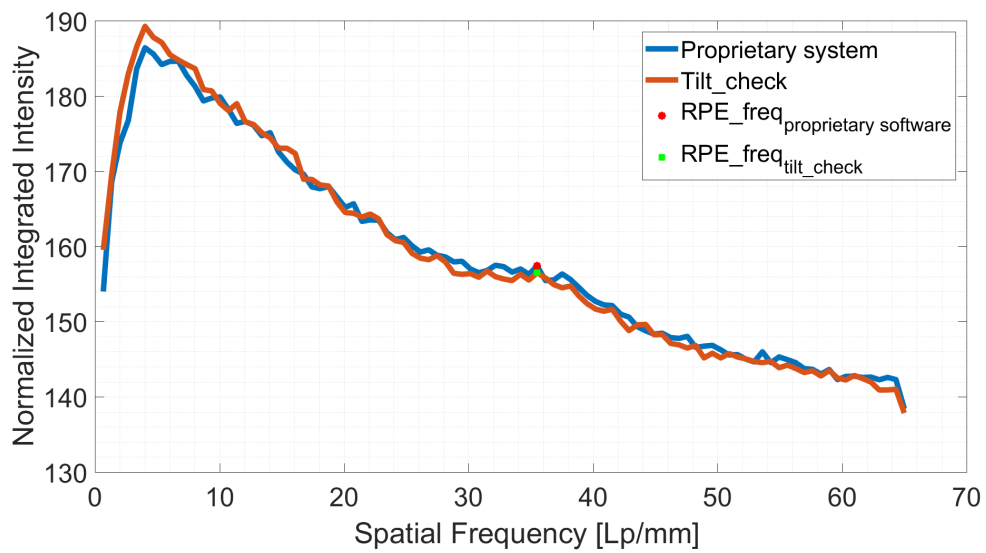


Figure 4.19. Comparison in terms of axial behaviour of integrated intensity in Fourier domain.

4.3 Withstanding the Blinking

An essential test that was performed is relative to the check of the ability of the produced loop software to effectively withstand the blinking condition. To be sure of this capability the test condition were stressed forcing many blinks to occur in a reduced time interval. From a first measurement done in these conditions it resulted that the loop withstood without providing errors or crashing. The results of this first measurement are shown in Figure 4.20 and Figure 4.21. The former shows the behaviour of the residual phase RMS error, which peaks in correspondence of a blinking event. This effect is due to the fact that, when the current image is supposed not to be suitable for the correction because it is not respecting the conditions described in Section 3.5, the previous good image that is respecting those conditions is maintained as the current image. the consequence of this choice is that, although the system is maintained at work, the nature of the generated correction is not perfect, because it is not completely respecting the position of the eye. When finally the images acquired by the wave-front sensor’s camera start again to be “good” the correction is performed properly, but the error to correct has increased due to the higher distance with respect to the previous applied correction, which was only used to maintain the system at work during the blinking. Instead, the latter shows the behaviour of the different figures of merit, which in accordance are eventually peaking the iteration before with respect to the residual phase error (cause effect behaviour).

To further check if each of the figures of merit variations corresponded to a blinking event, the test was repeated, this time recording a video of the eye behaviour with the pupil camera. After that the data were post processed to correlate the two available information. First of all the time evolution of the loop was reconstructed from the storage of the time needed to perform each iteration. In this way, supposing to start a chronometer at the beginning of the loop, it was derived the value of that timer at each iteration. This was done accordingly to equation 4.1.

$$timer_{iteration_}(i),loop = \sum_{j=0}^{j=i-1} iteration_duration_j \quad (4.1)$$

Then a similar procedure was followed for the pupil camera video. Knowing the *frame rate* of the camera during the video, which resulted to be equal to 25.13 *frame/s*, also in this case it was reconstructed the *time axis*. This time, considering that the camera could have been started not exactly at the same time of the loop. Thus, an unknown offset contribution was added accordingly to equation 4.2

$$timer_{iteration_}(i),camera = offset + timer_{iteration_}(i-1),camera + 1/frame\ rate \quad (4.2)$$

After that, from the data of Figure 4.22 it was determined for which iterations it was supposed to be present a blink as the cause of the behaviour of the figures of merit. From this analysis eighteen different blinking episodes were supposed. Presuming then the offset

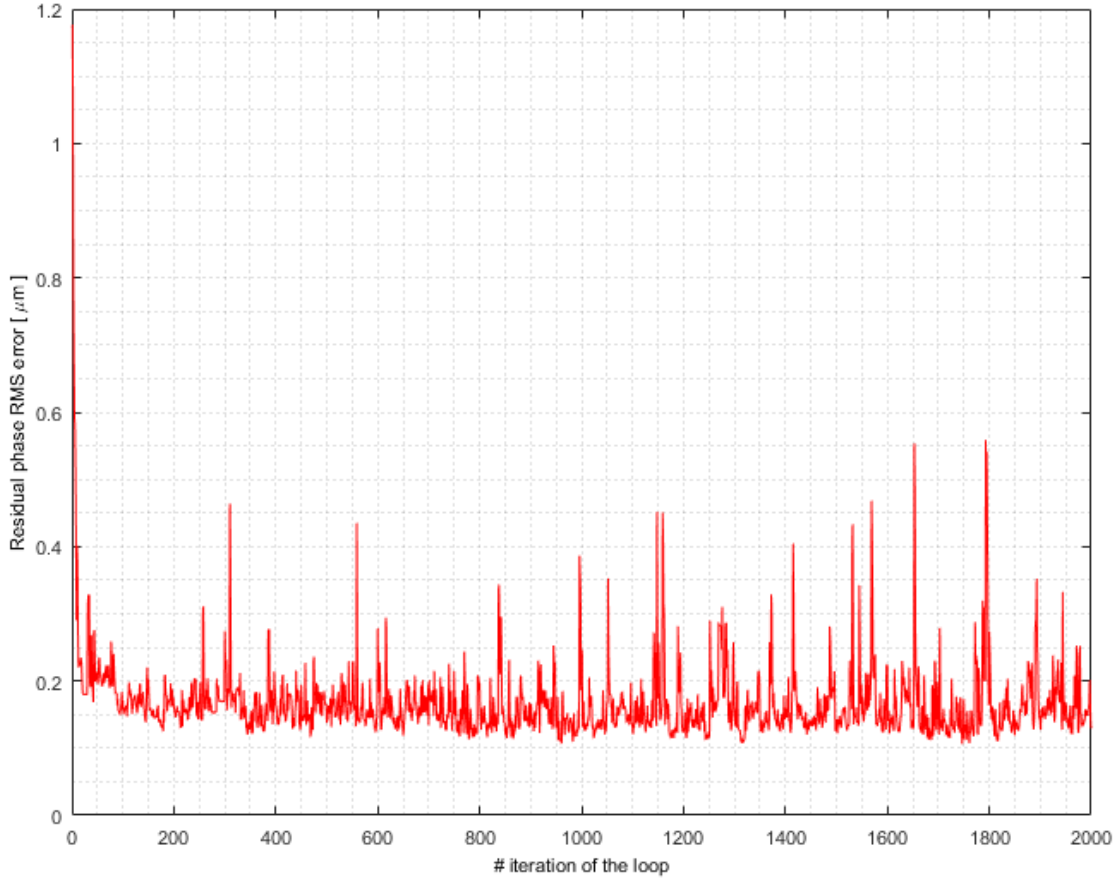


Figure 4.20. In-vivo test of the ability of the loop to withstand the blinking: residual phase RMS error (Exposure Time = 6.04 ms, 32 modes, gain = 0.5, Power SLD = 28 μW)

to be equal to zero, that means that camera and loop are supposed to be started at the same time instant, it was calculated for each supposed blinking episode the frames at which it should have been visible in the camera video. This operation was handled finding the first video frame timer value that was not any more smaller than the value found as timer reference for the blinking episode on the loop time axis. The related index of the containing vector at which that time value could be found corresponded to the supposed frame or range of frame to be checked. Afterwards, the camera video frames were checked till the first blinking episode. Consequently, a shift of 14 frames was founded. This because the camera started to record the video at a time corresponding to $14[\text{frame}] \cdot \frac{1}{25.23}[\frac{s}{\text{frame}}] = 0.557[\text{s}]$ before the real starting of the loop of correction. Removing this offset, the supposed frames interested by blinking episodes were analytically evaluated again to have a starting interval of frames to check on the video. After checking each of those intervals, which almost perfectly matched the real ones, a 100% correspondence was found in terms of blinking events. Hence, it was demonstrated that the system perceived all the blinking

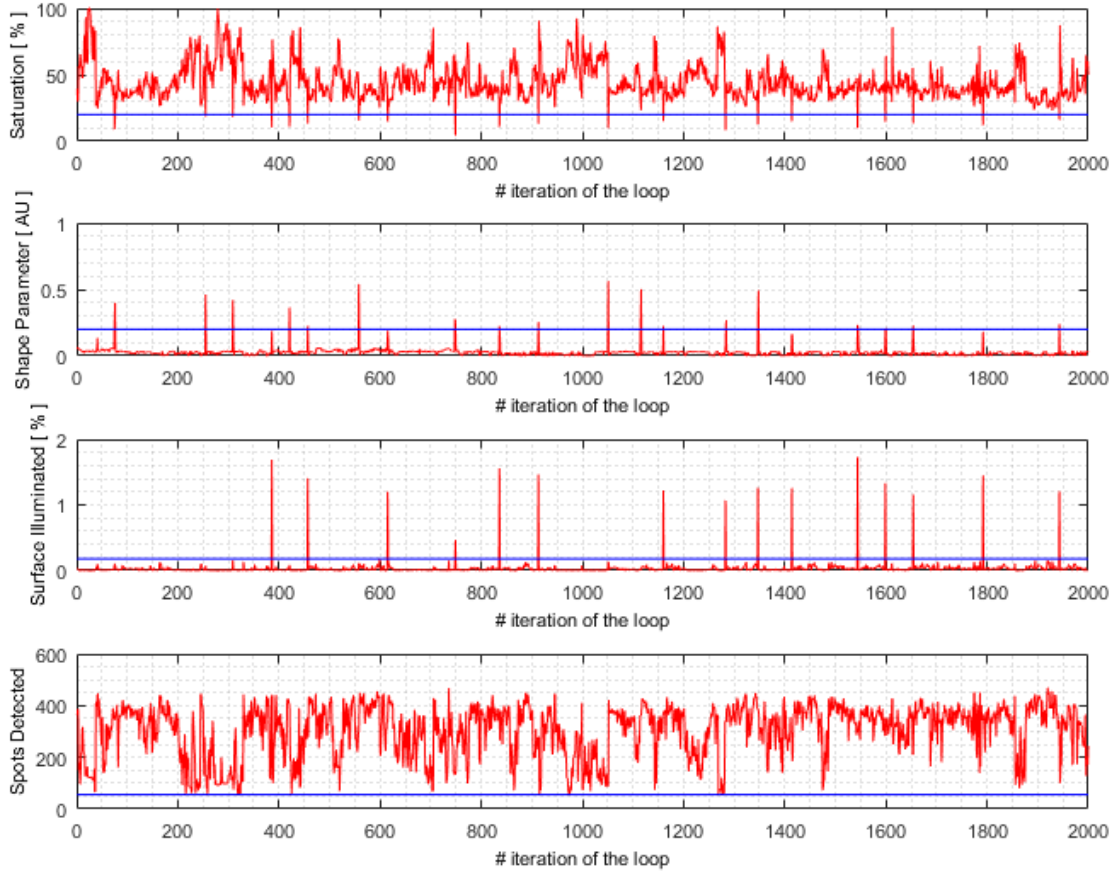


Figure 4.21. In-vivo test of the ability of the loop to withstand the blinking: variation of the different figures of merit during the loop, in red the variations, in blue the thresholds set. From the top to the bottom: Saturation, Shape Parameter, Surface Parameter, Spots Detected (Exposure Time = 6.04 ms, 32 modes, gain = 0.5, Power SLD = 28 μ W)

episodes and that no *False Positives* had occurred. Therefore, it is possible to affirm that the chosen figures of merit are able to efficiently detect the presence of a blinking event. The values obtained during the processing are reported in Table 4.1. The real frames corresponding for instance to the first blinking event are reported in Figure 4.23.

The importance of these results is also corroborated from another test. It was indeed, checked if the system was able to withstand the blinking of the patient without performing any check on the values of the previously described figures of merit. In this case the system crashed as expected providing a “no signal” error, moreover, the configuration of the spots’ matrix on the CCD at the moment of failure was checked, and it obviously corresponded to one of those clearly produced by a blinking. The results of this test are reported in Figure 4.24, while in Figure 4.25 it is shown the spots’ matrix at the moment of the failure.

In conclusion it is possible to affirm that the implemented method provide an effective

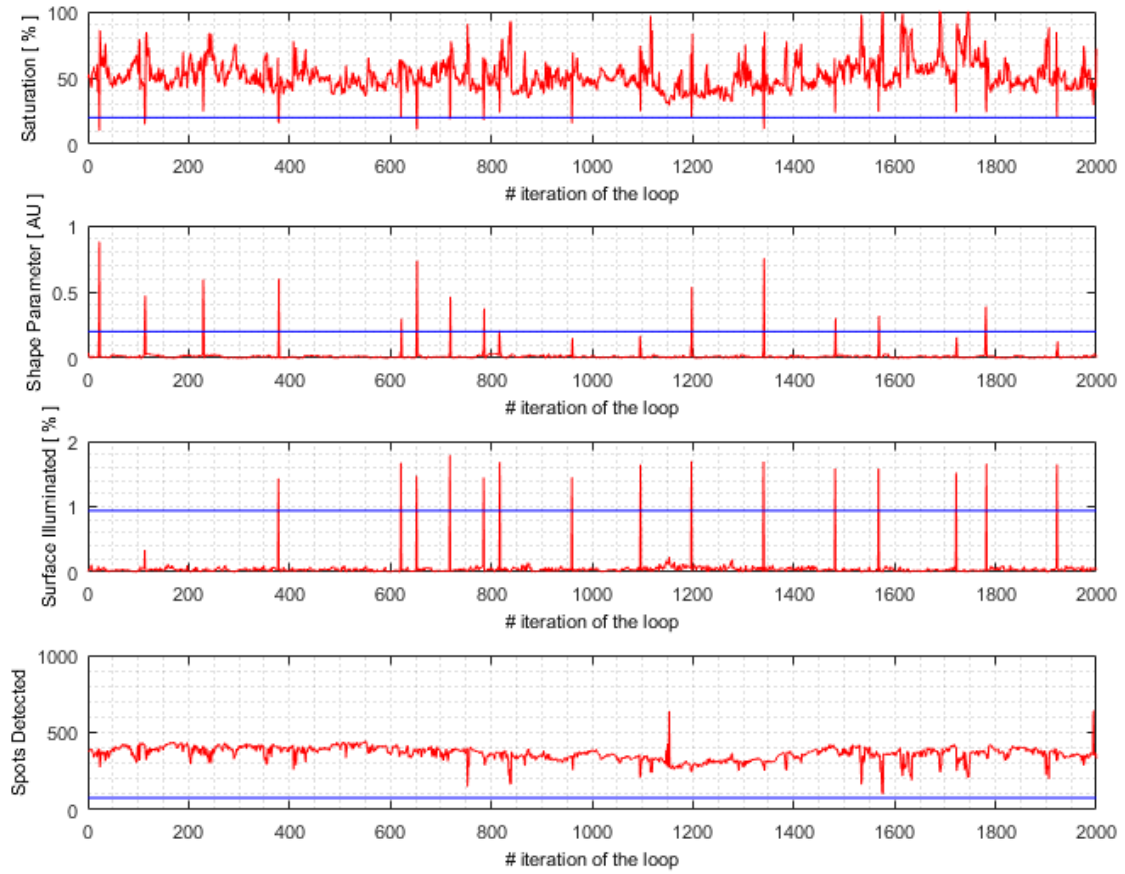


Figure 4.22. In-vivo test of the ability of the loop to withstand the blinking, variations of the different figures of merit during the loop, in red the variations, in blue the thresholds set. From the top to the bottom: Saturation, Shape Parameter, Surface Parameter, Spots Detected (Exposure Time = 11.74 ms, 32 modes, gain = 0.5, Power SLD = 28 μ W)

security check for what concerns the problematic behaviour of blinking, without implying the detrimental drawback of *False Positive* episodes.

Results Blinking Verification						
Episode	Iterations	$Frames_{no\ offset}$	$Frame_{real}$	Offset	$Frames_{offset}$	Ok?
1	22-23	44-49	58-64	14	58-63	✓
2	113-114	149-154	163-168	14	163-168	✓
3	229-230	281-286	297-302	16	295-300	✓
4	378-379	449-453	463-468	13	463-467	✓
5	621-622	716-721	730-734	14	730-735	✓
6	652-653	756-760	770-775	14	770-774	✓
7	718-719	833-838	847-853	14	847-852	✓
8	785-786	920-925	934-940	14	934-939	✓
9	816-817	959-964	975-981	16	973-978	✓
10	960	1128	1142-1145	14	1142	✓
11	1096	1277	1291-1296	14	1291	✓
12	1197-1198	1391-1396	1405-1412	14	1405-1410	✓
13	1340-1341	1554-1559	1567-1575	13	1568-1573	✓
14	1482-1483	1716-1721	1730-1735	14	1730-1735	✓
15	1568-1569	1818-1823	1832-1838	14	1832-1837	✓
16	1722	1991	2005-2010	14	2005	✓
17	1780-1782	2060-2069	2075-2086	15	2074-2083	✓
18	1922	2225	2239-2245	14	2239	✓

Table 4.1. Results of Blinking verification

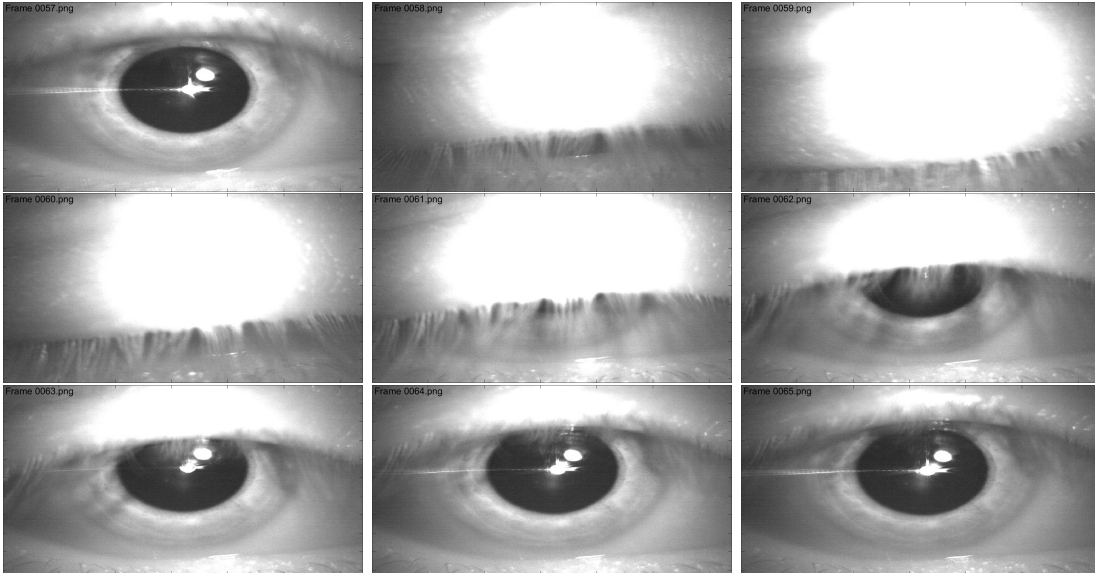


Figure 4.23. Pupil camera's frames for the first blinking episode of table 4.1

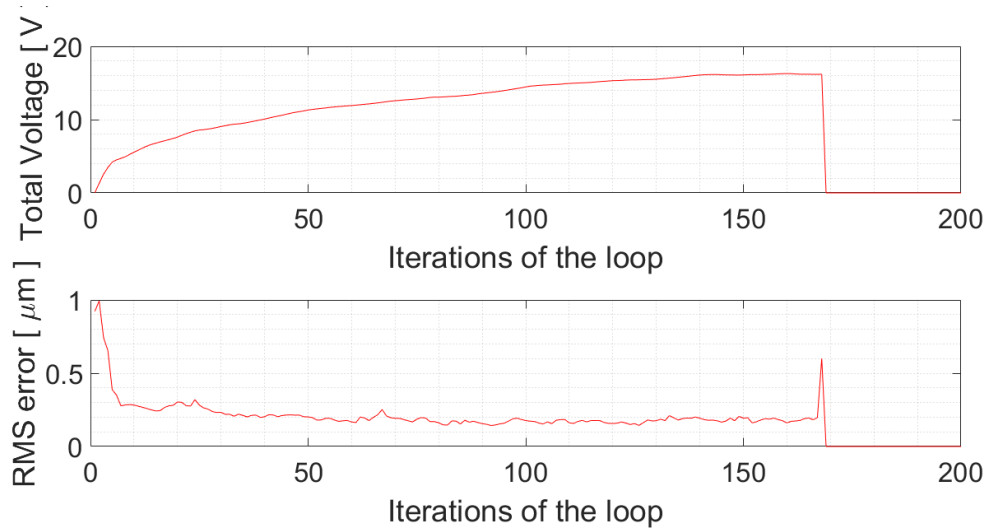


Figure 4.24. In-vivo test of the ability of the loop to withstand the blinking without any check on the values of the figures of merit, total amount of applied voltage and residual phase RMS error (Exposure Time = 9.62 ms, 32 modes, gain = 0.5, Power SLD = $28 \mu\text{W}$)

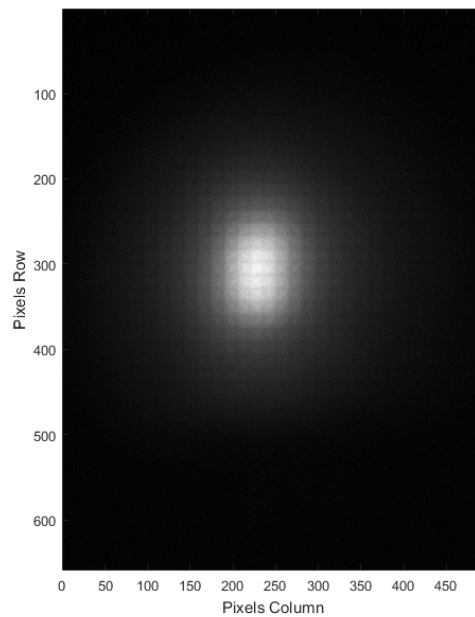


Figure 4.25. In-vivo test of the ability of the loop to withstand the blinking without any check on the values of the figures of merit, spots' matrix appearance at the instant of failure (Exposure Time = 9.62 ms, 32 modes, gain = 0.5, Power SLD = $28 \mu\text{W}$)

4.4 Testing the Optical Resolution

In order to compare the ability of the system to perform the correction with the same capability of the proprietary software, it was decided to evaluate the behaviour of the *Modulation Transfer Function* (MTF). To perform this measurement, images of a standard USAF Target were acquired both with the proprietary software and with the implemented Adaptive Optics Loop software. The comparison was performed evaluating the contrast using the horizontal targets of the elements of group 4, 5 and 6 of the USAF Target. To perform the measurement it was used a “10x objective” (Olympus, NA = 0.25, 10x). The acquired images are visible in Figure 4.26, where are also shown the region used to compute the contrast. Indeed, the contrast was evaluated along all the possible vertical lines belonging to the underlined squared region present in Figure 4.26 for all the elements. Thus, it was obtained an averaged value for the contrast and a standard deviation. Hereafter, each contrast value was related to the correspondent elements spatial frequency and the MTF behaviour was reconstructed. The behaviour of the two MTF are visible separately in Figure 4.27 and compared in Figure 4.28. In conclusion it is possible to affirm that the behaviour of the two system is comparable although not perfectly superimposed.

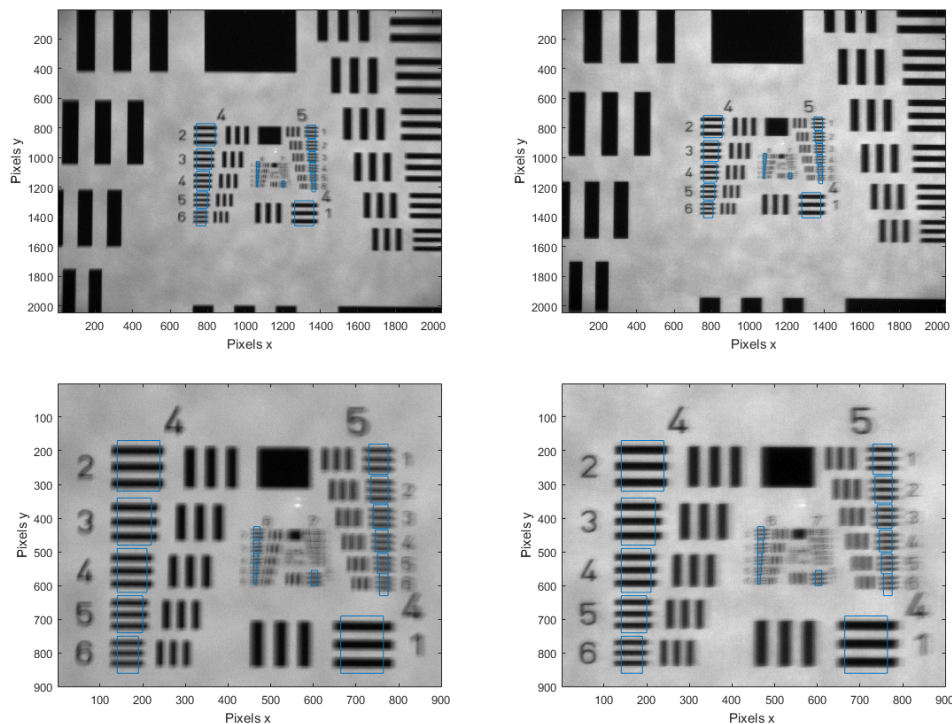


Figure 4.26. Acquired image of the USAF Target, on the left column the ones relative to the proprietary software (zoom below), on the right one the image produced using the implemented software (zoom below)

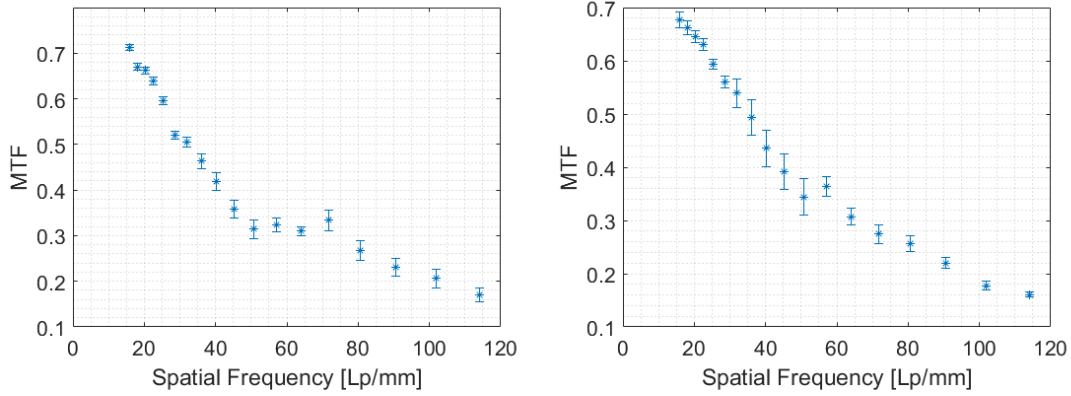


Figure 4.27. Evaluated behaviour of the MTF for the images in Figure 4.26, on the left the one relative to the proprietary software, on the right the one produced using the implemented software

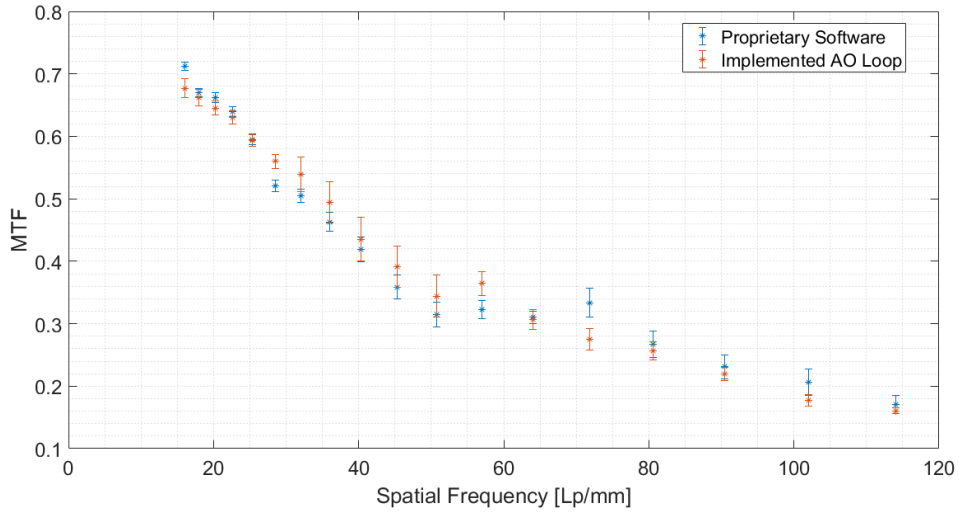


Figure 4.28. Superimposition of the MTF shown separately in Figure 4.27

4.5 Analysis of the Speed

A significant aspect of the realization of the system it has been to maintain a sufficient speed for the loop iteration (from the WS acquisition to the DM actuation), that could allow it to work properly while integrated with the remaining subsystems. For this reason the time needed to perform each iteration is monitored during the loop and from this information it is possible to evaluate the trend of the frequency behaviour during the running of the code. The speed was recognized to be in average proximal to $(21 \div 23) Hz$ with reduction of speed during the handling of the blinks due to what discussed in Section 3.6. Its behaviour

is shown in Figure 4.29.

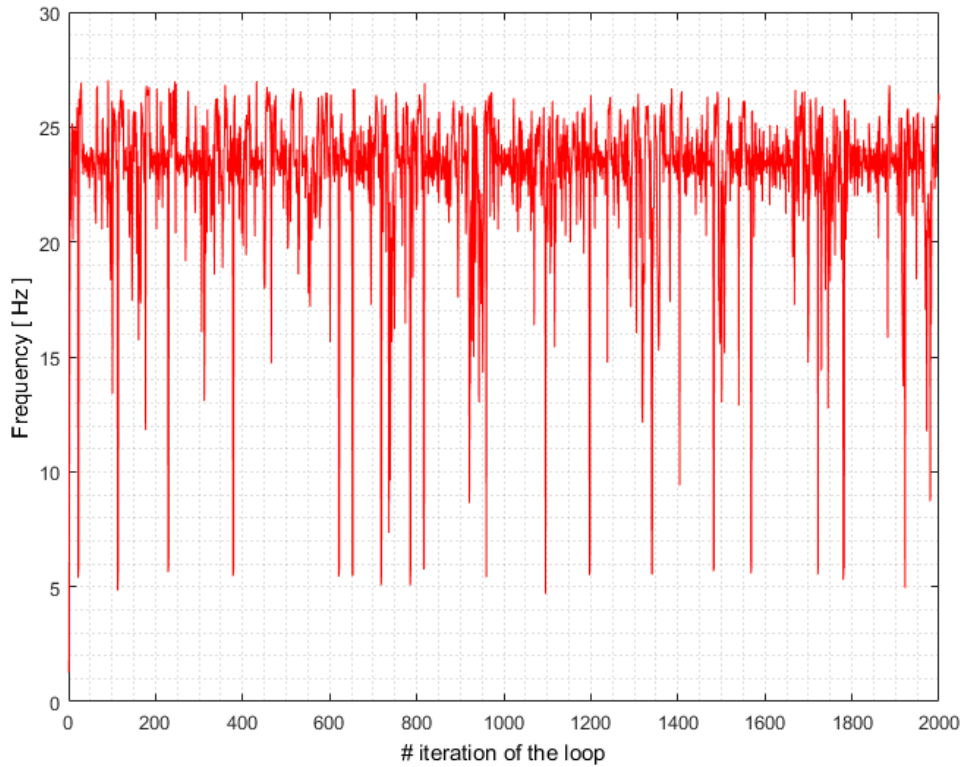


Figure 4.29. In-vivo test speed results, evolution of the frequency during the loop running, decrease of frequency are correspondent to blinks of the patient (Exposure Time = 11.74 ms, 32 modes, gain = 0.5, Power SLD = 28 μ W)

The further step performed is related to the will of understanding which are the main contributes that influence the speed during the loop. To do this, each section was timed separately with respect to the others and then a percentage analysis with respect to the total was provided. In Figure 4.30 it is shown the percentage of time related to each of the task required, while in Figure 4.31, the task are recollected in three different clusters: *Acquisition*, *Processing* and *Actuation*. Moreover, in Figure 4.32 it is shown the time required for each procedure during the whole loop. Finally in 4.2 are reported the average value of those times and their standard deviations.

As a consequence of the speed analysis performed, it is possible to assert that the principle bottleneck for the loop speed is for sure the image acquisition. Indeed, independently on the value of exposure the was chosen or auto-set the image acquisition task remains the most time-consuming task of the loop, in this test around 28%. Other important

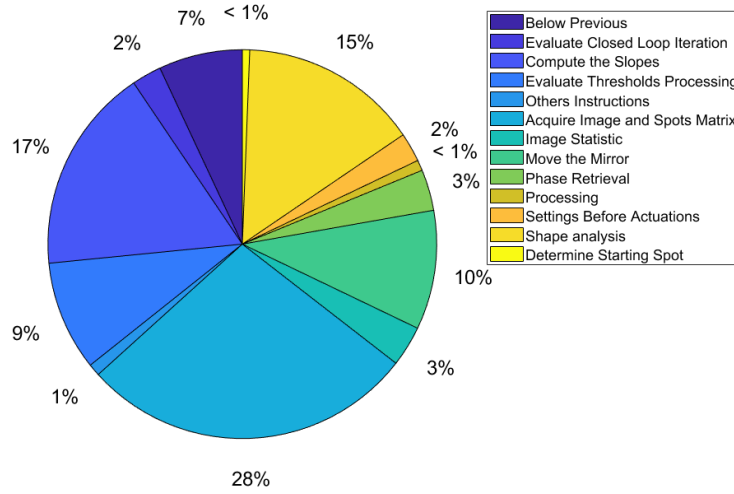


Figure 4.30. In-vivo test pie redistribution of the time required for the different tasks (Exposure Time = 11.74 ms, 32 modes, gain = 0.5, Power SLD = 28 μ W)

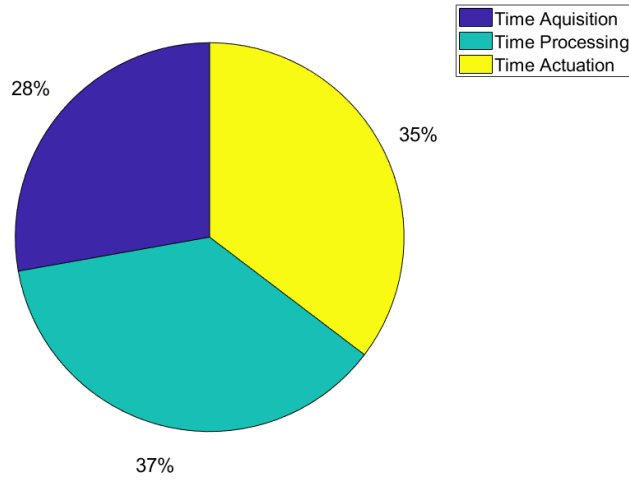


Figure 4.31. In-vivo test pie redistribution of the time required for the different tasks (Exposure Time = 11.74 ms, 32 modes, gain = 0.5, Power SLD = 28 μ W)

contributes are then given by the computation of the slopes, around 17%, and the mirror actuation, around 10%; concerning the figure of merit evaluation the more time consuming remains the shape analysis, around 15%. If the analysis is moved then to the *Acquisition*, *Processing* and *Actuation* clusters, it has been found that the time distribution among

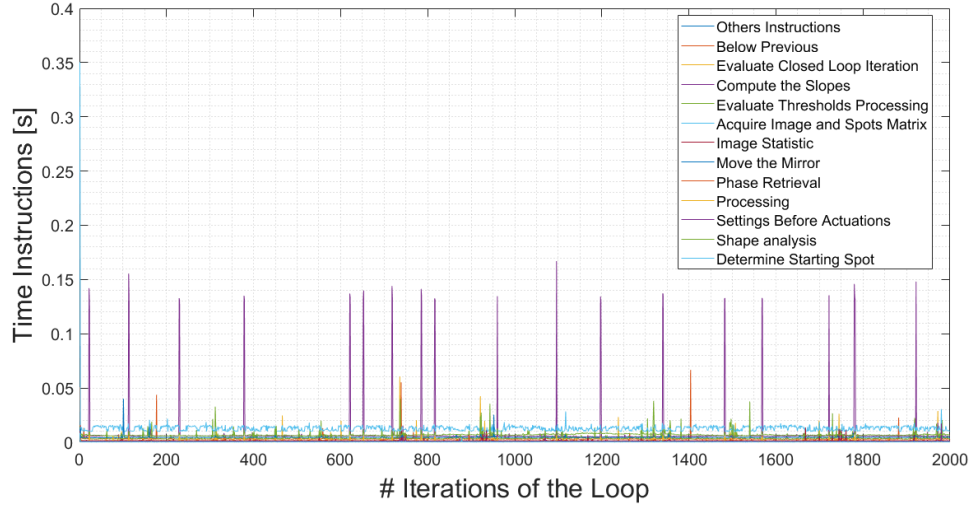


Figure 4.32. In-vivo test evolution during the loop the time required for the different tasks (Exposure Time = 11.74 ms, 32 modes, gain = 0.5, Power SLD = 28 μ W)

Speed Contributions		
Name Task	Average Time [ms]	Standard Deviation [ms]
Below Previous	3.21	2.49
Close Loop Iteration Evaluation	1.14	2.47
Compute Slopes	7.84	16.74
Evaluate Thresholds Processing	4.21	2.65
Get Image and spots' matrix	12.82	7.81
Image Statistic	1.56	0.80
Move Mirror	4.57	1.03
Phase Retrieval	1.57	0.30
Processing	0.41	0.70
Settings Before Actuation	1.12	0.45
Shape Analysis	6.86	1.39
Determine Start Spot	0.29	0.22
Others	0.46	6.93

Table 4.2. Speed contributions analysis

them is approximately equal, indeed each of them account for one third of the loop iteration required time. Concerning then the time required to reach the convergence of the system, that is to say the steady state, an average of 10 to 15 iterations are generally required.

Chapter 5

Conclusions and Future Works

Throughout this work it has been presented the development of the software to handle an *Adaptive Optics Loop*. The aim of the work has been to replace the current available proprietary software with something more manageable. This work spring from the forthcoming need to handle with ease the future integration of the many subsystem constituting the complex system that is used to take retinal scans at different depths with cellular resolution. The complexity of this system has been presented with more details in Section 3.1, where each of the subsystem task has been briefly tackled. First of all, to set the bases to accomplish the work required, the handling of the most complex of the subsystems, this thesis has moved from the description of the theoretical background that lays behind. For these reasons Chapter 2 has recalled in Section 2.1 the main optical concepts related to the system to be handled. Among them the most important one is certainly the *Optical Transfer Function*. The root of its importance derives primarily from the fact that, if the *Adaptive Optics* concept is seen with ease, the main aim of this kind of devices is to evaluate the *Optical Transfer Function* of the contribute the has to be removed [19]. After presenting in Section 2.2 and Section 2.3 the most significant anatomical and optical properties of the eye, the contribute to be evaluated and removed, the effect of eyes' aberrations, was described in Section 2.4 and Section 2.5. Furthermore, a brief delineation of the the hardware devices used, the *Shack-Hartmann Wave-front Sensor* and the *Deformable Mirror* were performed in Section 2.8 and Section 2.9 after the discussion of the origin of the Adaptive Optics concept (Section 2.7). Afterwards, the main steps for the realization of the loop code were discussed and developed in Chapter 3. Above all, in this chapter the focus was on the main issues related to the task to handle. The most significant one concerns the *Pupil Tracking* problems, mainly during the causalities of blinking (Section 3.5). The following step after the realization of the loop has been the validation and the testing of what was discussed in Chapter 3. The attention was focused on several critical aspects for the loop effectiveness. The first important element that was then considered is the presence of tilt on the mirror, as an effect that could lead to an increase of the total amount of voltage applied to the actuators. This effect could be an issue due to the power linked physical limitations of the device. Different configurations has been tested with different results, which were detailed in Section 4.1 concerning the loop behaviour and in Section 4.2 concerning their influence on the acquisition of images of the retina. Moreover, a further essential and crucial ability of the loop is related to its ability

to withstand to blinking casualties during the process of pupil tracking. As a consequence the whole set of concepts and methods presented in Section 3.5 has to be deeply tested. The results of this testing phase has been shown in Section 4.3, with really good results. Furthermore, a comparison with the existent proprietary software was performed thanks to the juxtaposition of the *Modulation Transfer Function* provided by the two codes. This measurements was possible thank to the usage of a USAF Target and has been presented in Section 4.4. Finally, a brief description of the speed contributions during the working of the software has been provided in Section 4.5. The series of tests performed to validate the work done has provided confirmation that the main issues tackled were solved. A more detailed analysis of the work done allows to point out the major contributions of this thesis. First of all, a skeletal simplified structure of the loop software was fully realized starting from the provided library functions, structure that allowed to correctly perform ex-vivo measurements. Moreover, the challenging in-vivo acquisition mode was handled and the main related issues were faced. The in-vivo procedure requires to adapt the exposure duration for the wave-front sensor acquisition to the patient, procedure that before was performed manually, constituting a bottleneck for the use of the existent proprietary software; the new developed software introduces the possibility of an automatic choice of this quantity to slim down the setting procedures required before the measurements. What probably is the main final contribution is the Handling of the Blinking. Indeed, as Section 4.3 has demonstrated, the system resulted to be 100% able to recognize blinking events and to takes countermeasures. This result was obtained without reducing the effectiveness of the procedure since no *False Positive* events has been recorded. Another important issue is related to the total amount of applied voltage. In fact, in this case a safety procedure was introduced allowing the loop to be maintained at work also when the limit of maximum applied voltage has been almost reached. This results is quite important because for the complexity of the in-vivo measurements is is less impacting the lost of the correction for the number of iterations required to reset the mirror and track again the aberrations than the crashing of the system which consequently implies the need to start again the measurements procedure as it was happening with the existent proprietary software. On the same path it is located the study of the reasons of this increment of the total applied voltage. A possible motivation has been individuated in the proliferating tilt applied to the mirror. This issue was tackled and a possible solution has been found, although this, further works is required to completely ensure the eradication of this problem. In conclusion, this work has set the foundations for the possibility to integrate the several control softwares that are currently handling the behaviour of the whole imaging device: from the current adaptive optics loop for the correction of the aberration and the maximization of the resolution, to the software used for the management of the transscleral illumination system.

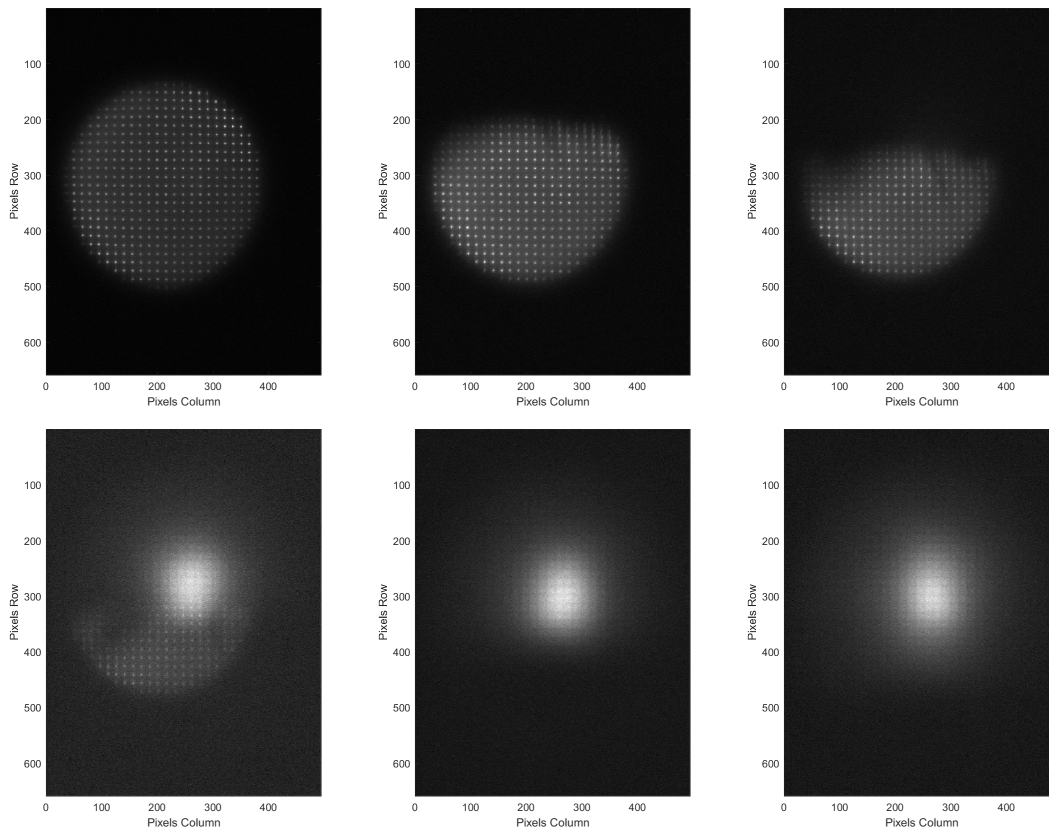
Bibliography

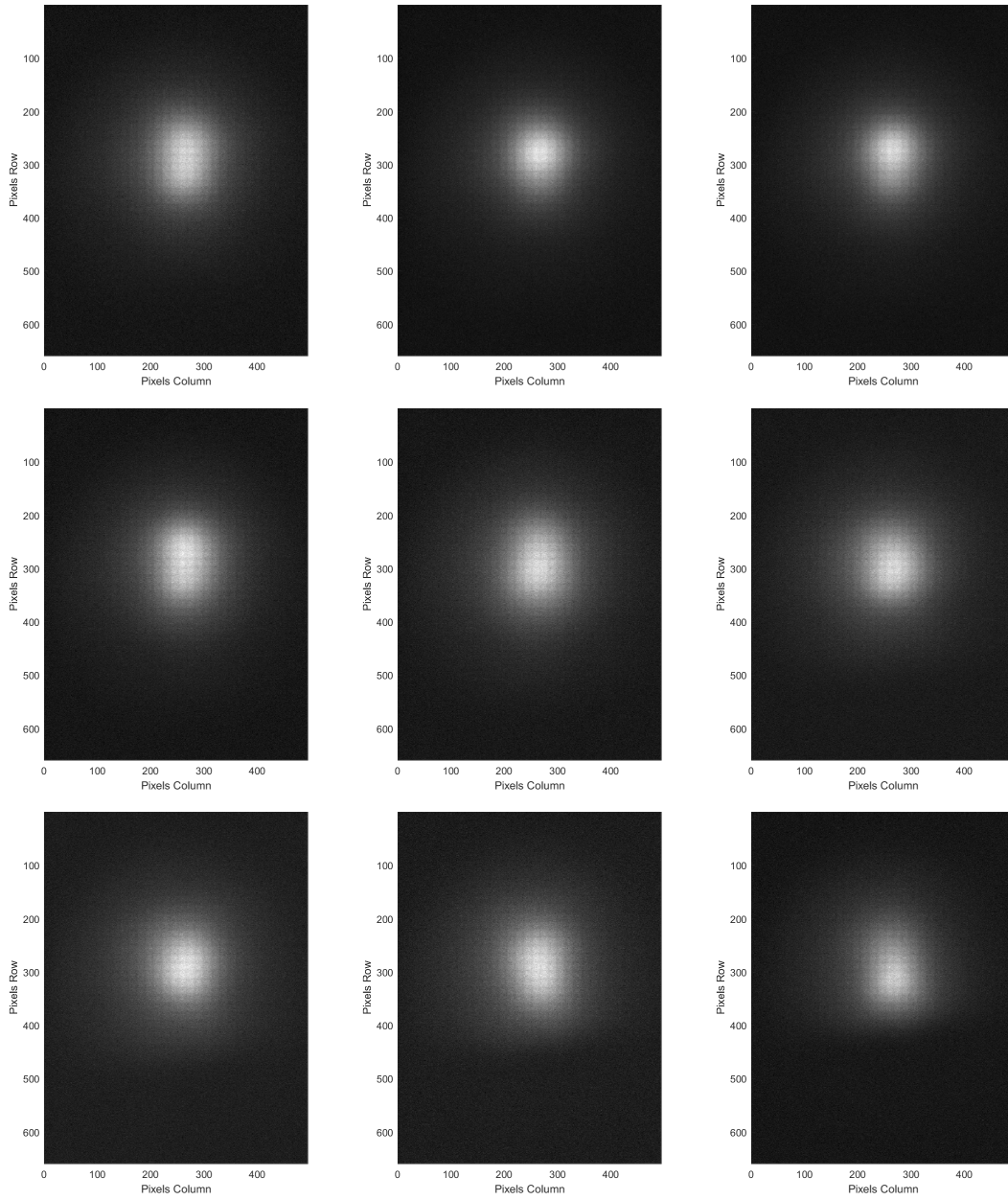
- [1] T. Laforest, D. Carpentras, M. Kunzi, L. Kowalczyk, F. Behar-Cohen, C. Moser, 2017, A new microscopy for imaging retinal cells
- [2] J. W. Goodman, 2005, Introduction to Fourier Optics
- [3] Shutterstock.com
- [4] K. Rogers, The eye: the physiology of human perception, Britannica educational Publishing
- [5] D. H. Hubel, 1995, Eye, Brain and Vision
- [6] H. Gross, 2008, Handbook of Optical Systems: vol 4., Survey of Optical Instruments
- [7] J. F. Koretz, G. H. Handelman, 2018, How the Human Eye Focuses
- [8] A. Popiolek-Masajada, H. Kasparzak, 2002, Model of the optical system of the Human Eye during Accommodation
- [9] D. Atchinson, G. Smith, 2000, Optics of the Human Eye
- [10] P. Mouroulis, 1999, Visual Instrumentation
- [11] Y. Le Grand, S. El Hage, 1980, Physiological Optics
- [12] H. L. Liou, N. A. Brennan, 1997, Anatomically accurate finite model eye for optical modeling
- [13] R. Navarro, J. Santamaria, J. Bescos, 1985, Accomodation-dependent model of the human eye with aspherics
- [14] M. K. Kim, 2011, Digital Holographic Microscopy Principles Techniques and Applications
- [15] D. Hillmann, H. Spahr, C. Hain, H. Sudkamp, G. Franke, C. Pfäffle, C. Winter, G. Hüttmann, 2016, Aberration-free volumetric high-speed imaging of in vivo retina
- [16] B. C. Flores, 1992, Robust method for the motion compensation of ISAR imagery
- [17] I. Newton, Opticks, 1704, 4th ed. New York, Dover.
- [18] C. Max, Introduction to Adaptive Optics and its History
- [19] B. C. Platt, R. Shack, 2001, History and principles of Shack-Hartmann wave-front Sensing
- [20] R. Tyson, 2011, Principles of Adaptive Optics
- [21] M. J. Booth, 2007, Adaptive optics in microscopy
- [22] D. R. Neal, J. Copland, D. Neal, 2002, Shack-Hartmann wave-front sensor precision and accuracy
- [23] S. Hicks, J Noé, A Simplified Shack Hartmann Sensor to Demonstrate wave-front Analysis
- [24] *By2pem–Ownwork, CC BY–SA 3.0, <https://commons.wikimedia.org/w/index.php?curid=15278966>*

- [25] R. H. Freeman, J. E. Pearson, 1982, deformable mirrors for all seasons and reasons, applied optics, vol 21, no.4
- [26] J. Feinleib, S. G. Lipson, P. F. Cone, 1974, Monolithic Piezoelectric Mirror for wave-front Correction
- [27] E. J. Fernandez, L. Vabre, B. Hermann, A. Hunterhuber, B. Povazay, W Drexler, 2006, Adaptive optics with a magnetic deformable mirror: applications in the human eye
- [28] W. H. Southwell, 1980, Wave-front Estimation from Wave-front Slope Measurements
- [29] International Standard IEC 60825-1
- [30] S.B. Mehta, C. J. R. Sheppard, 2009, Quantitative phase-gradient imaging at high resolution with asymmetric illumination-based differential phase contrast, optics Letters, Vol. 34, No 13
- [31] Datasheet Mirao 52, *Imagine OpticsTM*
- [32] Datasheet Haso4 First, *Imagine OpticsTM*
- [33] Wavekit Library documentation, *Imagine OpticsTM*
- [34] M. Laslandes, M. Salas, C. K. Hitzenberger, M. Pircher, 2017, Influence of wave-front sampling in adaptive optics retinal imaging
- [35] D. K. Roberts, Y. Yang, A. S. Lukic, J. T. Wilensy, M. N. Wernick, 2012, Quantification of Pupil Parameters in Diseased and Normal Eyes With Near Infrared Iris Transillumination Imaging
- [36] *png – zernike – polynomials – optics – comsol – multiphysics – ray – 1535039*
- [37] [http : //www.newton.cam.ac.uk/art/portrait.html](http://www.newton.cam.ac.uk/art/portrait.html)
- [38] ybialets at eso.org
- [39] [https : //earthobservatory.nasa.gov](https://earthobservatory.nasa.gov)

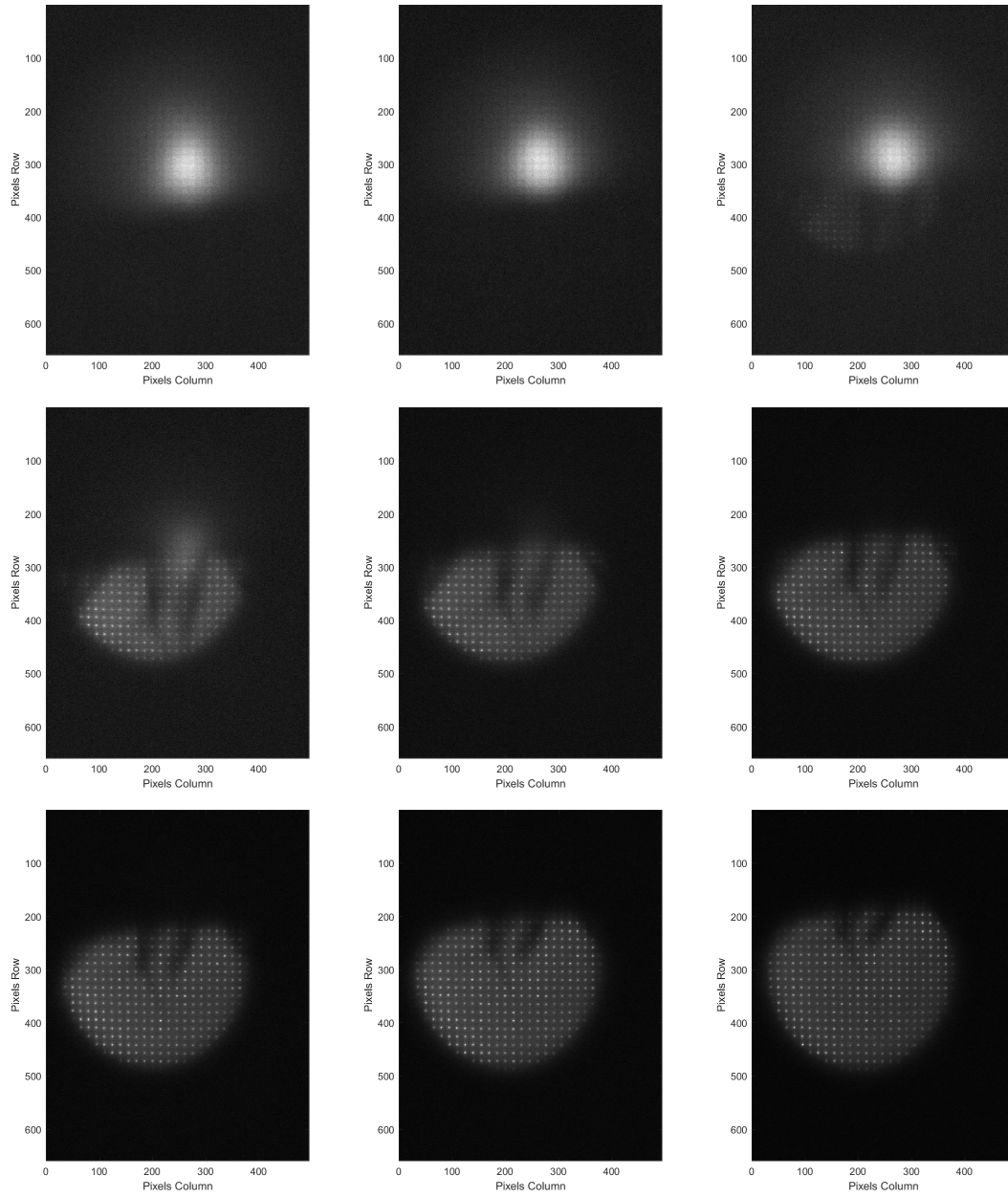
Appendix A

Spots' Matrix During Blinking





A – Spots' Matrix During Blinking



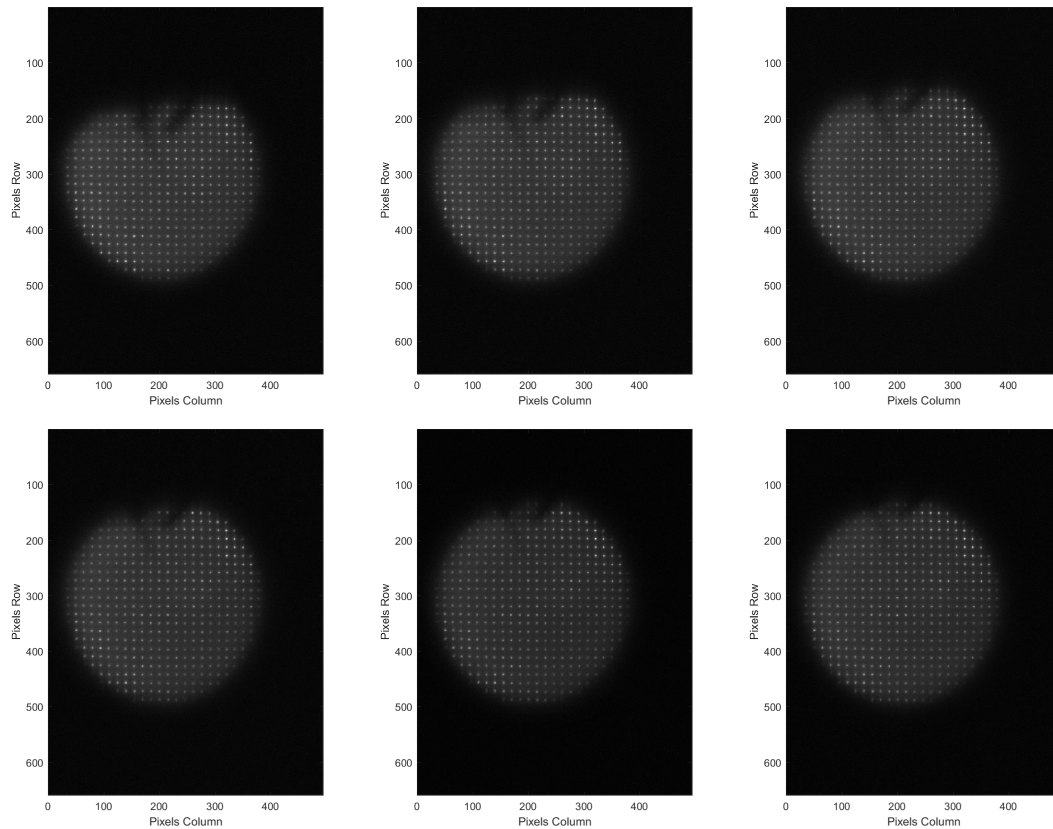


Figure A.1. from the beginning of the Appendix A it is possible to see the spots' matrix changing during a blink of the patient eye

Appendix B

Flow Diagram of the Loop

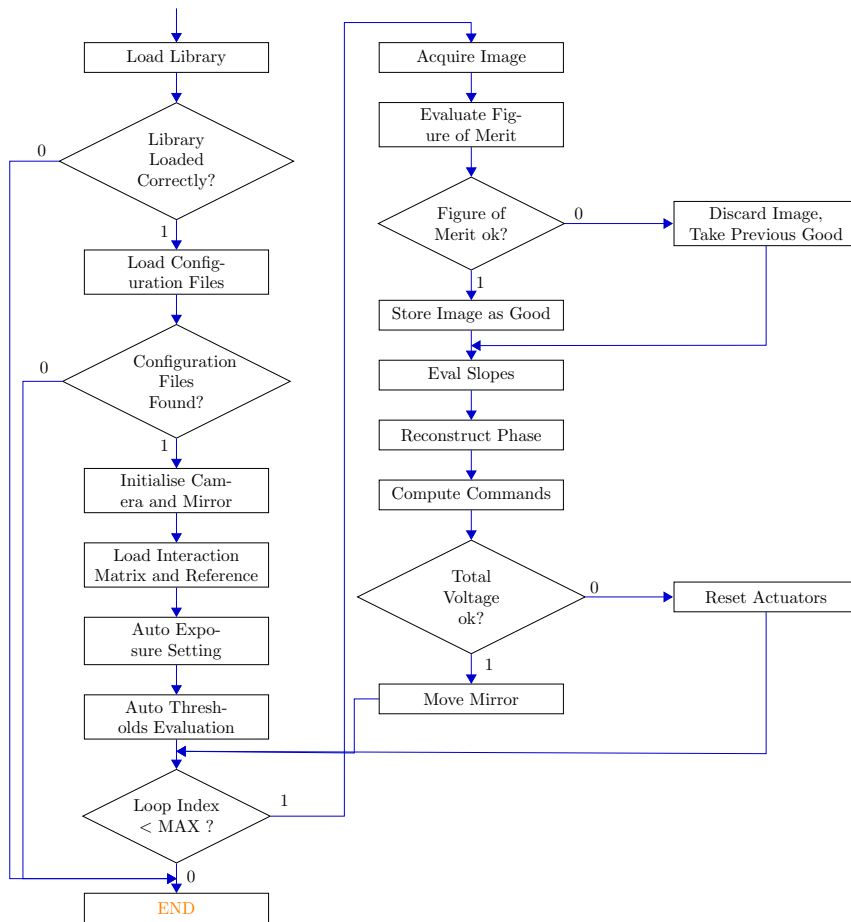


Figure B.1. More precise schematic of the evolution of the loop

Appendix C

In-vivo retina images

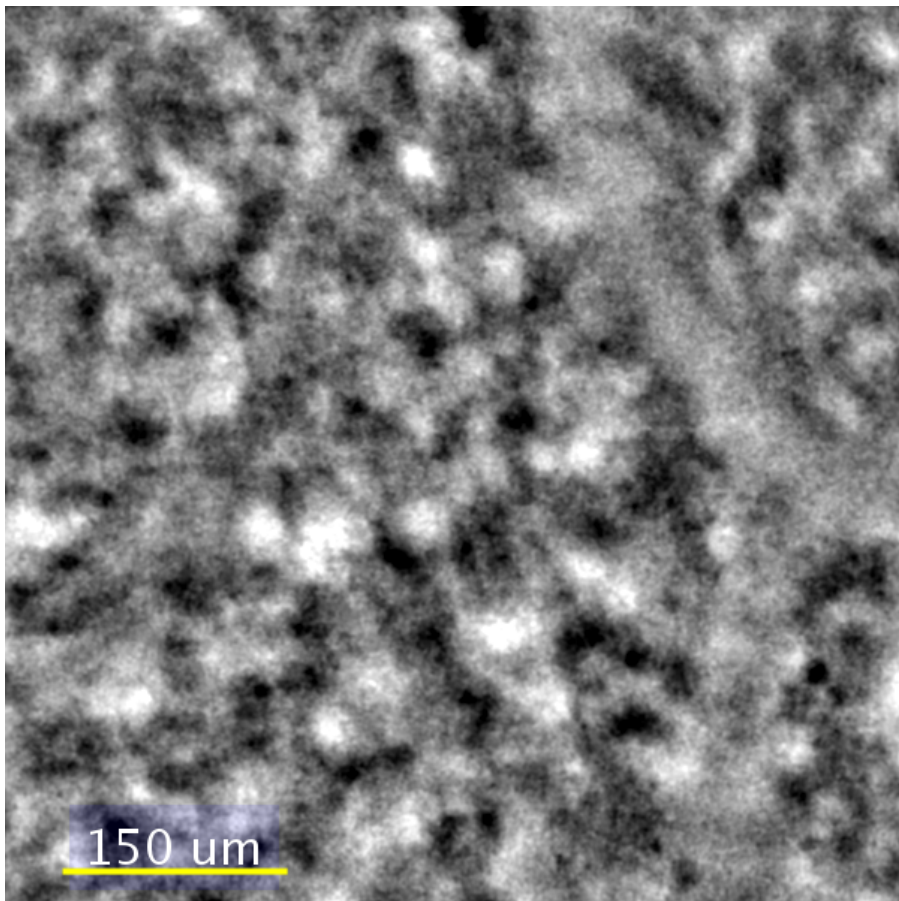


Figure C.1. Acquired image of the retina obtained with the forcefully removal of tilt configuration

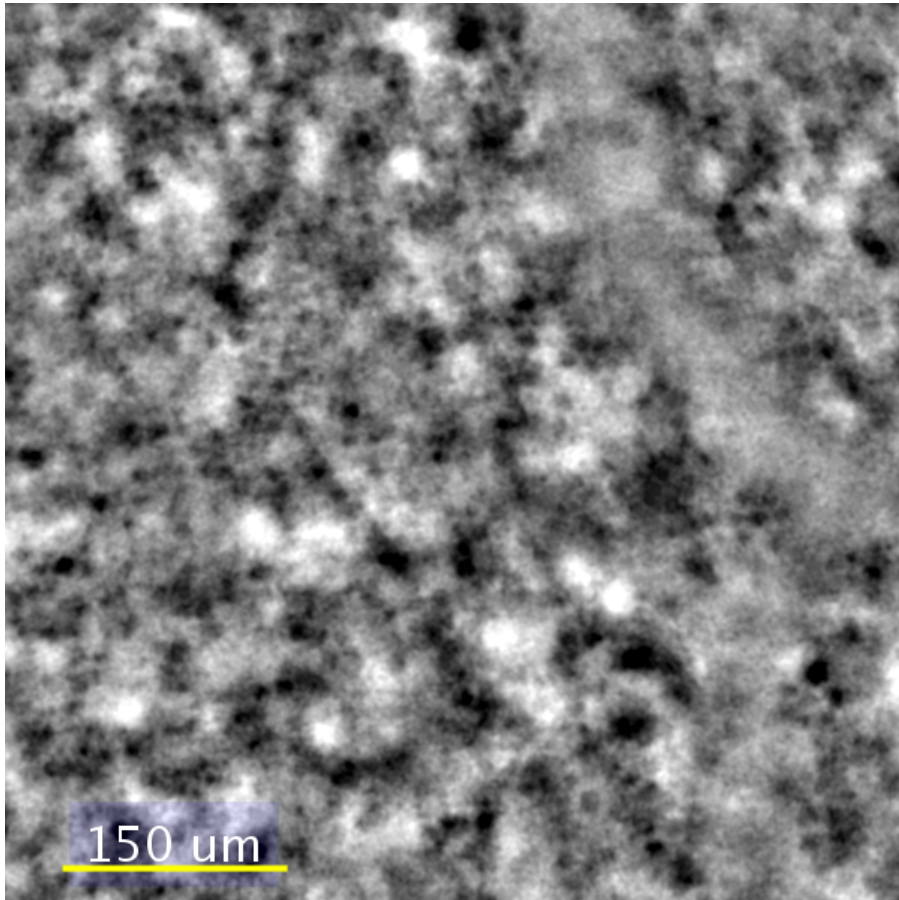


Figure C.2. Acquired image of the retina obtained with the *tilt_check* configuration

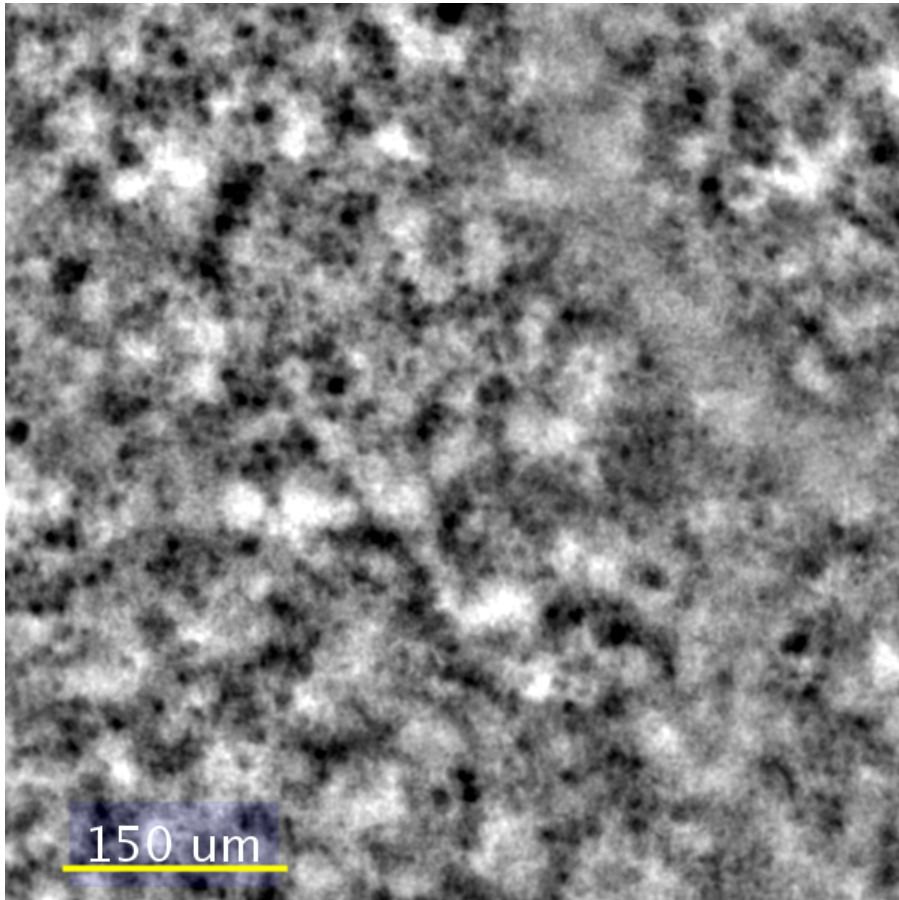


Figure C.3. Acquired image of the retina using the proprietary software.